



Atmospheric turbulence over crops

*confronting theories
with observations*

Atmospheric turbulence over crops - Anneke van de Boer

Anneke van de Boer

Propositions

1. For an unstable atmospheric surface layer, analytical footprint models predict a too large upwind source area and no downwind contribution.
(this thesis)
2. Monin-Obukhov similarity theory can be extended to include the effects of entrainment.
(this thesis)
3. Since women shy away from competitive workplaces (Gneezy et al. 2003, *Q. J. Econ* 118:3), the tenure track enhances gender inequality.
4. PhD-research should be combined with exercising, because non-competitive physical activities build self-esteem (Badami et al., 2012, *Res. Q. Exercise Sport* 83:2).
5. You can chain yourself to your desk, but you cannot chain your mind.
6. A cow faces east when the rain comes from the west.
7. A PhD-proposal is like the constraints of Monin-Obukhov similarity theory: never really achieved.
8. Instead of a bypass for cars, Wageningen needs a bicycle highway.

Propositions belonging to the thesis entitled

'Atmospheric turbulence over crops, confronting theories with observations'

Anneke van de Boer
Wageningen, 6 February 2015

Atmospheric turbulence over crops

Confronting theories with observations

Anneke van de Boer

Thesis committee

Promotor

Prof. Dr A.A.M. Holtslag
Professor of Meteorology
Wageningen University

Co-promotors

Dr A.F. Moene
Assistant professor, Meteorology and Air Quality Group
Wageningen University

Dr A. Graf
Senior scientist, Agrosphere Institute
Forschungszentrum Jülich, Germany

Other members

Prof. Dr R. Uijlenhoet, Wageningen University
Prof. Dr S. Kollet, Rheinische Friedrich-Wilhelms-Universität Bonn, Germany
Dr F. Lohou, Université Toulouse III - Paul Sabatier, France
Dr F.C. Bosveld, Koninklijk Nederlands Meteorologisch Instituut, De Bilt

This research was conducted under the auspices of the Graduate School for Socio-Economic and Natural Sciences of the Environment (SENSE).

Atmospheric turbulence over crops

Confronting theories with observations

Anneke van de Boer

Thesis

submitted in fulfillment of the requirements for the degree of doctor
at Wageningen University
by the authority of the Rector Magnificus
Prof. Dr M.J. Kropff,
in the presence of the
Thesis Committee appointed by the Academic Board
to be defended in public
on Friday 6 February 2015
at 4 p.m. in the Aula.

Anneke van de Boer

Atmospheric turbulence over crops, *confronting theories with observations*
x+145 pages.

PhD thesis, Wageningen University, Wageningen, NL (2015)

With references, with summaries in Dutch and English

ISBN 978-94-6257-241-6

Abstract

In this thesis we deal with some major challenges for studying atmospheric turbulence over crops. Land-atmosphere interactions are specifically complex because of surface heterogeneity and boundary-layer entrainment. Furthermore, the absence of high-frequency observations and of measurements of underlying soil and vegetation processes complicates studying these interactions. Atmospheric turbulence plays a key role in hydrological and carbon cycles and is essential for weather and climate. Understanding and forecasting turbulence is thereby relevant for human life and environment.

Turbulent scalar transport takes place via so-called ‘eddies’ that can be analyzed using the eddy-covariance method, in which high-frequency observations of wind speed, air temperature and gas concentrations are combined. The method is widely used to study gas exchange between a specific land surface and the atmosphere above. Before eddy-covariance became feasible, the so-called Monin-Obukhov similarity theory was used to estimate gas exchange, from low-frequency data. This theory is still used in models and data analyses, to relate mean turbulent quantities (e.g. vertical gradients, variances, and the refractive index structure parameter C_n^2) to atmospheric stability.

We evaluate semi-analytical footprint models that are used to estimate the surface source area of a turbulence measurement. These models are based on Monin-Obukhov similarity theory, which means that a homogeneous surface is assumed. Such models are however only needed for heterogeneous areas. Therefore, we critically test three of these models for eddy-covariance data gathered at a station surrounded by three different agricultural fields in Merken (Germany). By carrying out a natural tracer experiment, we generally find an overestimation of the footprint length, but a combination of two of our tested models results in an acceptable estimate for land-atmosphere studies over a site with environmental conditions similar to our site. This model is, however, very sensitive to atmospheric stability and surface roughness, and should not be used for highly convective cases.

For an intensive atmospheric measurement campaign in southern France (BLLAST), we find deviations from Monin-Obukhov similarity theory for humidity variances. Our study reveals that these were caused by entrainment of dry air from the free atmosphere that was transported all the way down to the surface. We develop a method to detect such entrainment events from eddy-covariance data only. Further-

more, we manage to quantify the contribution of entrainment to the total observed turbulence for a certain relative height within the boundary layer, and for a certain atmospheric stability, using variance budgets and scaling theories.

To apply Monin-Obukhov similarity theory for estimating mean turbulent quantities, in case no flux data are available, we test and extend a scheme from which surface fluxes can be derived from single-level weather data. This scheme is based on the Penman-Monteith approach, in which the dependencies of fluxes on the difference between air and surface temperature are linearized. We determine with tests on the two above-mentioned datasets and one year of data over grass in the Netherlands (Wageningen) that the scheme is most sensitive to the transpiration estimate. It matters largely which stomatal reaction on atmospheric water vapor deficit is implemented. We apply the scheme for the estimation of C_{n^2} from the derived surface fluxes via Monin-Obukhov similarity theory for a given location, height and wavelength, and thereby develop an approach that results in very good optical turbulence estimates for the above-mentioned agricultural sites.

Finally, we deal with the fact that eddy-covariance observations give us net exchange fluxes between the surface and the atmosphere, that result from both plant and soil processes. To distinguish plant transpiration from soil evaporation, a range of methods has been described in literature. We evaluate an existing method that is based on the observed correlation between CO_2 and water vapor fluctuations, and an estimated water-use efficiency of the vegetation. We perform a critical reevaluation of the method, specifically focusing on the estimation of the water-use efficiency and assumptions considering the temperature and humidity profiles in and above the canopy. We suggest a determination to improve the method for a growing wheat field in Merken (Germany).

Keywords: Atmospheric turbulence, eddy covariance, footprint model, surface heterogeneity, entrainment, Penman-Monteith, crop water-use efficiency, transpiration

Contents

Abstract	v
1 Introduction	1
1.1 Description of atmospheric turbulence	2
1.2 Atmospheric turbulence in a simplified world	4
1.3 Real-world topics discussed in this thesis	5
1.4 Turbulence observations	8
2 Sensitivity and uncertainty of analytical footprint models according to a combined natural tracer and ensemble approach	11
2.1 Introduction	12
2.2 Model description	14
2.2.1 HKC00 and KM01	14
2.2.2 Our implementations	16
2.3 Research strategy	18
2.3.1 Footprint model evaluation	18
2.3.2 Sensitivity analysis and specification of the ensemble	20
2.3.3 Ensemble average	21
2.4 Data	21
2.4.1 Experiment	21
2.4.2 Processing	23
2.4.3 Land use map	23
2.5 Results and discussion	24
2.5.1 Meteorological conditions and eddy covariance fluxes	24
2.5.2 Footprint model evaluation: Forward method	24
2.5.3 Footprint model sensitivity to input parameters	27
2.5.4 Footprint model ensemble average	28
2.5.5 Footprint model evaluation: Inversion method	29
2.6 Conclusion and outlook	30
2A Appendices	32
2A.1 Footprint model equations	32
2A.2 Surface layer scaling	33

3	Detection of entrainment influences on surface-layer measurements and extension of Monin-Obukhov similarity theory	35
3.1	Introduction	36
3.2	Theory	37
3.2.1	Surface-Layer and Boundary-Layer Scaling	38
3.2.2	Entrainment Signals in Surface-Layer Observations	42
3.3	Data and Methods	44
3.3.1	Field Measurements	44
3.3.2	Data Analyses	47
3.4	Results and Discussion	52
3.4.1	Meteorological Conditions	52
3.4.2	MO Similarity Theory for Different Surfaces and Scalars	53
3.4.3	Indications of Entrainment in ASL Observations	54
3.4.4	Relations Between ASL Observations and Entrainment Regime	57
3.4.5	MO Similarity Theory in Relation to Entrainment Data	59
3.5	Conclusion	62
3A	Appendix	63
4	Estimation of the refractive index structure parameter from single-level daytime routine weather data	67
4.1	Introduction	68
4.2	Framework	69
4.2.1	Estimation of surface fluxes from single-level weather data	71
4.2.2	Estimation of temperature, humidity and joint structure parameters from surface fluxes	74
4.2.3	Estimation of C_{n^2} from temperature, humidity and joint structure parameters	75
4.3	Data	75
4.3.1	Datasets	76
4.3.2	Data processing and selection	77
4.4	Estimates and validation	79
4.5	Results	80
4.6	Discussion	84
4.7	Conclusions	89
4A	Appendices	89
4A.1	Appendix A; Scheme to estimate fluxes from weather data	89
4A.2	Appendix B; Coefficients capturing the wavelength dependency of C_{n^2}	93
5	Leaf water-use efficiency: impact on the estimation of evapotranspiration partitioning	95
5.1	Introduction	96
5.2	Theory	97

CONTENTS

5.2.1	General concept	97
5.2.2	Original method	98
5.2.3	Determination of <i>WUE</i>	100
5.3	Methods	102
5.3.1	Data	102
5.3.2	Research strategy	103
5.4	Results	105
5.4.1	WUE: methods to derive external and internal CO ₂ and H ₂ O concentration	105
5.4.2	WUE: evaluation-height dependence	106
5.4.3	Hybrid method to derive <i>WUE</i>	107
5.4.4	Partitioned fluxes: <i>WUE</i> dependence	108
5.5	Discussion	109
5.6	Conclusions	111
6	Perspectives	113
6.1	Footprint modeling over complex terrain	113
6.2	Footprint modeling for a highly turbulent atmosphere	114
6.3	Effect of surface heterogeneity on Monin-Obukhov similarity theory derived from observations	115
6.4	Modeling deviations from Monin-Obukhov similarity functions	117
6.5	Applications to urban areas	119
6.6	Measurement campaigns	120
	References	123
	Samenvatting	131
	Dankwoord	137
	The author	139
	Journal publications by the author	141
	Education of the author	143

1

Introduction

Life is mainly present near the interface between the earth surface and the atmosphere. One of the interactions between the soil, vegetation and atmosphere is the uptake, release and distribution of gases like CO₂ and water vapour, in which atmospheric turbulence plays a key role. Gas exchange processes are related to transport of pollen, black carbon, heat, moisture, and thereby greatly influence our health and comfort, as well as weather and climate. Because the Earth's surface is continuously changing (partly by human activities), we should know the effect of different types of surfaces on the atmosphere and vice versa. For example, cutting a pine forest may lead to less transpiration, and thus a higher ground water level locally. On a larger scale, forest clearance causes an increase in atmospheric CO₂, leading to a warmer earth surface.

To predict and evaluate characteristics of the soil, vegetation and atmosphere (e.g. crop growth, rain, global temperature), we need to understand transport processes at different scales. This thesis focuses on processes at relatively small scales in approximately the lowest 100 m of the atmosphere, which is called the atmospheric surface layer. In this chapter, we first explain how and where turbulence is formed, how it can be recognized, and how it is described. Next, we present how the atmospheric surface layer is simplified for academic studies. Furthermore we describe how these simplifications differ from the real world, and we thereby introduce our research questions. Finally, we describe how and where we measured atmospheric turbulence for our studies.

Chapters 2, 3 and 4 of this thesis are published in three different scientific jour-

nals, and Chapter 5 is in preparation for submission. The individual chapters are presented as published, therefore especially the measurement-methodology descriptions slightly overlap. Our vision on and recommendations for atmospheric-turbulence studies are given in Chapter 6. At the end of this thesis, my acknowledgments, research school certificate and a list of my publications are presented.

1.1 Description of atmospheric turbulence

An example of atmospheric turbulence can be observed by watching the scintillations or twinkling of an object over hot asphalt or transpiring maize. A very turbulent atmosphere is characterized by many whirls, so called eddies, of different sizes and air densities, that are chaotically moving and rotating, indicated by circular arrows in Figure 1.1. Such a whirl can for example be observed when it is strong enough to pick up some leaves.

Turbulence is generated by surface heating. A relatively warm surface heats the air parcels just above, which thereby get lighter and will rise. Birds and gliders make use of such rising air parcels, also called thermals. Relatively heavy, cold air will consequently sink, and buoyancy turbulence is produced.

On a sunny summer day, the air will be warmer above a dry sandy area than above well-watered vegetation, because in the first case, energy is used for atmospheric heating, whereas it is used for evapotranspiration in the second case. In a daytime surface layer, the wind speed increases and humidity and temperature decrease rapidly with height (see Figure 1.1 for the decrease with height of temperature and humidity).

Turbulence is also mechanically produced. Mechanical turbulence is the result of an airflow over a surface with obstructions (e.g. plants). The wind speed, surface roughness, and stability of the air, determine the strength of mechanical turbulence. The stronger the airflow that moves contrary to the main flow, the more whirls are formed. This is also the type of turbulence one notices in an aircraft, or that is attempted to be minimized using aerodynamic helmets, suits and vehicles.

The largest eddies can be as large as the atmospheric boundary-layer height, which is the height until which the surface has a direct effect on the temperature, humidity and motions of the air. The large eddies in the boundary layer break down into smaller eddies, since energy cascades, and the smallest eddies (≈ 1 mm) dissipate: the mechanical energy of the eddy is converted into heat due to friction. The top of the boundary layer is over land typically between 500 and 2000 m during the day, which corresponds with eddies with a maximum duration of 15 to 20 min.

On top of the boundary layer, there is an inversion layer with a positive potential temperature gradient, i.e. the potential temperature, the temperature an air parcel would have when brought adiabatically to a standard referenced pressure, increases with height (see Figure 1.1). This layer suppresses turbulent exchange between the

1.1. DESCRIPTION OF ATMOSPHERIC TURBULENCE

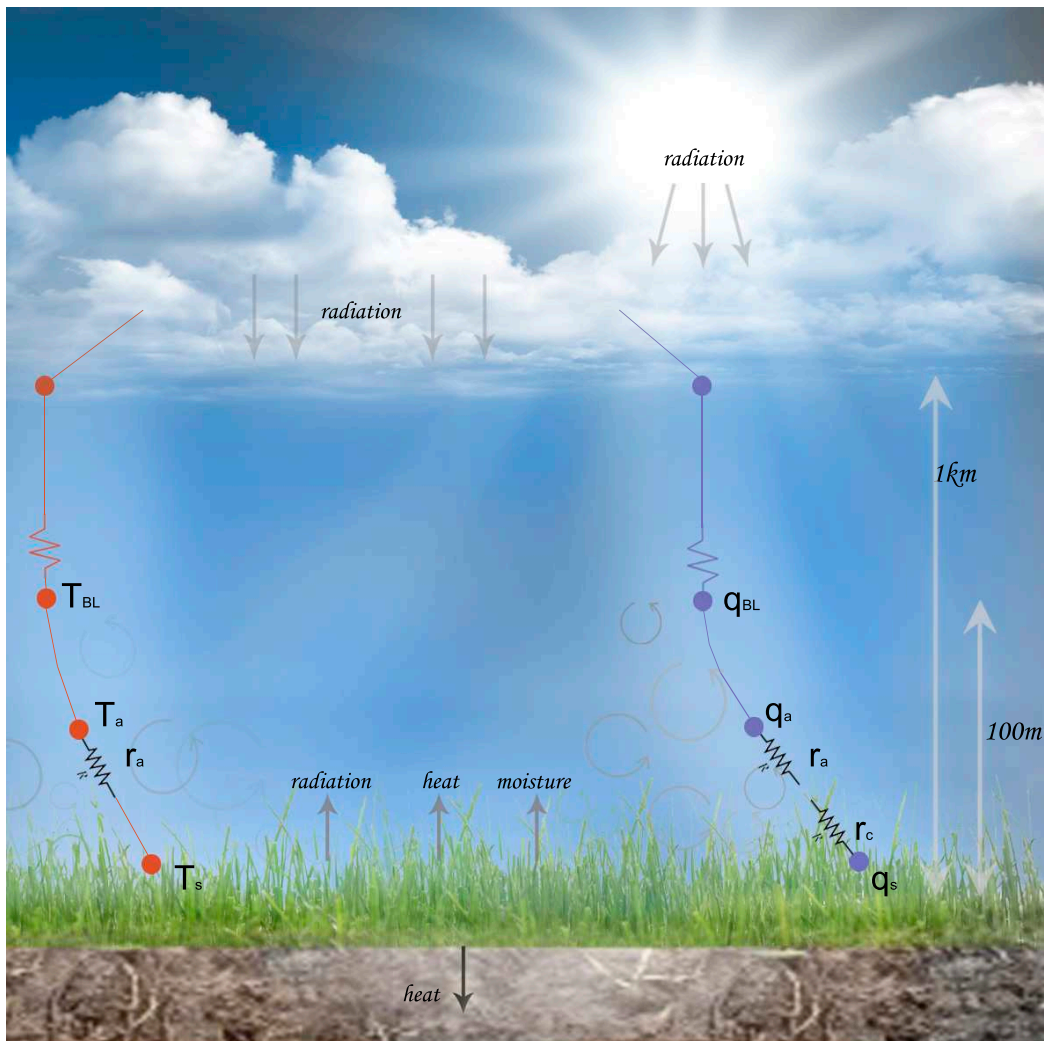


Figure 1.1: Daytime situation of the atmospheric boundary layer (BL) in a simplified world, where the rate of exchange of heat and moisture between the surface (s) and air (a) is theoretically controlled by resistances (r_a and r_c), and where the surface influences the vertical profiles of potential temperature (T) and humidity (q). Net radiation at the surface equals soil and air heating and evaporation and transpiration (moisture flux). The indicated surface-layer and BL heights are estimates, as they depend on the weather and the time of the day.

boundary layer and the free atmosphere aloft (up to ≈ 10 km above the inversion layer). The suppression of exchange between the boundary layer and the free atmosphere causes the concentration of pollutants to be much higher in the boundary layer. The inversion layer can often be seen from an air-plane around the cloud layer, as the transition between humid polluted air and dry cleaner air.

1.2 Atmospheric turbulence in a simplified world

Because turbulent motions are chaotic, they can only be described using statistics and probability theory in atmospheric models and data analyses. One way to quantify atmospheric turbulence is using Reynolds decomposition, in which the fluctuating parts of a variable are separated from the mean. This represents that individual eddies are characterized by a different temperature, humidity and wind speed than the mean air characteristics. The average deviation from the mean, and the related variance, are used as a measure of how far the values (e.g. temperature) are spread out, i.e. how many different air parcels are present.

The temperature variance can be combined with the variance of the vertical wind speed, to determine the vertical flow rate, flux, of in this case heat (represented by straight arrows in Figure 1.1). This flux calculation follows the so-called eddy-covariance technique, which makes use of the average product of the vertical wind-speed variance and the variance of another variable. The required eddy-covariance instrumentation is given in Section 1.4.

Another mean statistical quantity that can be used to characterize atmospheric turbulence is the structure parameter of scalar x , C_{x^2} . It relates the difference between concentrations at two locations to the fluctuation intensity, and can be interpreted as a spatial variance. Atmospheric turbulence can be quantified by combining the effects of temperature and humidity fluctuations on the structure parameter of the refractive index of air, C_{n^2} . The refractive index n describes the propagation and refraction of a beam, as a function of its wavelength, in this case through the air.

In a turbulent atmosphere, n changes in time and space because all beams travel through air parcels with different air densities and thus different refractions of the beam. Diffraction of an optical beam between an object and ones eye gives a blurred vision of for example a tree behind a transpiring maize field. An example of the result of internal reflections in water droplets is the rainbow. Light of different colors that together form white light is refracted when both entering and returning from a water droplet. Because each color corresponds with a slightly different wavelength, n differs per color and the light beam spreads out as a rainbow.

At the earth surface, the lower boundary of this layer, radiation that is not reflected is used for heating of soil and plants, heating of air, thermal radiation into the atmosphere, evaporation of soil water, and transpiration of water by photosynthesizing plants. This system is in energy balance, which means that the sum of soil and air heat transport and evaporation and transpiration equals net radiation received from the sun and the atmosphere (e.g. from clouds and greenhouse gases), as indicated in Figure 1.1 (assuming an infinite thin surface as control volume for the energy).

Due to turbulent mixing, wind speed, humidity, and potential temperature are, in the simplified world, constant with height in the boundary layer above the surface layer (as indicated with the vertical lines (profiles) of potential temperature and

humidity in Figure 1.1). Furthermore, the exchange between the boundary layer and the free atmosphere does not influence the surface-layer processes in the simplified world.

To capture the transport between the land surface and the atmosphere, both in weather and climate models and in observations, a widely used theory was introduced by Monin and Obukhov (1954). Monin-Obukhov (MO) similarity theory relates turbulence properties within the atmospheric surface layer to the surface fluxes, based on dimensional analysis. Therefore, derived relationships between atmospheric variables for a certain situation, can be applied to all similar situations. Their theory is applicable to an ideal flat and homogeneous surface, for temperature, humidity, CO₂, wind speed, and other variables. For example, if the air temperature is known at two heights, then the surface sensible heat flux can be estimated for a certain height and situation (atmospheric stability and wind speed). Also, relationships between a variable's variance and the corresponding flux are empirically derived for a range of atmospheric stabilities, known as flux-variance relationships.

The rate of exchange of heat and moisture between the surface and atmosphere depends on the buoyancy intensity, wind speed, and on the roughness of the surface. A wind flow over a surface with plants with various heights (a rough surface) will produce strong turbulence, which enhances the transport of heat and moisture released by the soil and vegetation. Accumulation of the released heat and moisture occurs around the plants in case of no transport.

In theories and models, the complex surface-roughness dependency of the surface fluxes is represented as a resistance (see at the bottom of the vertical profiles in Figure 1.1). This so-called aerodynamic resistance is very low when the atmospheric surface layer is very turbulent, such that the surface heat flux is relatively high.

The moisture flux, called the evapotranspiration flux, additionally depends on plant physiology via the so-called canopy resistance (see Figure 1.1). If a plant experiences heat stress (e.g. when radiation or temperatures are high), or water stress (e.g. when the soil or the air is dry), then the plant decreases the loss of water by closing its stomata. This is represented by a high canopy resistance in crop models and leads to less photosynthesis and transpiration, and on a larger scale to a drier and warmer boundary layer, with fewer clouds and rain.

1.3 Real-world topics discussed in this thesis

Studying atmospheric turbulent transport, we obtain knowledge about the related land surface. To understand the soil-vegetation-atmosphere system, generalizations based upon empirical observations need to be developed and tested. In this thesis we study how and why turbulent transport deviates from the simplified cases described above, and how we can implement real-world implications in atmospheric-turbulence studies and simulations. We tested and improved four of such concepts

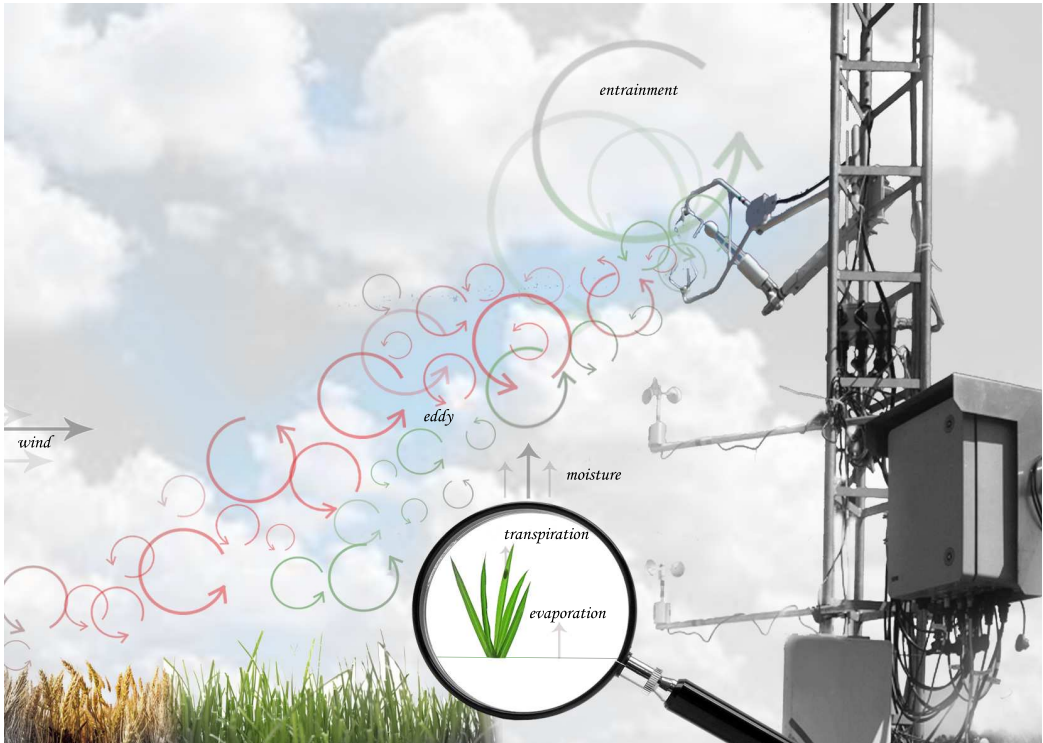


Figure 1.2: Daytime situation of the atmospheric surface layer in the real world, with an eddy-covariance station with a flux footprint, indicated with eddies, upwind from the station leaving either the wheat or grass. A large eddy related to entrainment reaches the instruments as well. The magnifier shows the plant and soil processes that together form an upward moisture flux.

that are commonly used by modelers and data analysts. These are all related to the exchange of water vapour, heat and momentum via atmospheric turbulence.

The first two concepts we deal with in this thesis, consider the sources of atmospheric turbulence. The third concept deals with estimating turbulence in the absence of turbulence observations. The fourth concept involves separating plant processes from soil processes, while measuring the net exchange. We restricted the studies to daytime data, when boundary-layer turbulence is much better defined. Each of the paragraphs below introduces a problem that is related to the studies that are presented in this thesis.

Parameterizations for turbulent transport in land-surface models are generally based on a landscape with only one land use type. Measurements that are used for validating these models, are therefore ideally performed over a homogeneous terrain. However, in the real world, eddy-covariance flux measurements originate from a mostly upwind area that might be a mixture of land use types, depending on the measurement site. This area is called the flux footprint, and will be larger if one

measures higher up or when the atmosphere is stably stratified such that horizontal motions are relatively important with respect to vertical motions. An example is given in Figure 1.2, where the footprint is the horizontal area where the air parcels leave the surface.

Different land-use types next to each other create a variable source and sink distribution, and thereby influence the turbulent flow field. To determine whether flux measurements come from the agricultural field of interest, footprint models are used to estimate the extent of the source area of eddy-covariance measurements. Because numerical models are computationally expensive, several analytical footprint models have been developed (Leclerc and Foken, 2014). These footprint models assume MO similarity theory, and thus a homogeneous turbulent flow field. However, footprint models are only needed for heterogeneous area's. So which footprint model is the best for studying turbulent transport over a heterogeneous surface?

We investigate this, by testing the three most-commonly applied analytical footprint models. Different than what they are developed for, we critically evaluated the estimated footprint for an eddy-covariance station surrounded by three different land-use types. We measured latent and sensible heat fluxes separately at these land-use types, and compared the fluxes of the mixed station with the fluxes as calculated from combining the locally measured fluxes of the surrounding land-use types with the estimated footprint (Chapter 2).

The land surface and the inversion layer, also called the entrainment zone, define two boundaries of the simplified atmospheric boundary-layer. However, even across a strong inversion, the boundary-layer top exchanges air with the free atmosphere aloft (enhanced by wind shear). MO similarity theory considers basically a horizontally homogeneous surface layer, thus a homogeneous surface *and* no influences from the free atmosphere. The surface layer might in reality however be affected by entrainment, such that the theory is not applicable. This is indicated with the big whirl in Figure 1.2. Compared to the boundary layer, the free atmosphere is relatively dry and warm (see the upper parts of the temperature and humidity profiles in Figure 1.1). During daytime, the effect of entrainment on the water-vapour content in the boundary layer is thus opposite to that on the boundary-layer temperature.

In Chapter 3, we discuss the effect of entrainment on deviations from simplified-world turbulence predictions that follow from MO similarity theory. What is the exact impact of entrainment on flux-variance relationships derived from this theory? We compare MO similarity theory with eddy-covariance measurements, and use boundary-layer measurements to quantify humidity entrainment. We use an analytical footprint model to select situations in which the measurements originate from one land use type only, such that the criterion of a homogeneous surface is met. Furthermore, we theoretically derived a term to expand MO similarity theory for entrainment. For that we used an existing budget of the humidity flux variance, in which the total humidity variance is equal to the sum of a surface and

an entrainment term (Chapter 3).

A concept that is used to derive surface heat fluxes and turbulence from single-level weather-station data is discussed in Chapter 4. This scheme is based on the Penman-Monteith equation that can be used for determining evapotranspiration from air temperature, wind speed, humidity and solar radiation. The scheme is furthermore based on the surface energy balance, and can be used in combination with MO similarity theory in case turbulence observations are not available. But, how well can this 'big leaf' approach represent surface heat fluxes for an agricultural field? Moreover, how good are turbulence estimates derived from these fluxes using MO similarity theory? We quantify atmospheric scintillations by estimating C_{n^2} from the surface fluxes, using MO similarity theory. We test our approach for two different locations and land use types, for both an optical and a millimeter wavelength, and compare daytime estimates with C_{n^2} values determined from eddy-covariance measurements (Chapter 4).

The moisture transport in the atmospheric surface layer is generally measured as the evapotranspiration flux. This is the net flux of evaporation related to soil processes, and transpiration related to plant photosynthesis (see the magnifier in Figure 1.2). The observed daytime CO_2 -transport is the result of the production of CO_2 by soil organisms, and the uptake of CO_2 by plants for assimilating carbon for their metabolism. For studying e.g. plant growth or water usage, only transpiration and assimilation are the variables of interest, whereas they cannot be measured directly at field scale. For studying plant processes at field scale, the observed net fluxes should be partitioned.

We present in Chapter 5 a study on partitioning transpiration and evaporation, and assimilation and respiration, from eddy-covariance data. We tested and improved a method that is based on the observed correlation between CO_2 and water-vapour fluctuations, and a calculated water-use efficiency of the vegetation. Different algorithms were studied to determine the leaf water-use efficiency. Furthermore, the sensitivity of the partitioning method to the water-use efficiency was examined (Chapter 5).

1.4 Turbulence observations

Atmospheric turbulent transport of gas above a certain surface is often measured using the eddy-covariance technique. This method relates the covariance between vertical wind speed fluctuations and fluctuations in the concentration of a specific gas, to land-atmosphere gas exchanges. The instrumentation contains a gas analyzer and a sonic anemometer, to respectively measure fluctuations in gas concentrations (e.g. CO_2 , water vapour or methane), and fluctuations in the horizontal and



Figure 1.3: Locations from which data is used for the studies presented in this thesis (courtesy of Google Earth): the meteorological site in a flat grass area in Wageningen, the Netherlands, the FLUXPAT-2009 campaign in a relatively flat area with wheat, barley and sugar beets in Merken, Germany, and the BLLAST-2011 campaign in a relatively flat area with wheat and grass in Lannemezan, France.

vertical wind speed. Such an instrument can be installed on a tower, ship, or aircraft. An example is given in Figure 1.4, where the instruments are installed on a mast in a wheat field. The temperature, humidity and wind speed fluctuations are measured at a high frequency of ≈ 20 Hz, to minimize the statistical errors of the turbulent quantities that are derived from a certain amount of samples. A time interval of 30 minutes is often used because it is long enough to capture the most important turbulence scales, and short enough to exclude concentration variations caused by weather events or by the diurnal cycle (different solar input). An eddy-covariance station is rather expensive ($\approx 25\text{k€}$) and is not (yet) standard at an official weather station.

We based all analyses on observations over different regions and crop types. We had access to data from two measurement campaigns and from one continuously operating meteorological site. The continuous meteorological site we used is located in the Netherlands (Wageningen), in an agricultural area with grass as the main land-use type. An eddy-covariance station was installed at the site in 2005.

The objective of the FLUXPAT campaign in the summer of 2009 in western Germany (Merken) was to study patterns in soil-vegetation-atmosphere-systems. A variety of soil and vegetation parameters were measured. Three eddy-covariance stations were located in a field with sugar beets, winter wheat, and barley. One eddy-covariance station was installed at the edge between two of these fields, such that data with homogeneous and heterogeneous footprints were observed.

I was involved in the BLLAST campaign in the summer of 2011 in southern France,



Figure 1.4: *The author of this thesis working with, among other instruments, a gas analyzer and a sonic anemometer (above in the mast), in a wheat field in southern France during the BLLAST campaign in 2011.*

which was mainly intended for studying the late afternoon transition of the atmospheric boundary layer. We installed three eddy-covariance stations in a grass field, a wheat field (see Figure 1.4), and on the edge between these fields to study heterogeneity effects. During this campaign, radio-soundings were performed intensively at a meteorological site at 500 m distance from the fields. Both the FLUXPAT and the BLLAST dataset have a well-defined surface heterogeneity.

2

Sensitivity and uncertainty of analytical footprint models according to a combined natural tracer and ensemble approach

Evaluations of analytical footprint models using data from several stations located in different land use types are still scarce, but valuable for defining the spatial context of the measurements. Therefore, we evaluated two analytical footprint models by applying a 'forward' and an 'inversion' method. We used eddy covariance measurements from a flat agricultural landscape in western Germany in the summer of 2009, with seven eddy covariance systems over three different land use types with contrasting sensible heat fluxes. We found that the model of Hsieh et al. (2000, Adv. Water Resour. 23, 765-772) and of Kormann and Meixner (2001, Bound.-Lay. Meteorol. 99, 207-224) are both overestimating the distance of the peak contribution of the footprint. In our evaluation, the former model performs slightly better, independent of whether the crosswind dispersion was used from the latter model, or from the proposed model by Detto et al. (2006, Water Resour. Res. 42, 1-16).

This chapter is published as van de Boer et al. (2013).

2.1 Introduction

The large horizontal variability of the energy and gas exchange down to very small scales, and especially the representation of gas exchange in land-surface models, still poses major problems. Long term monitoring networks have been established during the last decades to determine trace gas fluxes between terrestrial surfaces and the atmosphere, e.g. FLUXNET (Baldocchi et al., 2001), AMERIFLUX and CARBOEUROPE. The eddy covariance (later referred to as EC) method is widely used to quantify land-atmosphere exchange of carbon dioxide and water vapor. However, EC systems measure fluxes at field to catchment scale, which implies that the measured flux often originates from a mixture of land use types. Footprint models (Schmid, 2002) aim at predicting the contribution of different parts of the surface to a measured flux or scalar concentration.

Although footprint models are frequently used to determine the homogeneity of the footprint of EC-measurements, little is known about their validity and accuracy. The use of artificial tracer gases, natural sources of scalars, and isolated heterogeneities for footprint model evaluation is discussed by Foken and Leclerc (2004). They point out that well designed experiments with natural tracers should be performed to investigate the application range for different footprint models, since those studies can often be included into on-going flux field campaigns. This was done by Reth et al. (2005) and Göckede et al. (2005) among others, who tested the suitability of natural tracer experiments in the evaluation of footprint models. Reth et al. (2005) attempted to use soil chamber measurements and EC data to evaluate footprint models. Göckede et al. (2005) compared soil chamber measurements with EC and scintillometer measurements with various footprints, using data from the same field experiment as Reth et al. (2005). During the past decades, research on footprint modeling has increased significantly. Different types of methods have been developed by many researchers. Pasquill (1972) simulated the transfer between downwind observations and two-dimensional upwind sources analytically. The advantage of an analytical footprint model is its ability to describe the horizontal distribution of source weight with one or two equations and a manageable amount of parameters. The parameters can typically be computed from measurement height, roughness length, atmospheric stability and crosswind variance.

Analytical footprint models in the strict sense are analytical solutions of the advection-diffusion equation (e.g. Gash, 1986; Schmid and Oke, 1990; Schuepp et al., 1990; Horst and Weil, 1992; Schmid, 1994; Stannard, 1997; Horst, 1999; Haenel and Grünhage, 1999; Kormann and Meixner, 2001). The flow field in analytical footprint models is implicitly calculated using either (quasi) logarithmic profiles from MOST (Monin-Obukhov similarity theory) or power law profiles. The crosswind dispersion is described as a Gaussian plume. As an improvement to such analytical models, an approximate analytical model was developed by Hsieh et al. (2000). Their model is based on a combination of Lagrangian stochastic dispersion model

results and dimensional analysis. It does not contain a crosswind distribution in its original form, which is a prerequisite for the kind of application and evaluation our study aims at. However, it can be combined with the crosswind distribution in the frequently used model of Kormann and Meixner (2001) as well as with a crosswind distribution suggested by Detto et al. (2006).

Lagrangian stochastic dispersion models (e.g. Kljun et al., 2002) and LES-based models (e.g. Steinfeld et al., 2008) have been developed as well. However, computations in those types of footprint models are time consuming. The approximate analytical parametrization by Kljun et al. (2004) would be interesting to include in a comparison because of its ability to predict downwind contributions. However, the model does not yet include a published crosswind distribution for these downwind contributions.

Here, we test two frequently used analytical footprint models and various ways to obtain their required input data on a set-up that allows for extensive natural tracer experiments. We deliberately focus on sensible heat flux because it depends (apart from the Schotanus correction) on one sensor only, which is the same providing all other footprint-relevant turbulence data; the sonic anemometer. Other scalar fluxes are known to fail quality tests more often than sensible heat fluxes. Furthermore, we will use a dataset from a landscape with different land use types, but without heterogeneities in orography or roughness which would affect the mean flow in a direct way and to a high degree. With the present study, we hope to contribute to the proper use and further development of footprint models used over sites with several land use types, for EC flux data quality control, validation of new instruments (e.g. scintillometers and chambers), or for dis-aggregation by inversion (Hutjes et al., 2010). In this study, we build on the suggestion of Foken and Leclerc (2004) to include a footprint evaluation in a larger field experiment. Seven EC sensor pairs (sonic anemometers and gas analyzers) at locations implying footprints with differences in the main land use type were operated in a landscape dominated by a mosaic of three land use types. In this way, the natural tracer evaluation concept can be extended to a dataset where different footprint model properties (e.g. upwind and crosswind extension) become important in different situations (e.g. wind direction and stability).

Within the core of our study, a forward application of the footprint model of Hsieh et al. (2000), hereafter referred to as HKC00, is used to predict fluxes at the border station, which is located in the most heterogeneous surrounding. For this purpose, the HKC00 model is combined with a land use map. EC data were used to determine the representative fluxes of the three dominant land use types in the measurement area. These fluxes were multiplied with contributions of the corresponding land use type in the calculated footprint of the border station. The predicted fluxes at the border of the two fields were evaluated with flux measurements from the border station.

This evaluation method is repeated systematically using the model of Kormann

and Meixner (2001), hereafter referred to as KM01. Furthermore, the sensitivity of the evaluation results to different choices of parameterizations and input variables is investigated. These runs include the parametrization of crosswind distribution, surface roughness, and atmospheric stability. Moreover, we will give a brief example of solving the evaluation problem with an inversion approach, which estimates fluxes for each land use type from all measured fluxes and modeled footprints for each station, rather than assuming any of the stations to deliver ‘pure’ surface fluxes of a single land use type. Together, these approaches aim at answering the following questions:

1. Can we identify, by reference to the **natural tracer experiment**, certain recommendations on the implementation of the approaches presented by HKC00 and KM01? (Section 2.5.2)
2. Is the footprint model **uncertainty** related to
 - the crosswind distribution,
 - surface roughness of an area with different land use types,
 - atmospheric stability in an area with different land use types?(Section 2.5.2 and 2.5.3)
3. Does an **ensemble average** derived from different model combinations and input parameterizations improve our forward evaluation results? (Section 2.5.4)
4. Is **inversion**, as suggested by Neftel et al. (2008) and Hutjes et al. (2010), robust enough to serve as an alternative way to determine ‘pure’ land use fluxes? (Section 2.5.5)

We will first describe the two footprint models (HKC00 and KM01), our implementation of the models, and the method to obtain footprint weights of each land use type in Section 2.2. In Section 2.3, we describe the evaluation methods and the sensitivity analyses. A description of the measurements, the data processing and the measurement area is given in Section 2.4. In Section 5.4, results will be shown characterizing the meteorological conditions, the model evaluation, the sensitivity analysis, and the ensemble evaluation. Conclusions are given in the final Section 2.6. Equations used in this study can be found in 2A.1 (footprint models) and 2A.2 (surface layer similarity).

2.2 Model description

2.2.1 HKC00 and KM01

The parameters in the models proposed by HKC00 and KM01 are determined explicitly from micro-meteorological parameters (see 2A.1 for equations used in the

footprint models). The model by HKC00 requires roughness length (z_0), Obukhov length (L) and aerodynamic measurement height (z_m , height above displacement height) as input to determine its shape parameters (cf. Equation 2A.1). A rougher surface, a more unstable atmosphere, and lower sensors all result in a smaller footprint. The model returns the crosswind integrated source weight as a function of upwind distance (x). The crosswind distribution later added by Detto et al. (2006) additionally requires the standard deviation of crosswind speed (σ_v , Equation 2A.5) and the friction velocity (u_*). The crosswind integrated part of KM01 (cf. Equation 2A.2) also requires z_0 , L and z_m (see Table 2.1). The crosswind distribution part of KM01 (Equation 2A.3) only requires σ_v as extra input.

Figure 2.1 shows crosswind integrated flux footprints for both models (after Equation 2A.1 and 2A.2) for two different atmospheric stability cases. The input data chosen represent a daytime and night-time situation which are inspired by our measurement data. The figure clearly shows the main difference between the two models for unstable conditions. For the unstable case, the peak contribution according to HKC00 is located 12 m closer to the instrument, and is one and a half times higher than the peak modeled by the function of KM01. When comparing the KM01 model with their backwards in time Lagrangian stochastic dispersion model, Kljun et al. (2003) found that the upwind tail of the KM01 footprint was heavier than their tail. We also included the parameterized footprint model by Kljun et al. (2004) (not shown). Although the model by HKC00 gives a lower tail than KM01, it is still relatively high compared to Kljun et al. (2004).

For the stable case, the peak contributions predicted by HKC00 and KM01 are very small and occur at less different locations, and tails are much longer than for the unstable case. The peak locations of both models differ less than 10% for this case. The dependence on stability within a stability regime (stable or unstable) is different for both models. HKC00 shows a stronger dependence on z/L than KM01 (not shown). Also the dependence on surface roughness (not shown) is different. The KM01 model is more affected by a changing z_0 . In Figure 2.2a, a Gaussian crosswind dispersion function is shown. The second part of Figure 2.2 shows the increase of the crosswind width parameter σ_y (depending on crosswind standard deviation and u_* , Equation 2A.4 and 2A.5) with upwind distance for the crosswind dispersion functions of KM01 and Detto et al. (2006). The specification of σ_y is the only difference between the two Gaussian crosswind dispersion functions. Further away from the station, the difference between the two crosswind functions increases, and the function of Detto et al. (2006) results in more crosswind dispersion than KM01 for both the day and night time case.

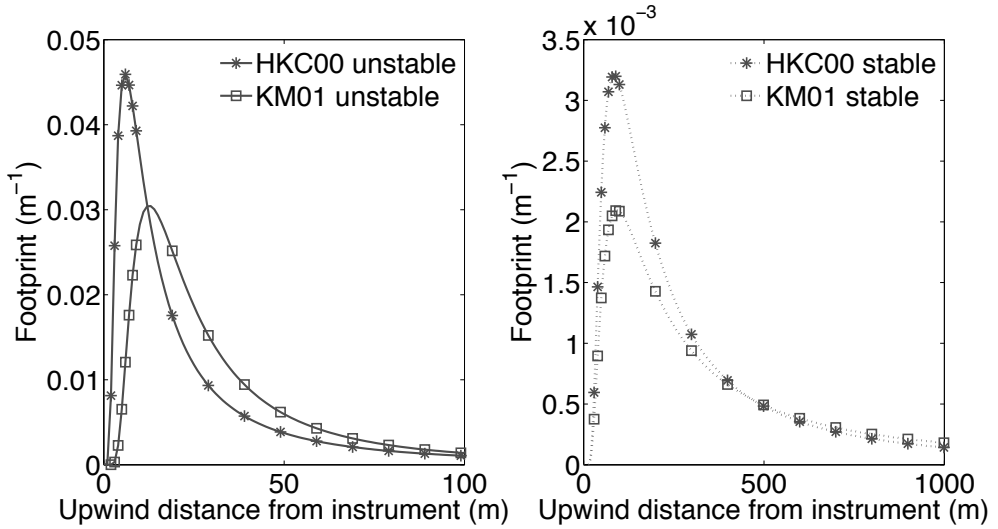


Figure 2.1: Longitudinal distribution function of KM01 and HKC00 for a typical unstable situation ($z/L = -0.44$, $z_0 = 0.05\text{m}$, $u_* = 0.22\text{ms}^{-1}$, $U = 1.8\text{ms}^{-1}$), and a stable situation ($z/L = 1.13$, $z_0 = 0.05\text{m}$, $u_* = 0.05\text{ms}^{-1}$, $U = 1.2\text{ms}^{-1}$). Note that the values on the axes are different for both cases.

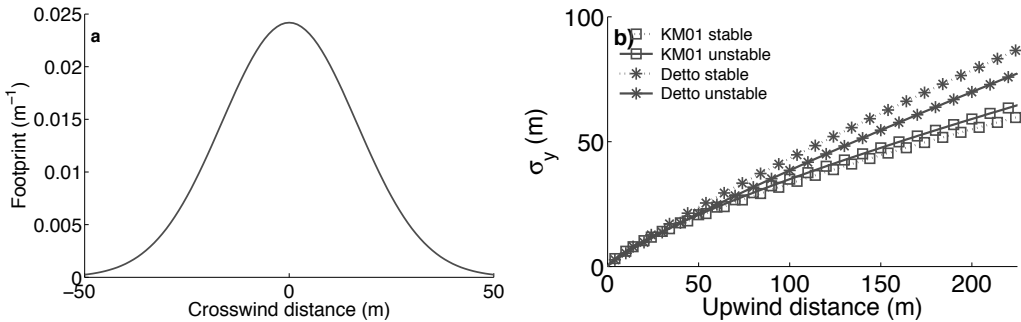


Figure 2.2: a) Crosswind distribution function at upwind distance of the peak location. Peak locations are 18, 93, 6 and 84 m for KM01 unstable, KM01 stable, HKC00 unstable and HKC00 stable respectively. b) Crosswind width, described by KM01 and Detto et al. (2006), depending on upwind distance, for the same unstable and stable situation as in Figure 2.1, with $\sigma_v = 0.83$ and 0.21ms^{-1} respectively.

2.2.2 Our implementations

Determination of roughness length

In a widespread implementation of the KM01 model (Neftel et al., 2008), the observed wind speed (U) together with the variables z_m/L and u_* are used to determine z_0 (Equation 2A.7), rather than using a fixed estimate of z_0 . By doing so, the z_0 value that would be consistent with the observed combination of U , u_* , and L

2.2. MODEL DESCRIPTION

Table 2.1: Footprint model input for the original models and our implementations. HKC, KM and Det indicate our implementations of respectively the alongwind part of HKC00, the alongwind or crosswind part of KM01, and the crosswind function described by Detto et al. (2006). ✓ indicates that the parameter is required for the given implementation.

Input	Original				Our implementations		
	Longitudinal		Crosswind		HKC-KM	KM-KM	HKC-Det
	HKC00	KM01	Det	KM01			
u_*	-	-	✓	-	✓	✓	✓
z_0	✓	✓	✓	✓	-	-	-
L	✓	✓	✓	✓	✓	✓	✓
z_m	✓	✓	✓	✓	✓	✓	✓
σ_v	-	-	✓	✓	✓	✓	✓
U	-	-	-	-	✓	✓	✓

can be used to detect violations of the assumptions underlying the model, in particular MOST. We calculate z_0 using Equation 2A.7 (Neftel et al., 2008) in our three implementations of the models (see Table 2.1 how the model input differs). Records yielding values outside the range 1×10^{-4} to 0.2 m were adapted to these limits. We analyze the effect of z_0 by also using fixed estimates of z_0 for footprint calculations in two members of our ensemble study.

Discretization

To assign the flux contributions to different land use types, the source weight function (footprint), the position of the EC station, wind direction (U_{dir}) and a land use map are required. Neftel et al. (2008) integrated the footprint density function over a defined surface area given as quadrangular polygons representing the fields. In contrast, we used grid information of the land use types to compute the integral footprint weight of each land use type. This grid information is more easily applicable to arbitrary field shapes. However, the resolution at which the source weight function is discretized is imposed by the resolution of the land use map. Therewith, a certain minimum resolution is required to properly integrate the dispersion function.

In a series of numerical experiments, we found that for our conditions the footprint models need a spatial resolution roughly equal to the measurement height for unstable atmospheric stratifications. Using a coarser resolution will lead to a wrong description of the sharp peak contribution close to the station. Furthermore, the integral of the discretized footprint function can differ significantly from one (up to 10% for $\Delta x = 8 z_m$) in case the function is under-resolved.

Construction of 2-D footprint model

A combination of the longitudinal part of HKC00 and the crosswind part of KM01 was chosen for our reference footprint model. Comparison results of Kijun et al. (2003) show a disadvantage (mentioned in Section 2.2) of using KM01. On the other

hand, HKC00 initially did not include a crosswind distribution function; therefore we use the one of KM01. The choice of the reference run RefHKC-KM does not imply any appraisal at this point, but is owed to the requirement of one central combination from which only one element at a time is changed in the model runs, which is described in more detail in Section 2.3.2. Detto et al. (2006) propose a crosswind function for the HKC00 model, which is used in one of the configurations of footprint model functions and input (given in Section 2.3.2). Hereafter, HKC, KM and Det indicate our implementations of respectively the alongwind part of HKC00, the alongwind or crosswind part of KM01, and the crosswind function described by Detto et al. (2006).

2.3 Research strategy

The core of our study is the evaluation of our implementations of HKC00 and KM01 using a natural tracer experiment for sensible heat flux. We use two different evaluation methods; a forward method and an inversion method (Section 2.3.1). We tested the sensitivity (Section 2.3.2) to choices of model combinations (longitudinal and crosswind distribution) and input parameterizations (e.g. instantaneous estimates vs. long-term averages of roughness length) using our forward method. In order to give the uncertainty with respect to the choice of model components and input parameters we also evaluate the performance of an ensemble average (Section 2.3.3).

2.3.1 Footprint model evaluation

We used HKC-KM, KM-KM, and HKC-Det (see Table 2.1) to predict the measured flux at the border station, in order to evaluate the models. This border station is the station with the most heterogeneous surrounding, located in a barley field near the border with a sugar beet field (a more detailed site description is given in Section 4.3.2). We calculate H at the border station as:

$$F_{border} = \sum_{i=1}^I c_i \tilde{F}_i \quad (2.1)$$

in which F_{border} is the estimated flux at the border station, c_i is the fractional contribution of land use type i , I is the number of land use types, and \tilde{F}_i is the ‘pure’ flux of land use type i .

These estimates are compared to the measured flux (question 2). The footprint of the border station may be rather homogeneous in case the flux is resulting from the field it was installed in; barley regrowth. Therefore, we separately examined the 10% of the cases when the footprint contained the most sugar beet concentration.

We applied a forward (Section 2.3.1) and an inversion (Section 2.3.1) method to estimate the ‘pure’ fluxes \tilde{F}_i of all land use types.

Forward method

To estimate the ‘pure’ fluxes (\tilde{F}_i) using this method, we first applied RefHKC-KM to select those half-hours, where the lower levels of all three EC stations located in the middle of the fields had a flux contribution of more than 80% from their own target field:

$$\tilde{F}_i = F_j \mid c_i > 80\% \quad (2.2)$$

in which measured fluxes at station ‘j’ are indicated with F_j . It should be noted that this filtering unavoidably depletes atmospherically stable situations in the dataset, because these situations produce larger footprints.

To ensure that the model combinations are evaluated on the same dataset, the 80% input criterion was always determined according to the reference run ‘RefHKC-KM’ (see Table 2.2). The forward evaluation method was applied to each model combination, as well as to the other runs (described in Section 2.3.2).

Inversion method

The fluxes measured at the stations are acknowledged to contain contributions from different land use types. Hence, for the inversion method the ‘pure’ fluxes \tilde{F}_i are defined implicitly:

$$F_j = \sum_{i=1}^I c_{ij} \tilde{F}_i \quad (2.3)$$

where the modeled contribution of each land use type to each station is given by matrix c_{ij} , and the measured fluxes at each station (except for the border station) are indicated with F_j (question 3). This system (Equation 2.3) was solved in a similar way as suggested by Neftel et al. (2008) for two ground-based stations, or by Ogunjemiyo et al. (2003), Hutjes et al. (2010), and Metzger et al. (2012) for an arbitrary number of airborne measurement points.

Unlike in the Neftel et al. (2008) case, our system is overdetermined, with six included stations and three considered land use types, requiring regression as the solution strategy. At the same time, however, the relatively small degree of overdeterminedness as compared to the Hutjes et al. (2010) case does not allow for an application of robust statistics. Consequently, we used the ordinary least squares solution to determine the unknown ‘pure’ surface fluxes. Different from the forward approach, this approach does not require the 80% criterion for the input data. Hence, a larger part of the dataset can be used for the evaluation. However, inversion is more vulnerable to violations of the assumptions underlying analytical footprint models, as pointed out by Schmid (2006).

Table 2.2: Configuration of the different model setups. The first three runs are used for the model evaluation (results in Table 2.3), the other 7 are used in the sensitivity analyses (results in Table 2.4). The entire list of 10 runs is used in the ensemble average (results in Table 2.5).

Run	Longit. model	Crossw. model	z/L source	z_0 source
RefHKC-KM	HKC	KM	border	border
KM-KM	KM	KM	border	border
HKC-Det	HKC	Det	border	border
AreaAvg ^a	HKC	KM	average	average
MostStable ^b	HKC	KM	highest z/L	border
MostUnstab ^b	HKC	KM	lowest z/L	border
BorderZ ₀ ^c	HKC	KM	border	0.02 m
SugBeetZ ₀ ^c	HKC	KM	border	0.07 m
CorWD ^d	HKC	KM	border	border
Hact ^e	HKC	KM	border	border

^a Averages are taken of u_* , H_V and U of the 7 EC-systems. From those, area average z_0 and z/L were determined.

^b The quartiles and median for z/L for *MostUnstab* are -0.63, -0.15 and -0.01, and for *MostStable* -0.05, 0.01 and 0.72 (without selection for heterogeneity).

^c 0.02 m is the most frequently observed z_0 at the border station in August 2009. 0.07 m is the most different frequently observed z_0 , measured at the sugar beet field in August 2009.

^d A correction of -6° , the deviation from the median of the 7 systems, was applied to the wind direction measured at the border station.

^e The actual instead of the virtual sensible heat flux was taken for the footprint calculations.

2.3.2 Sensitivity analysis and specification of the ensemble

The model evaluation tests the dependence of the model performance on the choice of model components: HKC or KM for the alongwind component, and KM or Det for the crosswind component. For our sensitivity analysis, we varied the input parameters one at a time (Table 2.2). Different values were used for L because of its large variation between the different fields and because of its impact on footprint size. In the reference run we used L calculated from measurements at the border station. In the runs ‘MostStable’ and ‘MostUnstab’, we used the most stable (typically the least unstable) and the most unstable (sometimes the least stable) z/L respectively. Moreover, one model run is based on the determination of z/L (and z_0) from the area averaged u_* , H_V and U (‘AreaAvg’). The effective area average of z/L (and of z_0) was computed from the arithmetic averages of u_* , H_V and U from all (7) EC-systems for every half hour of data.

Since the roughness length is calculated for each interval as a function of observed thermal and aerodynamic parameters (Neftel et al., 2008), unnecessary and unrealistic variability may be introduced. Because a change in the roughness length affects the features of the footprint, other footprint models (e.g. HKC00) use the assumption that the roughness length has a fixed value of for example 10% of the

vegetation height. However, potential real time-variability and direction dependence are not taken into account using this assumption. To quantify the effect of a constant z_0 , we use two runs with two different constant mostly observed values at the two most different stations ('Border Z_0 ' and 'SugBeet Z_0 ', question 4). Furthermore, we use an area average z_0 in the run 'AreaAvg' (calculated from the arithmetic averages of u_* , H_v and U).

We also deal with the fact that the wind direction was not exactly the same for all the 7 EC-systems due to small differences in alignment. We corrected the wind direction at the border station with -6° , which is the mean deviation of the border station from the median of the 7 systems. The last run is related to the heat flux used in the Obukhov length L (Section 2A.2). In principle, this should be the virtual sensible heat flux. However, some past studies used the actual sensible heat flux, which might have affected the usual parameterization of universal functions. Therefore, we include a run 'Hact', in which we used the actual sensible heat flux (see Table 2.2).

2.3.3 Ensemble average

In the sensitivity analysis we perform a number of runs, but it is not a priori clear which permutation is correct. Therefore, we created an ensemble out of all members given in Table 2.2. An ensemble average (and associated variances) were calculated from the contributions of the members. To see if an ensemble out of different model and input choices provides a better flux estimate than the reference run, the evaluation method mentioned in Section 2.3.1 was applied to the ensemble average:

$$F_{border} = \frac{1}{M} \sum_{i=1}^I \sum_{m=1}^M c_{im} \tilde{F}_i \quad (2.4)$$

where an average is taken over a number of M ensemble members (given in Table 2.2).

2.4 Data

2.4.1 Experiment

Eddy covariance data used in this study were collected within the Transregio 32 FLUXPAT campaign in summer 2009 near Merken, Germany ($6^\circ 24'E$, $50^\circ 50'N$, 114 m asl), see e.g. Graf et al. (2010). Three stations with EC sensors at 6.0 m and at 2.5 m were installed in the middle of a field containing one of the three dominating crops: winter wheat, winter barley and sugar beet. Each EC system consisted of a fast response 3D sonic anemometer (CSAT3, Campbell Scientific, Logan, UT, USA), and an open-path infra-red gas analyzer (LI-7500, LI-COR). A border station was installed with sensors at 2.5 m height, in a barley field 50 m away from its border with a sugar

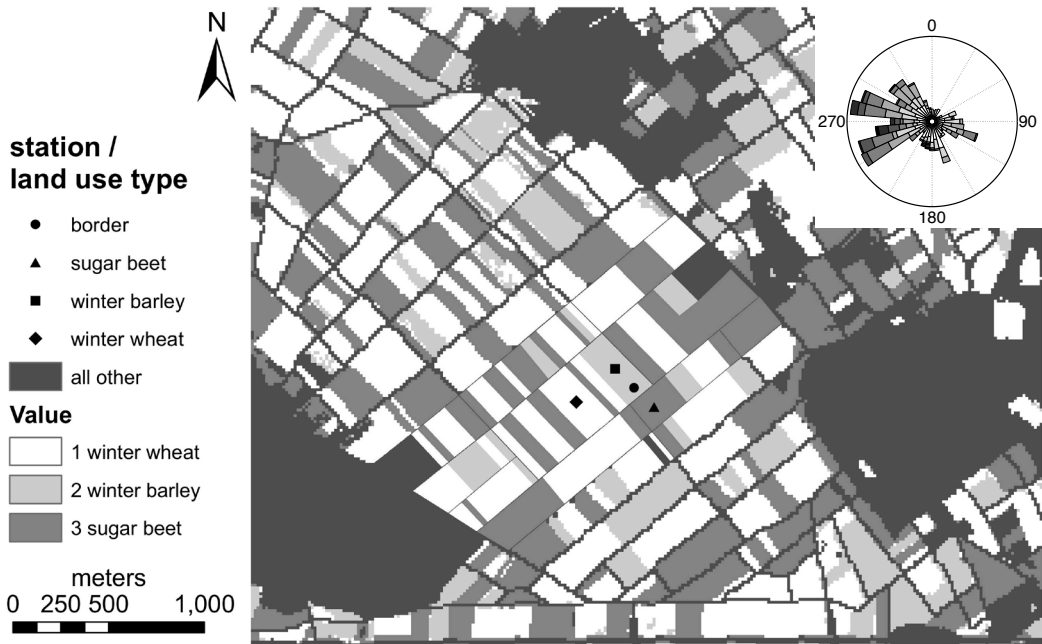


Figure 2.3: Land use map of the study area with locations of the four EC stations in Merken (Germany), and a wind rose of daytime measurements with wind speeds between 0 (light grey) and 8 ms^{-1} (dark), both of August 2009.

beet field. As a result, this station has a more heterogeneous footprint for certain wind directions. Figure 2.3 gives an overview of the locations of the EC-stations, and of the wind directions for the daytime data. The study region was chosen, among other reasons, for the fact that spatial flux variability in the footprint of the stations is dominated by sharp contrasts between few land use types (Figure 2.3), rather than gradual changes due to soil properties or other resources. At a radius of 700 m around the EC stations, the terrain is flat with a maximum slope of less than 0.7° . No ditches and no plants higher than the mapped crops were found, and the soil texture is uniform within this area (silt loam). Comparing chamber measurements between juvenile sugar beet and fully growing wheat in the spring of 2008 yielded differences in soil CO_2 efflux between the fields twice as high as the 95% confidence interval of spatial variability within each crop (Graf et al., 2011).

Data from all anemometers and gas analyzers were logged at 20 Hz. The azimuth angle of the anemometers in the three fields was 230° , and the angle of the anemometer at 2.5 m close to the border was 135° . Data from 4 to 27 August 2009 were used for this study. The barley field had already been harvested before August, however another canopy from weeds and new barley seedlings, scattered and with a maximum height of about 0.1 m, had developed in August. This field is therefore be called ‘barley-regrowth’. The wheat field was harvested at the 3rd of August and

are called 'wheat residual', and the sugar beet field was harvested after August. The height of the sugar beet plants was 0.68 m throughout August. We used a displacement height of zero for the wheat residual and barley regrowth, and a displacement height of $d=0.51$ m for the sugar beets.

2.4.2 Processing

The 20 Hz raw data were processed to yield 30-minute average fluxes with the software ECpack (van Dijk et al., 2004). A planar fit tilt correction (Wilczak et al., 2001) was performed with tilt angles determined over periods of 5 to 12 days, depending on the maintenance dates. Linear trends were removed, and the Webb-correction (Webb et al., 1980) was carried out. The Schotanus correction (Schotanus et al., 1983) was applied to correct for humidity effects on the temperature. Raw data points flagged by the instrument were eliminated, and 95% confidence intervals were estimated by quantifying the sampling error for each scalar average and flux following van Dijk et al. (2004). Half-hours with sensible heat flux confidence intervals larger than 20 Wm^{-2} were removed.

2.4.3 Land use map

Depending on stability, either the coverage of a large area (stable conditions), or a high resolution near the stations (especially unstable conditions) may become critical (explained in Section 2.2.2). In order to satisfy both requirements, our land use map was merged from two different sources. The station locations, crop types and corner points of all fields surrounding the stations to a distance of at least 300 m, were manually surveyed with a differential GPS (GPS-702/Propak V3, NovAtel, Calgary, Alberta, Canada), which assures an accuracy in the cm range. The resulting vector dataset was converted to a 1 m resolution grid and amended to a distance of at least 1 km from the stations with a satellite based land use classification with an effective resolution of 15 m. This classification was based on ASTER and RapidEye data (see Waldhoff, 2010). Each grid point of the combined dataset was assigned to one of the land use types winter wheat, winter barley, sugar beet, maize, road, water, and other, but only the first three crop types and the sum of weights from all points assigned to any other land use type are important within the framework of this study. The combined map is shown together with the location of the stations in Figure 2.3. Domains of 2400×2400 m around each EC-system were selected as square subsets of the map for the actual calculation of the footprint.

2.5 Results and discussion

2.5.1 Meteorological conditions and eddy covariance fluxes

Figure 2.4 shows the sensible and latent heat fluxes as observed over the different fields during the experiment. Sensible heat fluxes were highest at the harvested wheat field, with peaks of 300 W m^{-2} , and latent heat fluxes were highest at the sugar beet field, with peaks of 350 W m^{-2} . From the flux differences between the wheat and barley field, we can derive that the young and new barley canopy is already contributing a significant amount of transpiration to evapotranspiration. Hence, the daytime Bowen ratios and sensible heat fluxes can be put into the order wheat residual > barley regrowth > sugar beet, and three considerably different flux magnitudes are used in the footprint model evaluation.

The four stations measured similar temperatures and wind directions. The measurement area was characterized by relatively dry summer weather in August 2009, with a mean maximum air temperature of 26.9°C , a mean minimum air temperature of 14.8°C , with only 5 days of rain, and with winds coming from the west mainly (see Figure 2.3 and 2.4). This implies that the footprint of the border station did not generally include the closest sugar beet field at the south east of the border station.

A period of fair weather can be found between day of the year (DOY) 216 and 219, when the winds mainly came from the southeast during the day. The wind also came from the southeast at DOY 230-232 and 235-236, which implies that those days are characterized by a heterogeneous footprint for the border station, containing a considerable sugar beet contribution. However, we can conclude from Figure 2.3 and 2.4 that the barley-regrowth field acts as the main source in the footprint of the border station for most of the days. For those cases, the footprint of the border station can not be ideally heterogeneous, which confirms that the unpredictability of the wind direction is a disadvantage of natural tracer experiments.

Some light rain events occurred at DOY 214, 225, 233 and 238, and a heavy rain event occurred at DOY 220, which can be seen in Figure 2.4. Logically, latent heat fluxes increase after a rain event, which decreases the contrast between the wheat-residual and the sugar beet fluxes significantly. Hence, using fluxes from periods after a rain event (similar fluxes for all fields) for our evaluation might lead to a trivial result for those data points.

2.5.2 Footprint model evaluation: Forward method

Figure 2.5 shows the evaluation of predicted fluxes of the two analytical models (both combined with the KM crosswind dispersion) with measured sensible heat fluxes from the border station for the full dataset. 'Pure' fluxes were estimated using the forward method described in Section 2.3.1. Most of the stable data do not meet the 80% criterion and were therefore filtered out. Using the full KM01 model

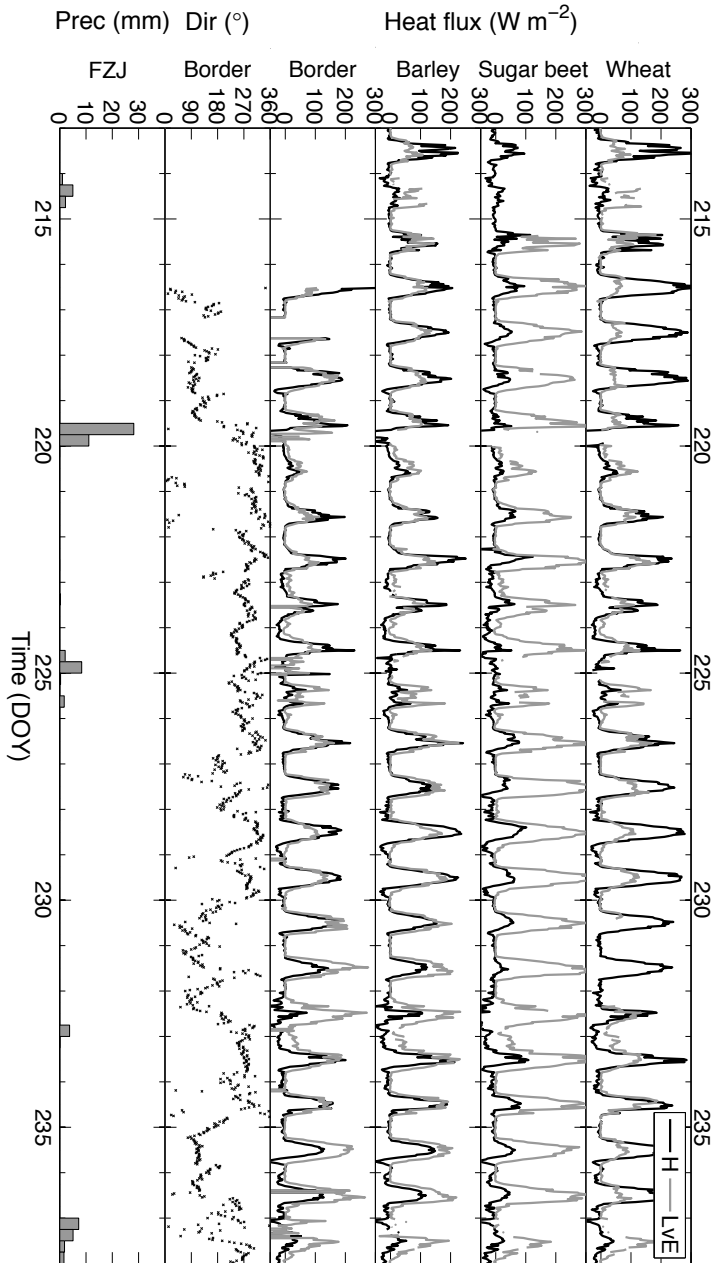


Figure 2.4: From top to bottom: sensible (H) and latent (L_vE) heat fluxes measured at the EC-station at 2.5 m in the wheat residual, sugar beet, barley regrowth, and at a station close to the border between the sugar beet and barley regrowth, respectively. The wind direction is measured at the border EC-station, and precipitation (shown cumulative over 6 hours) is measured at the Research Centre, close to Merken.

(KM-KM) instead of HKC-KM, we found a very slight degradation (from 0.95 to 0.94)

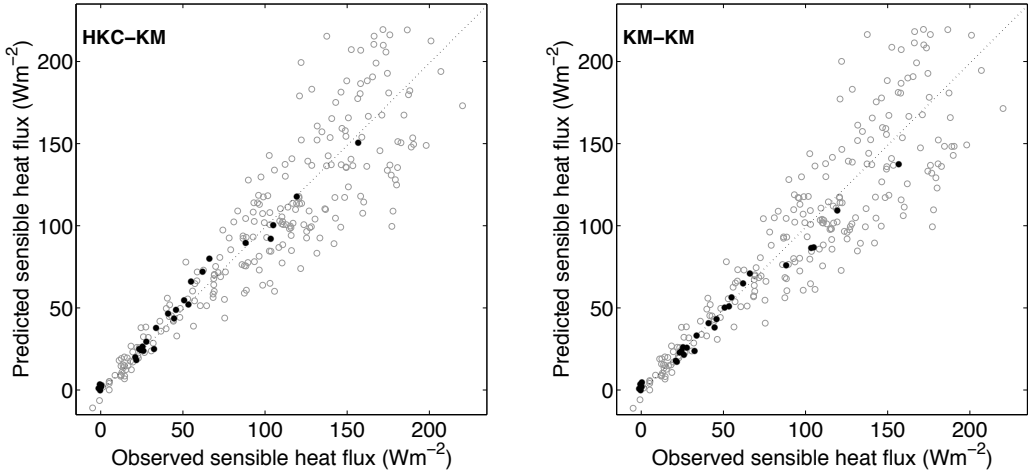


Figure 2.5: Evaluation of sensible heat fluxes estimated using a combination of HKC00 and KM01 and of KM01 only, with measurements from the border station. Black dots indicate heterogeneous data as identified by a minimum sugar beet contribution (see text). The 1:1 line is given dashed.

Table 2.3: Evaluation of different model combinations, evaluated for different data selections (heterog. indicates filtered data with a minimum sugar beet contribution to the border footprint)

Run	Data	slope	offset	R^2	N
		-	Wm^{-2}	-	-
RefHKC-KM	all	0.95 ± 0.03	3.1 ± 2.8	0.84	267
KM-KM	all	0.94 ± 0.03	2.5 ± 2.9	0.83	267
HKC-Det	all	0.95 ± 0.03	3.1 ± 2.8	0.84	267
RefHKC-KM	heterog.	0.96 ± 0.03	2.7 ± 1.6	0.98	27
KM-KM	heterog.	0.87 ± 0.02	2.6 ± 1.3	0.99	27
HKC-Det	heterog.	0.96 ± 0.03	2.7 ± 1.6	0.98	27

of the slope. Also, R^2 is slightly lower. The difference is however not significant (see Table 2.3 for regression results). We also see that it does not matter much which of the two crosswind functions is chosen for HKC.

Next we applied regression analysis on the 10th percentile of data with the highest sugar beet contributions (explained in Section 2.3.1), which corresponds to a minimum contribution larger than 16.2% in the reference run RefHKC-KM. We see that for KM-KM, the data points for which the footprint model matters most show an underestimation of the sensible heat flux. The slope of the regression fit for only heterogeneous data, which is only shown in Table 2.3 and not in the Figure, increases for this sub-dataset to 0.96 ± 0.03 for RefHKC-KM, but decreases to 0.87 ± 0.02 for KM-KM. The large R^2 values found for the heterogeneous sub-dataset might be caused by the fact that the selection for heterogeneity only includes data from similar days. Varying the minimum criterion for the sugarbeet contribution and thus the size of

Table 2.4: Evaluation of different runs explained in Table 2.2, evaluated only for the heterogeneity data selection

Run	slope	offset Wm ⁻²	R ²	N
	-		-	-
RefHKC-KM	0.96 ± 0.03	2.7 ± 1.6	0.98	27
AreaAvg	0.96 ± 0.03	2.8 ± 1.6	0.98	27
MostStable	0.94 ± 0.03	2.0 ± 1.6	0.98	27
MostUnstab	0.97 ± 0.03	2.6 ± 1.5	0.98	27
BorderZ ₀	0.97 ± 0.03	2.6 ± 1.6	0.98	27
SugBeetZ ₀	0.99 ± 0.03	2.8 ± 1.7	0.98	27
CorWD	0.97 ± 0.03	2.8 ± 1.6	0.98	27
Hact	0.95 ± 0.03	2.2 ± 1.5	0.98	27

the heterogeneous sub-dataset (not shown) yielded considerable differences in the overall performance (e.g. slopes and R^2) of all runs, but the relative performance of runs compared to each other remained conserved. This finding also applies to most results presented in the following sections.

Since sensible heat fluxes were generally much lower at the sugar beet field compared to the barley-regrowth and the wheat-residual field, an underestimation of the border station sensible heat flux indicates that a too large sugar beet contribution was estimated by the footprint model. This is the case for all runs considered so far, especially KM-KM. If we combine these results with the land use map in Figure 2.3, we can derive that this can be explained by the extent of the footprint. The peak contribution is located further from the instrument according to KM01 compared to HKC00 (Figure 2.1). For winds from the south-east, KM-KM will therefore predict larger contributions of sugar beet than the other runs. It should be noted that the criteria of a considerable sugar beet contribution in the border station footprint, and of >80% target field contribution to each center station, are somewhat conflicting. Heterogeneous footprints of the border station installed 50 m from the border, in the barley field, should partly capture the sugar beet field, whereas the footprints of the other stations should be small enough to be mostly located in one field. However, flux measurements from the border station which remain after this selection are equally spread between 0 and 200 Wm⁻².

2.5.3 Footprint model sensitivity to input parameters

Regression results of the evaluation of different input parameters (mentioned in Section 2.3.2) are given in Table 2.4. We only present the sensitivity evaluations using the most heterogeneous border footprints, since regression results without this heterogeneity selection are less different among the different runs. This is due to the fact that for the full dataset, most points have a homogeneous footprint which makes the evaluation insensitive to the exact details of the footprint model. Even for the heterogeneity selection, slope differences are only significant between the

Table 2.5: Evaluation of the ensemble average from all members explained in Table 2.2, evaluated for two different data selections (all data and only heterogeneous data)

Run	Data	slope	offset	R^2	N
		-	Wm^{-2}	-	-
RefHKC-KM	all	0.95 ± 0.03	3.1 ± 2.8	0.84	267
EnsAvg	all	0.95 ± 0.03	3.0 ± 2.8	0.84	267
RefHKC-KM	heterog.	0.96 ± 0.03	2.7 ± 1.6	0.98	27
EnsAvg	heterog.	0.95 ± 0.03	2.6 ± 1.5	0.98	27

most extreme results.

Using the most stable stability parameter from the four EC-stations (measured over sugar beet) leads to larger footprints and a poorer fit ('MostStable'), which is in agreement with the overestimation of sugar beet contributions. We found that this result also applies for the model combination HKC-Det, but it does not apply for the model combination KM-KM (not shown). A fixed roughness length which corresponds with the sugar beet field ('SugBeetZ₀') instead of the area around the border station (mainly barley-regrowth), results in a slope insignificantly different from 1 (see the regression slopes in Table 2.4).

The other changes in input parameterizations do not significantly improve or decline the footprint model results; using averaged stability and roughness parameters from the four stations ('AreaAvg') does not change performance. Applying the most unstable stability parameter does hardly change the model performance. This is probably due to the fact that the border station was among the most unstable stations. Furthermore, using a fixed roughness length from the border station itself is not significantly better than calculating z_0 after Neftel et al. (2008) for every half hour of data. Moreover, a small correction for the wind direction due to small alignment differences between the stations does not significantly change the results using the more heterogeneous footprints ('CorWD'). Using the actual sensible heat flux instead of the virtual sensible heat flux for L also does not significantly change the slope, and R^2 ('Hact').

2.5.4 Footprint model ensemble average

The evaluation of the ensemble average is shown for the full dataset in Figure 2.6. Errorbars are given according to 95% confidence intervals; for the horizontal bars they are estimated by ECpack (see Section 4.3.2), and the vertical bars are calculated from the standard deviations within the ensemble. We see that errors in observations and in predictions are both not negligible; predictions may be expected to additionally be affected by the flux measurement errors of the three stations in the field centers (not shown).

The ensemble average does not improve the outcome of the evaluation com-

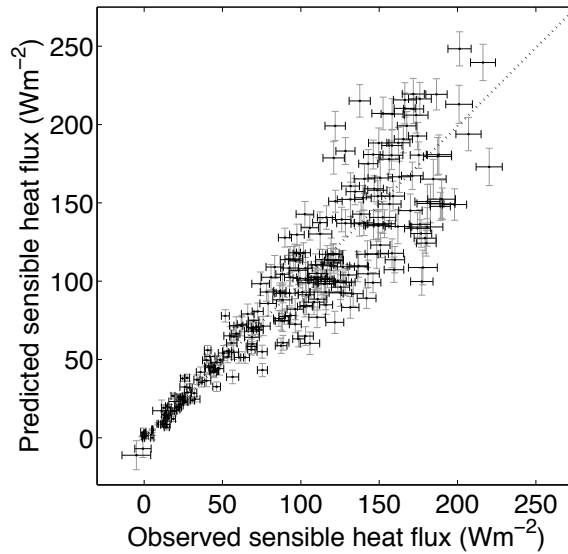


Figure 2.6: Evaluation of sensible heat fluxes estimated using the average of the 10 ensemble members given in Table 2.2, with measurements from the border station and without selection for heterogeneous data. Error bars show 95% confidence intervals from standard deviations within the ensemble (vertical), and from ECpack (horizontal). The 1:1 line is given dashed.

pared to the reference run RefHKC-KM, neither for the full, nor for the reduced dataset (see Table 2.5). According to our dataset, the ensemble of models and input is therefore only a helpful tool to indicate the uncertainty resulting from modeling decisions, but not to reduce this uncertainty. This result is however depending on the weight assigned to each ensemble member. In our case, all members account for 10% in the ensemble average, including the most deviating member (KM-KM). If the weights would have been different among the members, the ensemble average would behave differently. An alternative distribution of the weights would be: 25% for each of the three model variations discussed in Section 2.5.2, and 25% for the 7 runs with different input (mentioned in Section 2.5.3).

2.5.5 Footprint model evaluation: Inversion method

Figure 2.7 shows the evaluation of the HKC-KM combination using the inversion method. Unlike the forward method, near neutral and stable conditions remain, since no selection of ‘pure’ fluxes (measurements with homogeneous footprints) needs to be made. The regression line fits with $R^2 = 0.92$, and its slope is very close to one when using homogeneous and heterogeneous data. The same applies when using exactly the same 267 data points as for the non-heterogeneity filtered forward 80% criterion for reasons of consistency. When using the heterogeneous data (all data with a sugar beet contribution larger than 16.2%, which is consistent with the 10th percentile using the forward method), 364 points remain with a slope slightly

Table 2.6: Evaluation of HKC-KM, where ‘pure’ fluxes are derived after the inversion method, for different data selections (all data and only heterogeneous data, with and without the non-homogeneity filtering described in Equation 2.2)

Run	Data	slope	offset	R^2	N
		-	Wm^{-2}	-	-
Ref forward	all	0.95 ± 0.03	3.1 ± 2.8	0.84	267
Ref invers.	all	0.99 ± 0.03	2.0 ± 3.1	0.82	267
Ref invers.	all	1.01 ± 0.01	0.4 ± 0.7	0.92	867
Ref forward	heterog.	0.96 ± 0.03	2.7 ± 1.6	0.98	27
Ref invers.	heterog.	1.04 ± 0.05	-0.2 ± 2.7	0.95	27
Ref invers.	heterog.	0.97 ± 0.01	0.1 ± 0.4	0.93	364

lower than one, but which is still larger than follows from the forward method. A slope of 1.04 ± 0.05 results when using only the same heterogeneous data as for the reference forward run.

Due to the interactions between filter criteria, dataset size and model performance on the dataset, it is not save to conclude whether the inversion method is better or worse for calculating the fluxes from every land use type. The advantage of the inversion method is that more data remain, so that the evaluation of the footprint model can be made with more confidence (note the smaller error in the slope for the inversion method on the full dataset, as compared to the forward method (Table 2.6). However, it has been pointed out that footprint models may be overcharged by efforts to inversely determine fluxes (Schmid 2002, 2006). The systematic error introduced by the non-pure footprint is reduced, at the cost of increasing random errors (with respect to the originally measured fluxes).

2.6 Conclusion and outlook

This study presents a comparison of two-dimensional footprint models based on HKC00 (Hsieh et al., 2000), KM01 (Kormann and Meixner, 2001), and Detto et al. (2006). The main focus is the evaluation of these models through a natural tracer (here sensible heat) experiment over terrain with multiple land use types with contrasting sensible heat fluxes: Do the models predict the correct flux for a station that is influenced by a combination of land use types?

Based on a forward approach and all available data points, we found a slight underestimation of the estimated sensible heat fluxes compared to measurements for all model combinations. Due to our set-up, this indicates an overestimation of the footprint length. However, most data points did not contain significant contributions from the most deviating land use type (sugar beet). Selecting only the most heterogeneous footprints of the border (evaluation) station resulted in a negligible overestimation by the reference model RefHKC-KM and a significant underestima-

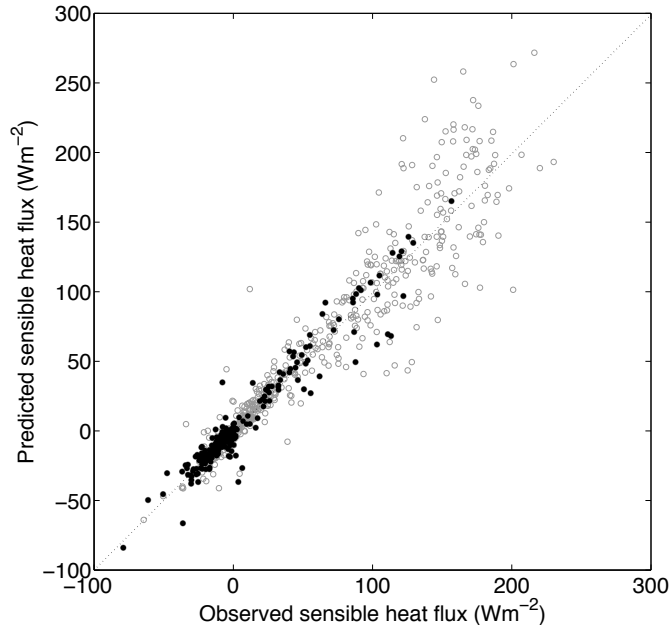


Figure 2.7: Evaluation of HKC-KM, where ‘pure’ fluxes are derived with the inversion method. Black dots indicate the heterogeneous sub-dataset). The 1:1 line is given dashed.

tion by KM-KM, which indicates an overestimation of the peak distance. The number of data points with such a heterogeneous footprint for the border station was very limited. For the forward evaluation approach and the encountered wind directions, a placement of the border station closer than 50 m to the border would have increased this sample size.

Compared to the ‘forward’ method, a substantial part of the systematic non-random deviations disappeared using the inversion method for HKC-KM. An additional advantage of the method is that the footprints of the fluxes from the individual fields (used as input) need not be homogeneous, so that more data remain. A disadvantage is that the footprint model has to be applied twice for this method. On the heterogeneity sub-dataset defined by a minimum sugar beet contribution to the border station and simultaneous data availability for the forward approach, the inversion approach yielded a slight flux overestimation by HKC-KM. Inversion seems however a promising method for future studies.

In the application of footprint models over terrains with different land use types, there is some uncertainty what the ‘effective’ values for stability and roughness should be. From our sensitivity analysis, we can conclude that the performance of the HKC00 model deteriorates if input parameters are chosen such that they increase the footprint length (e.g. a more stable z/L than observed at the station with the heterogeneous footprint). In contrast, the model results improved after applying a fixed but too high roughness length. We did not find a significant impact

of replacing H_v by H in the definition of L , of using area averaged values for z/L and z_0 , and of applying a small wind direction correction. Although we found an impact of the choices for z/L and z_0 , it remains unclear if the choices made for the reference run were correct, or that they were compensated by deficiencies in the footprint models themselves. In general, the choice of the input parameters appears to affect model results less than the choice of the model itself. Both footprint models depend on stability, but the model by KM01 has a weaker dependence on stability than HKC00. Unfortunately we do not have enough data to decompose the dataset into stability classes and evaluate the performance for each stability class separately.

For all evaluations, scatter might have been caused by a hypothetical imperfect homogeneity of the single fields and by the random errors of the measured fluxes. For the forward approach, additionally only relatively small footprints and mostly unstable situations remained after applying the 80% criterion that was required to confirm the purity of input fluxes measured by the field center stations. Furthermore, the set-up of the natural tracer experiment was not ideal concerning the wind direction during the experiment.

Altogether, the HKC00 model combined with the crosswind function from KM01 or Detto et al. (2006), form the best out of our tested footprint modeling approaches in our site conditions. However, to confirm the choice for the roughness length and stability to be used in the determination of the footprint, natural tracer experiments need to be repeated at more sites with different conditions, including an even more balanced mix of land use types in the footprint of at least one station. Our study is restricted to measurements in the lower part of the surface layer, and to non-complex terrain conditions where scalar flux contrasts are the only source and type of major heterogeneity. Furthermore, the evaluation needs to be extended to other scalar fluxes, notably those of moisture and CO_2 . Since these involve an additional instrument, typically reducing the amount of high-quality data, it is important to operate multi-station set-ups not only within campaigns, but also on long-term sites, as has already been suggested for other reasons (Mahrt, 2010).

2A Appendices

2A.1 Footprint model equations

The crosswind integrated footprint function at upwind distance x and height z_m ($z_m = z - d$, in which z is the height of the instrument above the surface, and d is the displacement height of 75% of vegetation height in our study) is in HKC00 described by:

$$f_{\text{HKC00}}(x) = \frac{c}{x^2} e^{-c/x}, \quad c = \frac{Rz_u^P |L|^{1-P}}{\kappa^2} \quad (2A.1)$$

where κ ($=0.4$) is the von Kármán constant, P and R are constants depending on stability, z_u is a length scale depending on z_0 (the roughness length in meters, cf.

Equation 2A.7) and z_m , and L is the Obukhov length defined in Equation 3.1. The crosswind integrated flux footprint at the upwind distance $x > 0$ and at the height z_m is described in KM01 by:

$$f_{KM01}(x) = \frac{1}{\Gamma(\mu)} \frac{\xi^\mu}{x^{1+\mu}} e^{-\xi/x} \quad (2A.2)$$

where $\xi(z_m, z_0, L)$ is the flux length scale, Γ the Gamma function, and $\mu(z_m, L, z_0)$ a constant (power law estimates are performed for these parameters, see KM01, p 211). The crosswind dispersion function depends on the crosswind distance y and is described by:

$$D(x, y) = \frac{1}{\sqrt{2\pi}\sigma_y} e^{-y^2/2\sigma_y^2} \quad (2A.3)$$

in which σ_y is the crosswind width (m), described by Detto et al. (2006) as:

$$\sigma_{yDetto} = \alpha_1 z_0 \frac{\sigma_v}{u_*} \left(\frac{x}{z_0} \right)^{p_1} \quad (2A.4)$$

and by KM01 as:

$$\sigma_{yKM} \approx \frac{\sigma_v x}{U_p} \quad (2A.5)$$

where σ_v is the standard deviation of the crosswind speed in $m s^{-1}$ (depending on wind speed and stability), $\overline{U_p}$ is the effective plume velocity in $m s^{-1}$ (see Equation 18 in KM01), u_* is the friction velocity and α_1 (=0.3) and p_1 (=0.86) are empirical parameters. The 2D footprint $DF(x, y)$ is calculated as:

$$DF(x, y) = D(x, y)F(x) \quad (2A.6)$$

The roughness length z_0 is estimated following Neftel et al. (2008) using:

$$z_0 = \frac{z_m}{e^{\kappa U / (u_* - \psi(z_m/L))}} \quad (2A.7)$$

Where U is the observed wind speed in $m s^{-1}$, and the stability parameter ψ is described in Equation 2A.10.

2A.2 Surface layer scaling

The Obukhov length L is defined by:

$$L = -\frac{\rho c_p T_a u_*^3}{\kappa g H_v} \quad (2A.8)$$

In which ρ is the air density in $kg m^{-3}$, u_* the friction velocity in $m s^{-1}$, κ the von Kàrmàn constant, H_v the virtual sensible heat flux in $W m^{-2}$, c_p the specific

heat capacity at constant pressure in J (kg K)^{-1} and T_a the air temperature in K. Logarithmic wind profiles from MOST are calculated using:

$$U = \frac{u_*}{\kappa} \left(\log \frac{z_m}{z_0} + \psi \left(\frac{z_m}{L} \right) \right) \quad (2A.9)$$

in which ψ is the integrated flux gradient relationship given in Equation 2A.10 (which drops out for neutral conditions). The integrated flux-gradient relationship for momentum for unstable conditions is given by:

$$\psi \left(\frac{z_m}{L} \right) = -2 \log \frac{1 + \zeta}{2} - \log \frac{1 + \zeta^2}{2} + 2 \operatorname{atan} \left(\zeta - \frac{\pi}{2} \right) \quad (2A.10)$$

where ζ is given as:

$$\zeta = \left(1 - \frac{16z_m}{L} \right)^{0.25} \quad (2A.11)$$

For stable conditions, the integrated flux-gradient relationship for momentum can be described by:

$$\psi \left(\frac{z_m}{L} \right) = 5 \frac{z_m}{L} \quad (2A.12)$$

Acknowledgments

This work was financed by the DFG (Deutsche Forschungsgemeinschaft), project GR2687/3-1 and SCHU 2350/2-1; "Links between local scale and catchment scale measurements and modeling of gas exchange processes over land surfaces". We would like to thank Martin Lennefer and Bernhard Pospichal for additional assistance in the field experiment. Additional contributions to the field setup were made possible by the DFG collaborative research center TR32 "Patterns in soil-plant-atmosphere systems". Furthermore we would like to thank Miranda Braam for fruitful discussions, and our anonymous reviewers for their clear and helpful comments.

3

Detection of entrainment influences on surface-layer measurements and extension of Monin-Obukhov similarity theory

We present a method to detect influences of boundary-layer processes on surface-layer measurements, using statistics and spectra of surface-layer variables only. We validated our detection method with boundary-layer measurements. Furthermore, we confirm that Monin–Obukhov similarity functions fit well to temperature-variance data obtained at two different homogeneous surfaces. However, we found that humidity variance measurements deviate from the universal functions above one of the two studied surfaces for days on which entrained air reached the surface layer. These results confirm that Monin–Obukhov similarity theory should be used with care in the analysis of surface-layer data. Finally, we propose the use of an extra term in flux-variance relations that depends on the entrainment ratio for humidity and on the boundary-layer height. If boundary-layer measurements are not available, we show how the entrainment ratio for humidity can be approximated from the skewness of the humidity distribution.

This chapter is published as van de Boer et al. (2014a).

3.1 Introduction

One step towards improving weather and climate models is to provide limits for the use of parametrizations for surface fluxes (Katul et al. 2008), which are usually based on Monin–Obukhov (MO) similarity theory. In MO similarity theory, a mean turbulent quantity is described by a limited number of variables related to height, turbulent kinetic energy production, surface roughness, and surface fluxes (Monin and Obukhov 1954). MO similarity theory assumes a homogeneous surface, stationarity, and that surface-layer turbulence only depends on surface fluxes, which in turn depend on surface characteristics, radiation, and the properties of the air that interact with the surface. Subsequently, fluxes of e.g. momentum, sensible heat (H) and moisture (L_vE) can be determined from mean turbulent quantities such as gradients or variances, in combination with the universal functions derived from MO similarity theory.

However, if the atmospheric surface layer (ASL) is influenced by larger-scale processes such as advection and entrainment, or if the surface is horizontally heterogeneous, the additional sources and sinks for a specific scalar cause an increase in scalar variance. MO similarity theory then gradually loses validity (Moene et al. 2006). Differences between the universal functions for temperature and humidity are also expected in very buoyant conditions, due to their different effect on buoyancy: temperature plays an active role while humidity plays a mostly passive role. Deviations from the universal functions are also expected in the case of non-stationarity (Katul et al. 2008). These deviations might be different for every scalar (e.g., potential temperature θ and specific humidity q), resulting in a specific universal function for every scalar. However, even for ideal conditions universal functions derived from MO similarity theory are expected to be accurate to no more than 10–20 % (Högström 1996).

Katul et al. (2008) review the causes of dissimilarity between the different published universal functions and conclude that surface heterogeneity, entrainment, and non-stationarity of the data are the main causes. In this study, we focus on the impact of entrainment. Mahrt (1991) found that in a dry convective boundary layer (CBL), entrainment of dry air might exceed evaporation at the surface, causing large eddies to transport dry air towards the surface. De Bruin et al. (1993) hypothesize that the observed scalar fluctuations close to the surface are generated by local and non-local (e.g. entrainment) processes. De Bruin et al. (1999) present evidence for this hypothesis. Michels and Jochum (1995), Sempreviva and Højstrup (1998) and Sempreviva and Gryning (2000) pursued research regarding temperature and humidity fluctuations in the CBL.

Lohou et al. (2010) show that during the drying and moistening periods of a monsoon cycle in western Africa, the temperature source and humidity sink at the boundary-layer top are sufficient to allow entrainment to affect the entire CBL down to the surface. They relate this to humidity statistics in particular, and show that MO

similarity theory fails for the parametrization of humidity-related moments. However, a detection method for entrainment using only surface-layer data has not been presented yet to our knowledge. Neither has the addition of variance related to entrainment been quantified.

In this study, we investigate the impact of entrained dry air on surface-layer data, and thereby on the validity of MO similarity theory. Our study focusses on the following four research questions:

- Is MO similarity theory valid for our surface-layer data?
- Do we find indicators for entrainment in the surface-layer data?
- Are these indicators in agreement with entrainment that is implied in boundary-layer data?
- Can we quantify the effects of entrainment on turbulence measurements and thus extend universal functions for entrainment effects, based on surface-layer measurements?

We start with a review on surface-layer and boundary-layer scaling relevant to this study in Section 3.2. We describe our measurements and data selection procedure in Section 3.3.1. In Section 3.3.2 we present our method to detect entrainment influences on surface-layer turbulence measurements using wavelet analysis, statistical analysis, or a so-called ‘local entrainment ratio’. We furthermore describe in Section 3.3.2 how we obtain an extension to MO similarity theory. In Section 3.4 we evaluate the validity of MO variance scaling for our dataset, and determine the moisture entrainment regime in different ways. Finally, we establish the relationship between the entrainment regime and invalidity of the MO scaling. Section 3.5 provides conclusions.

3.2 Theory

In this section we summarize surface-layer and boundary-layer scaling relevant to our analysis. Furthermore, we outline characteristics of boundary-layer turbulence that can be exploited for the detection of entrainment effects in surface-layer observations. We also discuss typical time scales of surface-layer and boundary-layer processes, and we introduce the wavelet analysis, which will be used later for the separation of fluctuations at small and larger time scales. Finally we show how to relate the shape of the vertical profile of humidity in the CBL to surface-layer measurements.

3.2.1 Surface-Layer and Boundary-Layer Scaling

Monin–Obukhov Surface-Layer Scaling

In this study, we focus on flux-variance relations rather than flux-gradient relationships because the former are commonly used in the analysis of surface-layer measurements. In MO similarity theory, scalars have identical flux-variance relations, in which scalar variance depends on the scaled scalar flux and on the atmospheric stability via the Obukhov length L Obukhov (1946), where

$$\frac{z}{L} = -\frac{H_v}{\rho c_p} \frac{\kappa g z}{\overline{\theta}_v u_*^3}, \quad (3.1)$$

with height z , virtual sensible heat flux H_v , air density ρ , specific heat of air c_p (for dry air $c_p = 1004 \text{ J kg}^{-1} \text{ K}^{-1}$), von Kàrmàn constant κ (0.4), acceleration due to gravity g (9.81 m s^{-2}), mean virtual potential temperature $\overline{\theta}_v$ and surface friction velocity u_* .

Flux-variance relations derived from MO similarity theory were established by, inter alia, De Bruin et al. (1993), who fitted their variance data to a similarity equation for local free-convective conditions (very unstable, indicated with subscript u), and to a function that is valid for near-neutral conditions (indicated with subscript n). In squared form, to describe variances rather than standard deviations, we obtain

$$\frac{\sigma_x^2}{x_*^2} = f_{s_n} \left(\frac{z}{L} \right) = 8.4(1 - 28.4(z/L))^{-2/3} \quad (3.2)$$

for unstable and near-neutral conditions, and

$$\frac{\sigma_x^2}{x_*^2} = f_{s_u} \left(\frac{z}{L} \right) = 0.9(-z/L)^{-2/3} \quad (3.3)$$

for very unstable conditions, where s stands for surface, and x_* is the turbulent scale $-F_{x_s}/u_*$ of scalar x (we use F for flux). Historically, flux-variance relationships were primarily derived for θ . However, the temperature variance in the ASL (which is relatively humid and warm) is affected less and in a different way by entrainment (of dry and warm air) than is humidity variance.

Boundary-Layer Scaling

Entrainment processes produce a transport of relatively warm and dry air from the free atmosphere into the CBL, and occasionally down into the ASL (Mahrt 1991; De Bruin et al. 1999). The entrainment flux of a scalar is its flux density due to turbulent mixing between the top of the boundary layer and the free troposphere above. Its definition and particularly its sign with respect to the vertical direction follows the same convention as that of the surface flux. The combination of a turbulent flux and

a concentration gradient implies the production of scalar variance. Therefore, scalar variance in the CBL is related to the surface flux of that scalar (F_{x_s}), and to the scalar entrainment flux (F_{x_e}). The ratio of these fluxes (Deardorff 1980), referred to as the entrainment ratio, can be written as

$$\beta_x = \frac{F_{x_e}}{F_{x_s}}. \quad (3.4)$$

We note that the production of variance by the entrainment flux can be an order of magnitude larger than the production of variance by the surface flux (Moene et al. 2006).

The entrainment ratio for buoyancy generally ranges from -0.4 to -0.1 (Hägeli et al. 2000), and may increase significantly with shear-induced turbulence (Pino et al. 2003), or just after sunrise (Braam et al. 2012). Furthermore, entrainment at the top of the CBL may vary in response to changes in surface forcing (Angevine 2008) and to the lapse rate in the free atmosphere above the CBL (Sorbjan 1996). However, a constant value of -0.2 is often used in atmospheric numerical models.

The entrainment ratio for humidity can vary widely in magnitude. If the entrainment ratio for humidity is <1 , humidity in the CBL increases and humidity transport is dominated by the surface flux. On the other hand, if $\beta_q >1$, the CBL is drying: the entrainment process drives the humidity transport (Moene et al. 2006).

To describe the effects of entrainment on scalar variances, we need expressions for scalar variances. We describe two expressions for the total scaled variance; the first is based on scaling functions derived from a large-eddy simulation (LES) study of Patton et al. (2003) that was instigated by Moeng and Wyngaard (1989), and the second is derived from a parametrized variance budget equation with scaling functions from Moeng and Wyngaard (1989).

Moeng and Wyngaard (1989) presented a decomposition of scalar variances into variance related to top-down processes (related to entrainment fluxes), bottom-up processes (related to surface fluxes), and to the correlation of these two types of processes (Equation 4.12 in their paper). In their scaling theory, which is derived from LES, the total variance depends on height relative to boundary-layer height (z/z_i), the surface and entrainment scalar fluxes, and the free-convection velocity scale w_* defined as

$$w_* = \left(\frac{gz_i H_v}{\theta_v \rho c_p} \right)^{1/3}. \quad (3.5)$$

We replace the entrainment flux in this decomposition by $\beta_x F_{x_s}$, after Equation 3.4. Furthermore, the variance is non-dimensionalized with $X_* = -F_{x_s}/w_*$ (Moene et al. 2006), which results in an expression for the total scaled variance,

$$\frac{\sigma_x^2}{X_*^2} = \beta_x^2 f_e \left(\frac{z}{z_i} \right) + f_s \left(\frac{z}{z_i} \right) + \beta_x f_{es} \left(\frac{z}{z_i} \right) \quad (3.6)$$

where f_e , f_s and f_{es} are boundary-layer similarity functions.

The top-down (called entrainment, 'e' in this study) and bottom-up functions of Moeng and Wyngaard (1989) are evaluated in Patton et al. (2003) with a LES model of a finer resolution for the ASL (5 m) than Moeng and Wyngaard (1989). Patton et al. (2003) simulated the atmospheric boundary-layer flow for a case with and without a forest canopy. We use their results of the non-canopy case to create a similarity function, specific for the ASL instead of for the whole CBL. The surface-related term is described as

$$f_s \left(\frac{z}{z_i} \right) = 1.8 \left(\frac{z}{z_i} \right)^{-2/3} \quad (3.7)$$

for $z < 0.1z_i$, and the entrainment term within the ASL is described as

$$f_e \left(\frac{z}{z_i} \right) = 0.87 \left(1 - \frac{z}{z_i} \right)^{-0.43} \quad (3.8)$$

for $z < 0.1z_i$. The entrainment term in the ASL is not very sensitive to z/z_i . From the LES data of Patton et al. (2003) we find a value of 0.7 for f_{es} for $z < 0.1z_i$.

The surface-layer based estimate for σ_x^2 (Equation 3.3) should match the boundary-layer based estimate (Equation 3.7) for very unstable conditions. Indeed, $f_{su}(z/L)$ and $f_s(z/z_i)$ can be rewritten using Equation 3.1 to expand L and Equation 3.5 to expand w_* to obtain

$$x_*^2 f_{su} \left(\frac{z}{L} \right) \approx X_*^2 f_s \left(\frac{z}{z_i} \right). \quad (3.9)$$

This result can be used in Equation 3.6. For comparisons with surface-layer scaled functions, Equation 3.6 should be converted to a variance function normalized with x_* , which means a multiplication with X_*^2/x_*^2 , or thus with u_*^2/w_*^2 . Therefore, we derived from Equation 3.1 and Equation 3.5,

$$\frac{u_*}{w_*} = \left(-\frac{z_i}{L} \right)^{-1/3} \kappa^{1/3}. \quad (3.10)$$

The surface-layer scaled variance function, which partly depends on MO universal functions, can then be rewritten as

$$\frac{\sigma_x^2}{x_*^2} = f_s \left(\frac{z}{L} \right) + \beta_x^2 \left(f_e \left(\frac{z}{z_i} \right) + \frac{f_{es} \left(\frac{z}{z_i} \right)}{\beta_x} \right) \left(-\frac{z_i}{L} \right)^{-2/3} \kappa^{2/3}. \quad (3.11)$$

An alternative way of determining the impact of entrainment processes on scalar variances in the ASL is through the variance budget of specific humidity (q). We here derive the entrainment-related variance from the parametrized budget equa-

tion after Equation B3 in Moene et al. (2006), viz.

$$\frac{\sigma_{q_e}^2}{q_*^2} \approx \frac{\tau_D}{q_*^2} \left(-2 \overline{w'q'_e} \frac{\partial \overline{q_e}}{\partial z} - \frac{\partial \overline{w'q_e'^2}}{\partial z} \right), \quad (3.12)$$

which is only a fair approximation of the total variance near the surface and the top of the CBL for a horizontally homogeneous flow in a steady state. In Equation 3.12, τ_D is a dissipation time scale, which can be derived from Figure 22 in Moeng and Wyngaard (1989) for the ASL ($\leq 0.1z_i$) as

$$\tau_D \approx \frac{z_i}{w_*}. \quad (3.13)$$

The total scaled variance in the ASL due to local production (surface related) and production in the upper part of the CBL (entrainment related) can then be written as

$$\frac{\sigma_q^2}{q_*^2} \approx f_s \left(\frac{z}{L} \right) + \frac{\tau_D}{q_*^2} \left(-2 \overline{w'q'_e} \frac{\partial \overline{q_e}}{\partial z} - \frac{\partial \overline{w'q_e'^2}}{\partial z} \right). \quad (3.14)$$

We rewrite the boundary-layer production terms using two derivations from Figures 11 and 14b respectively in Moeng and Wyngaard (1989). From their Equation 4.11a it follows that $\frac{\partial \overline{q_e}}{\partial z}$ depends on the top-down gradient function g_t shown in their Figure 11, which is approximately 1 in the ASL, at $1 - z/z_i = 0.9$. Thus,

$$\frac{\partial \overline{q_e}}{\partial z} \approx - \frac{\overline{w'q'_e}}{w_* z_i}. \quad (3.15)$$

In Figure 14b (Moeng and Wyngaard 1989), the top-down turbulent transport $\overline{w'q_e'^2}$ decreases with height by $\approx \frac{4}{z_i} \frac{\overline{w'q_e'^2}}{w_*}$ in the ASL, viz.

$$\frac{\partial \overline{w'q_e'^2}}{\partial z} \approx -4 \frac{\overline{w'q_e'^2}}{w_* z_i}. \quad (3.16)$$

By substituting Equations 3.10, 3.13, 3.15, and 3.16 into Equation 3.12, and replacing $\overline{w'q'_e}$ by $\beta_q \overline{w'q'_s}$ (Equation 3.4), we obtain a quantification of the contribution of the entrainment processes to the total variance that depends on the entrainment ratio for humidity

$$\frac{\sigma_{q_e}^2}{q_*^2} \approx (2 + 4) \beta_q^2 \left(-\frac{z_i}{L} \right)^{-2/3} \kappa^{2/3}. \quad (3.17)$$

In this expression, the term for the transport of scalar variance (e.g. of humidity) is twice as large as the production term caused by the vertical scalar gradient in the

entrainment zone. The total variance can be written as

$$\frac{\sigma_q^2}{q_*^2} = f\left(\frac{z}{L}, \frac{z}{z_i}, \beta_q\right) \approx f_s\left(\frac{z}{L}\right) + 6\beta_q^2 \left(-\frac{z}{L}\right)^{-2/3} \left(\frac{z}{z_i}\right)^{2/3} \kappa^{2/3}. \quad (3.18)$$

Both Equations 3.11 and 3.18 require β_q and z_i as boundary-layer input for these variance quantifications. Also, both equations are normalized with the same scale, such that they can be compared to each other.

3.2.2 Entrainment Signals in Surface-Layer Observations

Spectral Analysis

Turbulence measurements contain information on time scales (fixed measurements) or length scales (moving airborne measurements), which can be compared to each other using Taylor's frozen turbulence hypothesis. We here associate boundary-layer processes such as entrainment with relatively large time scales (low frequencies) ≈ 20 min, which is $\sim z_i/w_*$. This value of 20 min also corresponds to results presented in Figure 3.3 in Canut et al. (2010). In their study, the horizontal distance between the entrained 'dry tongues' is approximately 4 km at a mean wind speed of 3.2 m s^{-1} . Surface-layer turbulence is associated with relatively short time scales (high frequencies) ≈ 1 min, see Figure 3.4 in Kaimal et al. (1972). However, a clear distinction can not be made between these two sources of variance in the scalar signal, because scalar fluctuations can also arise from the 'chewing-up' of large-scale turbulence by smaller-scale turbulence (Kimmel et al. 2002).

To extract dominant frequencies from time series, we can use the wavelet analysis and, as with Fourier analysis, it can be used to detect the distribution of variance over different frequencies. However, the Fourier transform assumes the data are cyclic, whereas the wavelet transform can be used for waves with only a few periods and a finite lifetime. The application of wavelet analysis to atmospheric turbulence started already in the last century by e.g. Hudgins et al. (1993) and Farge et al. (1996). Fourier analysis cannot cope with non-linear convection, which is characteristic of a CBL. Therefore, Terradellas et al. (2001), Cuxart et al. (2002), Mauder et al. (2007) and others proceeded with wavelet analyses in atmospheric turbulence studies.

For wavelet analysis, we need a so-called mother function. De Moortel et al. (2004) studied the use of non-orthogonal and complex mother wavelets (e.g. Paul and Morlet). They concluded that a smaller value of the wavelet parameter provides a better time resolution, whereas a larger wavelet parameter improves the frequency resolution. We intend to clearly distinguish between different frequency ranges in the turbulence signal and make a compromise between obtaining the exact dominant frequency and the timing of changes in the spectra. To finally determine the fraction of the variance contained in a certain part of the spectrum, we use

an ogive, the integral of the power spectrum up to a certain frequency (Oncley et al. 1996).

Statistical Analysis

Graf et al. (2010) conclude that turbulence statistics obtained near the surface cannot be solely explained by local effects, but contain information about the whole CBL, including the entrainment zone. These boundary-layer-scale variations in e.g. T , q and u may in turn also enhance or diminish the surface fluxes (Sorbjan 1996). However, here we focus on entrainment effects on scalar variances rather than on entrainment-flux induced variations of the surface fluxes.

Figure 3.1 sketches vertical profiles of specific humidity for two different entrainment regimes. The solid blue line represents the profile in a well-mixed CBL with relatively weak entrainment, whereas the dashed red line shows the humidity profile for relatively strong entrainment and therefore a non-negligible gradient in the CBL. We expect that the distribution of humidity in the ASL for the first case is positively skewed because air that is drier than the constant mixed-layer value cannot reach the surface layer. The humidity distribution of the second case loses its skewness because dry air from the upper part of the CBL, and even drier air entrained from the free atmosphere above, reaches the ASL. Studies of Mahrt (1991), Lenschow et al. (2000), de Arellano (2004), Couvreux et al. (2007), Lothon et al. (2007) and Lohou et al. (2010) confirm this relation between humidity skewness (further referred to as Sk_q) and entrainment processes.

Accordingly, we might expect a relation between Sk_q in the ASL and violation of MO similarity theory (caused by boundary-layer-scale fluctuations in the q signal). However, using humidity distributions, turbulent advection of dry air from another region that is much drier than the study area cannot be distinguished from entrainment processes. That is, the effect of a horizontal humidity gradient on the skewness of q may be similar to that of a vertical gradient.

The relation between skewness and violation of MO similarity theory will not be valid for temperature, because warm entrained air from the free atmosphere cannot be distinguished from warm air from the surface in the distribution of temperature in the ASL. As a result, enhanced entrainment will not significantly affect the skewness in the ASL.

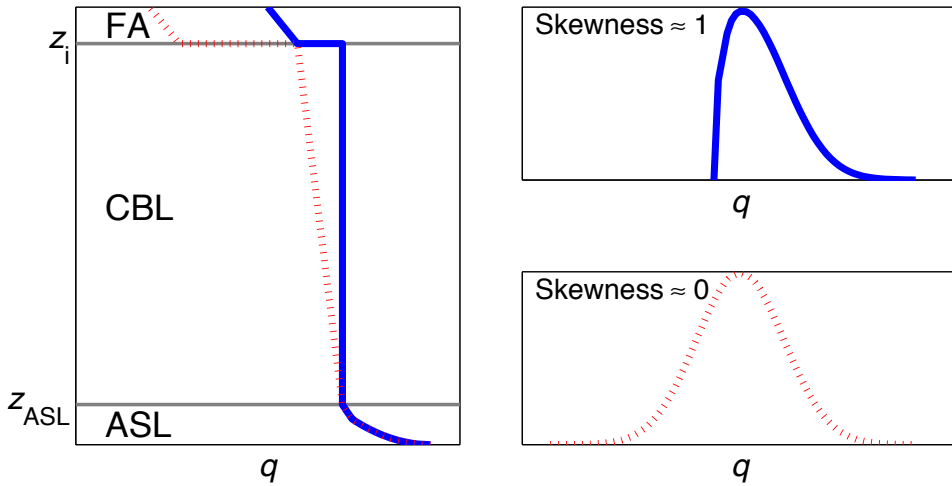


Figure 3.1: Sketch of the vertical profile and distribution of the humidity signal observed in the ASL in the case of relatively weak entrainment (solid blue, high skewness) and in the case of relatively strong entrainment (dashed red, zero skewness)

3.3 Data and Methods

3.3.1 Field Measurements

BLLAST Experimental Set-Up

The field campaign Boundary-Layer Late-Afternoon and Sunset Turbulence (BLLAST) took place near the Pyrenees in south-west France, from 14 June to 8 July 2011 (Lothon et al. 2012). The main objective of this campaign was to better understand the physical processes that control and follow the transition from a CBL towards a stratified nocturnal boundary layer. Surface and boundary-layer measurements were performed around Lannemezan, a village located on a large plateau (200 km²) with several mainly agricultural land-use types.

Two masts were installed at the so-called Edge site (which was actually used to study the effect of an edge between two different land-use types on the validity of MO similarity theory). They were installed (Figure 3.2) in a grass field and in a field mainly cropped with wheat. The latter will further be referred to as ‘fodder’, because it is a mixture for fodder purposes also containing minor portions of oats, barley and peas. The masts were equipped with sensors for the main surface energy components: sensible heat flux (sonic anemometer), moisture flux (sonic anemometer and infra-red gas analyzer) (CSAT3, Campbell Scientific, Logan, Utah, USA and LI-7500, LI-COR, Lincoln, Nebraska, USA), incoming and outgoing shortwave and longwave radiation (CNR1, Kipp and Zonen, Delft, the Netherlands), and soil heat flux (HFP01SC, Hukseflux, Delft, the Netherlands).

The grass was cut before the installation of the masts, and grew throughout the campaign. The fodder reached its final height (0.95 m) around the start of the campaign. The EC sensors in the grass field were placed 2.55 m above the surface, which is 2.25–2.50 m above the grass top, depending on growth. In the fodder field, the EC sensors were installed 3.00 m above the surface, which is 2.05 m above the top of the fodder. Both radiometers were installed 1.68 m above the surface.

A 60-m tower was located at a distance of 500 m from the Edge site, on which EC sensors were installed at different heights. In this study we used sensible heat fluxes (CSAT3, Campbell Scientific), relative humidity measured at 60 m, and precipitation measurements (EM LTD, ARG100). The land-use types closely surrounding the EC stations (Figure 3.2) were determined during the campaign. We used a GPS device to specify corners and borders of the fields. The characterization covered the area at least up to a distance of 300 m around the stations in order to apply a footprint model. The aerial view also shown in Figure 3.2 was used to complement the point dataset. Both were used to create a vector map of land use around the site. A grid (1 m) dataset was derived from this map for the footprint criterion explained in the following section.

During fair weather conditions throughout the campaign, so-called intensive observation periods (IOP), additional observations were performed using radiosoundings and other boundary-layer profiling instruments. Several radiosondes were launched at two agricultural sites located 1 and 4 km away from our EC site. We used Vaisala (Digicora III, RS92 SGP) and MODEM (developed by CNRS) sondes launched at 1100, 1300 and 1400 UTC at both locations, and obtained vertical temperature and humidity profiles from the soundings. These are shown, including the fit of the first-order jump model (explained in Section 3.3.2), in Figures 3A.1 and 3A.2 (see for an overview of all soundings the open database at <http://bllast.sedoo.fr>).

Data Processing and Selection

We determined fluxes and variances from the raw 20-Hz data using ECpack-2.5.23-1.3 (van Dijk et al. 2004). The averaging time was 30 min, which is a typical averaging time for EC data needed to capture surface-layer turbulence and exclude mesoscale processes. We performed a planar fit rotation (Wilczak et al. 2001) over the whole measurement period of 23 days to adjust the coordinate system. Linear trends were removed and the density correction (Webb et al. 1980) was carried out to correct the observed humidity for variations of the air density. The sonic temperature was transformed to actual air temperature using the Schotanus correction (Schotanus et al. 1983). The sensible heat flux is based on the sonic temperature (i.e. not corrected for humidity influences on the temperature), and so is close to the buoyancy flux as needed (Section 3.3.2).

Ninety-five percent confidence intervals were estimated by quantifying the sampling error for each scalar average and flux, following van Dijk et al. (2004). We re-

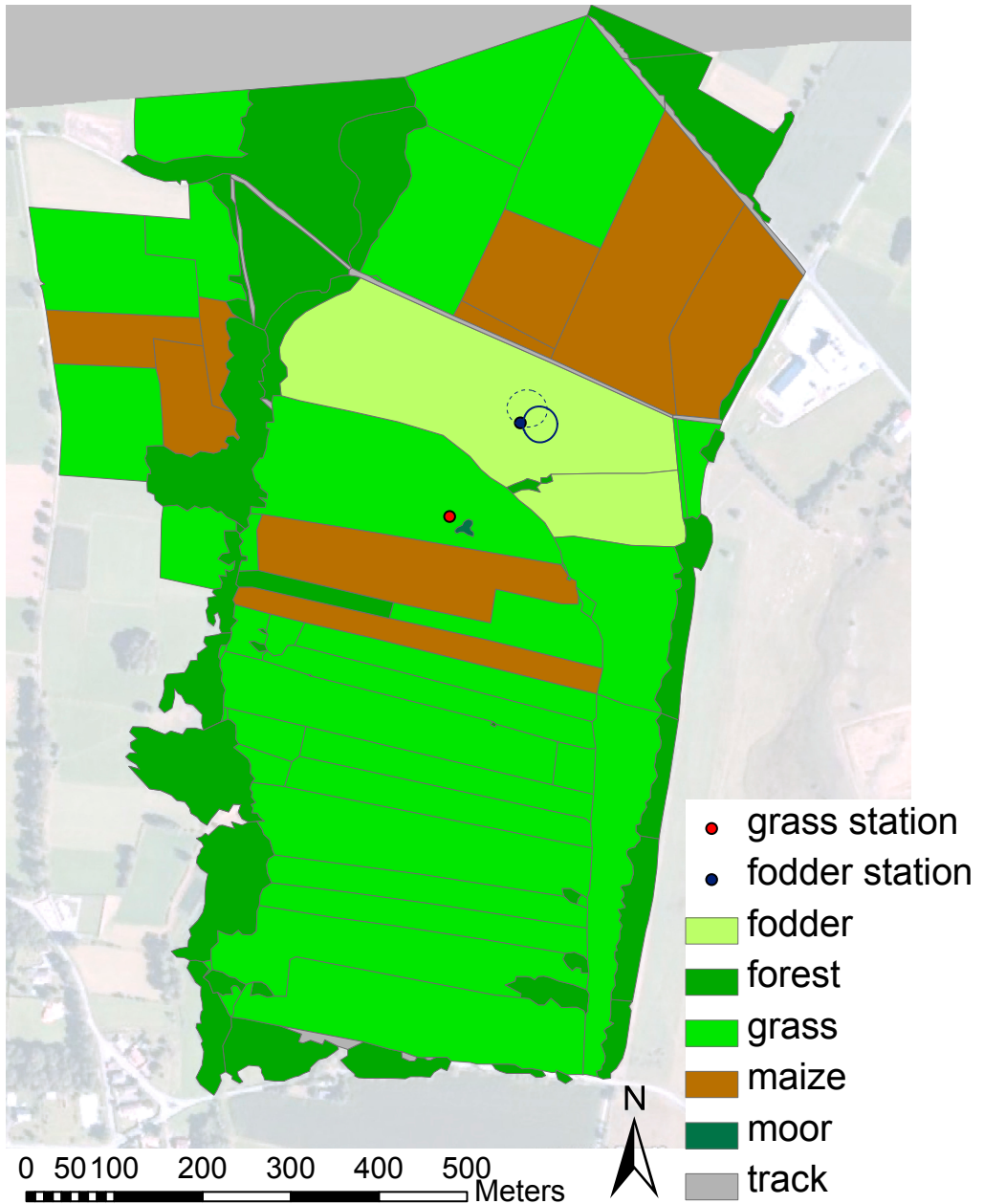


Figure 3.2: Land-use map of the study area (Edge site) with locations of two eddy-covariance (EC) stations in Lannemezan (France), in the summer of 2011. Two example footprints are given that contributed for 75 % (the surface heterogeneity criterion, Section 3.3.1) to the observed fluxes at the EC station in the so-called ‘fodder’ field at day of the year (DOY) 177 (solid) and 182 (dashed) at 1330 UTC (these moments are also used for other figures). Aerial view: GoogleTM Earth, IGN-France. 43°07’N, 0°21’E, 582 m above mean sea level

moved processed data for which the confidence interval of the non-dimensionalized standard deviation (see left-hand side of Equation 3.2) was >0.5 to exclude sam-

pling errors. Furthermore, 30-min periods with a sensible heat flux or latent heat flux $<10 \text{ W m}^{-2}$ were removed in order to only focus on data collected during unstable conditions.

We eliminated data with wind directions between 135° and 145° to avoid mast disturbances, and to exclude any surface-heterogeneity effects at field scale, we only used EC data of which at least 75 % of the footprint is located in the field of measurements (grass or fodder). Based on van de Boer et al. (2013), we used a combination of the footprint model of Hsieh et al. (2000) and the crosswind function of Kormann and Meixner (2001) to estimate the location of the flux footprints. Variance footprints might differ from flux footprints, but to date no variance-footprint model has been created and tested.

For the raw data analyses on statistics and spectra, we discarded the same data as for the 30-min averaged data. In addition, we applied linear detrending per hour of raw data and removed non-physical data. In both the raw and processed data we removed data obtained between 0900 and 1100 UTC at DOY (day of the year) 178 and between 1300 and 1500 UTC at DOY 186 because of non-stationarity caused by the passage of a cold front (which can be recognized in the vertical humidity profiles in Figure 3A.1 in the Appendix). All these restrictions led to a reduction by 8 % of all daytime data (0800-1600 UTC) above the fodder, and a reduction by 20 % of all grass daytime data. The difference in data reduction between both sites is mainly due to the footprint restriction.

3.3.2 Data Analyses

We here describe our wavelet analysis on the surface-layer data that was performed in order to detect events with low-frequency contributions. Based on our schematic in Figure 3.1, we attributed these low-frequency events to entrainment when the natural positive skewness of the humidity distribution (as described below) was reduced. We show how we calculated entrainment ratios for humidity to validate our entrainment detection method. Furthermore we describe how we separated the data of the driest surface (fodder) in a low and a higher entrainment regime (based on surface-layer data), so that we could quantify the effect of entrainment on the surface-layer scaled variances. We finally explain here how we tested MO similarity functions (Section 3.2.1) for all daytime data over two different surfaces, for temperature and humidity.

Quantification of Entrainment Regime Based on Surface-Layer Data: Spectra and Central Moments

To obtain information about the time scale of variations we have used spectral analysis based on wavelet transforms. We used spectral analysis in two ways:

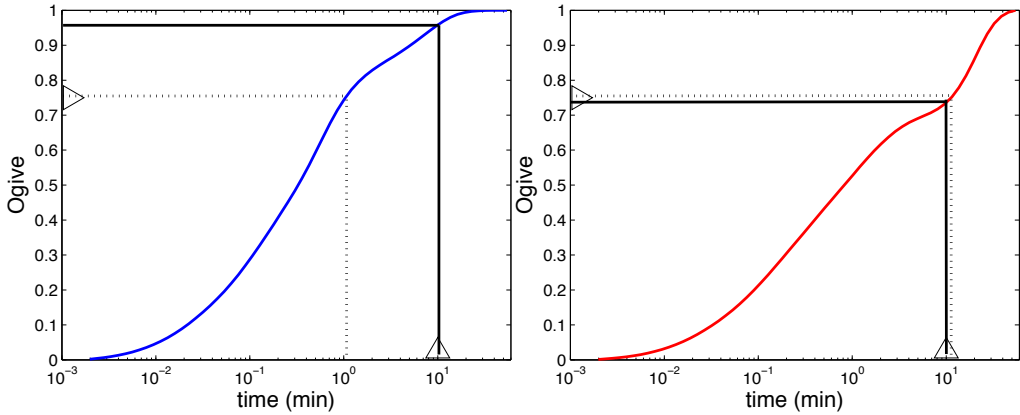


Figure 3.3: *Ogives of humidity data without a predominance of large-scale variance (left, blue, DOY 182), and with a predominance of large-scale variance (right, red, DOY 177) at 1300–1400 UTC, measured over fodder. The solid black lines indicate the 10-min time-scale threshold, and the dashed lines indicate the time scale at which 75 % of the variance is covered*

- To separate (non-periodic) events with time scales >10 min from events with time scales <10 min.
- To find the time scale per time interval at which 75 % of all variance is reached.

We used the Paul wavelet as the mother function to capture non-periodic scales, and we used the fourth-order function to have as much information about the exact frequencies as possible. Using the wavelet spectrum, we separated the total variance into a part related to time scales <10 min and a part related to larger time scales (see Figure 3.3). We define the relative contribution of larger time scales as $\sigma_{>10\text{min}}^2 / \sigma_{\text{tot}}^2$. It will be justified later in this study (Figure 3.6) that, in the ASL, there is a small energy gap at a time scale of 10 min. The separation of variance by a 10-min time scale was done for all IOP days and based on detrended time series of 1 h of 20-Hz data. Furthermore, ogives based on the wavelet spectra were used to determine a specific time scale. In Figure 3.3 we show two examples of ogives; one case with and one without a predominance of large time scales. The time scale at which 75 % (that is, a significant part) of the humidity variance was reached is our definition of the time scale TS (see dashed lines in Figure 3.3). As shown in Figure 3.3, TS is approximately 1 min if large time scales are not predominant, whereas TS can be 10 min in the case of predominant large time scales in the surface-layer data. The latter agrees with our assumption that boundary-layer processes have a time scale >10 min (Section 3.2.2).

We do not expect large differences in the daily course of daytime surface-layer related time scales, because the increase of larger scales in the CBL during the day goes along with an increase in smaller scales (surface-related turbulence), such that the relative role of large scales on the total variance in the ASL does not change much (except during the morning and afternoon transition). If larger-scale processes

are dominant, we expect them to be dominant for most of the daytime data of that day. Therefore, we determine TS each day. We calculated the median and standard deviation of hourly dominant time scales between 0800 and 1600 UTC to obtain a daily value based on more daytime data without a predominance of both transition periods.

In Section 3.2.2 it was identified that in situations with strong entrainment, the scalar skewness in the surface layer is expected to decrease. Therefore, for the same 20-Hz data as were selected for the time scale study, we calculated Sk_q . We also calculated medians and the standard deviation per day of hourly skewnesses between 0800 and 1600 UTC.

Quantification of Entrainment Regime Based on Boundary-Layer Data: Local Entrainment Ratio

Because the value of the entrainment ratio for the buoyancy fluxes is rather confined, we expect a larger variability in the effect of entrainment on surface-layer data for humidity than for temperature. Therefore, we determined the entrainment regime in terms of the entrainment ratio for humidity. We used radiosonde data to determine the entrainment ratio for humidity.

We first calculated the entrainment buoyancy flux H_{v_e} from the surface buoyancy flux (Equation 3.4), using a fixed value of -0.2 for the entrainment ratio for the buoyancy flux. We calculated H_{v_e} by using a daytime-averaged surface buoyancy flux H_{v_s} (1000-1500 UTC, in agreement with sounding launching times) obtained at 60 m (see Section 3.3.1), representing the area averaged flux of our study area per day.

Then we applied an adapted Bowen ratio (based on the buoyancy flux rather than on the sensible heat flux) at the boundary-layer top (Betts 1992) to calculate $L_v E_e$,

$$B_e = \frac{H_{v_e}}{L_v E_e} = \frac{c_p \Delta \theta_v}{L_v \Delta q}, \quad (3.19)$$

in which $\Delta \theta_v$ and Δq are the jumps in virtual potential temperature and specific humidity at the height of the temperature inversion at the top of the boundary layer, and L_v is the latent heat of vaporization of water ($\approx 2.5 \times 10^6 \text{ J kg}^{-1}$). The location and the size of the jumps that are needed in Equation 3.19 were derived from the vertical profiles of potential temperature and specific humidity (see Appendix, Figures 3A.1 and 3A.2 for these vertical profiles). We manually fitted a first-order jump model to the temperature and humidity profiles of every radiosounding dataset to estimate the scalar difference between the borders of the entrainment zone. We note that the first-order jump model assumes that the entrainment zone has a finite thickness (Mahrt and Park 1976). However, we see in Figures 3A.1 and 3A.2 that the quantification of the jumps is not straightforward, such that values of the derived $L_v E_e$ are uncertain.

Table 3.1: Entrainment fluxes ($H_{v_e}, L_v E_e$) and entrainment ratio for humidity over the fodder field (β_q), calculated from surface fluxes ($H_{v-area}, L_v E_{fodder}$) and the temperature and humidity jumps ($\Delta\theta_v$ and Δq) in the vertical profiles in Figure 3A.1 (1 km from the EC stations)

DOY	Time UTC	z_i m a.g.l.	$\Delta\theta_v$ K	Δq gkg ⁻¹	H_{v-area} Wm ⁻²	H_{v_e} Wm ⁻²	$L_v E_e$ Wm ⁻²	$L_v E_{fodder}$ Wm ⁻²	β_q -
170	1104	983	4.5	-5.0	210	-42	115	267	0.43
171	1101	713	1.3	-2.6	123	-25	119	266	0.45
175	1052	1110	3.1	-2.0	160	-32	50	202	0.25
176	1034	531	1.8	-4.7	189	-38	250	221	1.13
177	1052	349	0.4	-2.2	143	-29	396	208	1.90
177	1347	1052	0.2	-2.0	143	-29	620	208	2.98
178	1050	481	1.0	-3.7	105	-21	189	289	0.65
178	1345	1062	0.8	-4.6	105	-21	282	289	0.98
181	1053	1363	5.9	-5.3	97	-19	44	146	0.30
182	1050	1368	2.7	-1.1	130	-26	26	199	0.13
186	1047	480	-0.2	-4.9	119	-24	-1567	210	-7.5
186	1248	797	2.0	-4.6	119	-24	138	210	0.66

In order to quantify the effect of entrainment on data above a specific field, we define a *local* entrainment ratio

$$\beta_x = \frac{F_{x_e}}{F_{x_{s_{loc}}}}, \quad (3.20)$$

which will be larger in a field with a lower surface latent heat flux. We derived the local entrainment ratio for humidity β_q from the calculated $L_v E_e$ and the measured $L_v E_s$. We took $L_v E_s$ from the 30-min averaged fluxes (again averaged from 1000 to 1500 UTC) of the location of interest (grass or fodder in our case). We calculated entrainment ratios from daytime radiosoundings that were launched between 1100 and 1400 UTC on IOP days (see Tables 3.1 and 3.2 for details per sounding).

We compared all local entrainment ratios for humidity observed above the grass and the fodder with Sk_q and $\sigma_{>10min}^2 / \sigma_{tot}^2$ observed at the time of the radiosounding observations from both launch locations. We excluded the soundings of DOY 178 at 1050 UTC, and DOY 186 at 1258 and 1358 UTC because of non-stationarity caused by the passage of a cold front. We derived relationships between β_q and these surface-layer characteristics Sk_q and $\sigma_{>10min}^2 / \sigma_{tot}^2$. We hereby distinguish between days with both a very low Sk_q and a high TS , from cloudy days (on which we do not expect significant entrainment at the inversion top) with higher values for Sk_q , lower values for TS , or both. We selected a few days of our experiment as ‘entrainment day’, based on a low Sk_q (<0.2 and high TS (>25 min), in combination with a high entrainment ratio (>0.5).

Evaluation of Combined Surface-Layer and Boundary-Layer Scaling

To determine deviations from MO similarity theory, we evaluated non-dimensionalized temperature and humidity variances obtained over the grass and the fodder against the similarity relation Equation 3.2. We distinguish days with a

3.3. DATA AND METHODS

Table 3.2: Entrainment fluxes ($H_{v_e}, L_v E_e$) and entrainment ratio for humidity over the fodder field (β_q), calculated from surface fluxes ($H_{v-area}, L_v E_{fodder}$) and the temperature and humidity jumps ($\Delta\theta_v$ and Δq) in the vertical profiles in Figure 3A.2 (4 km from the EC stations)

DOY	Time UTC	z_i m a.g.l.	$\Delta\theta_v$ K	Δq gkg ⁻¹	H_{v-area} Wm ⁻²	H_{v_e} Wm ⁻²	$L_v E_e$ Wm ⁻²	$L_v E_{fodder}$ Wm ⁻²	β_q -
166	1410	961	2.3	-4.3	97	-19	89	204	0.44
170	1300	921	1.9	-2.7	210	-42	146	267	0.55
170	1358	889	0.5	-1.3	210	-42	289	267	1.08
171	1256	802	2.2	-2.7	123	-25	75	266	0.28
171	1402	894	2.8	-2.6	123	-25	56	266	0.21
176	1257	589	1.6	-2.0	189	-38	114	221	0.52
176	1401	642	1.8	-2.9	189	-38	153	221	0.69
177	1225	701	0.2	-3.1	143	-29	972	208	4.67
177	1408	876	0.3	-2.2	143	-29	534	208	2.57
178	1357	1416	0.7	-6.0	105	-21	455	289	1.57
182	1257	1312	4.0	-0.7	130	-26	-11	199	-0.06
182	1355	1276	3.5	-3.5	130	-26	65	199	0.33
183	1257	891	2.1	-0.7	145	-29	24	208	0.12
186	1258	878	0.7	-3.3	119	-24	279	210	1.33
186	1358	935	0.5	-1.2	119	-24	148	210	0.70

low Sk_q and a high $\sigma_{>10min}^2 / \sigma_{tot}^2$ from days without these indications for dominant entrainment processes.

We fitted the data to the function $c_1(1 - 28.4z/L)^{-2/3}$ using orthogonal distance regression (without weighting of the residuals), where both variables ($-z/L$ and the scaled variance) were log-transformed before fitting. We calculated the first coefficient, c_1 , for the two specific fields, for temperature and for humidity, and for days with and without indications of dominant entrainment processes. We applied a fixed value of 28.4 (De Bruin et al. 1993) for the second coefficient, c_2 , because the data do not cover near-neutral conditions such that the transition between neutral and free convection (i.e. $-z/L \approx c_2^{-1}$) could not be determined accurately.

To investigate whether the differences between observed relationships and the function given in Equation 3.2 are in agreement with boundary-layer scaling theory, we added the variance produced by entrainment processes expected from a certain β_q and z_i to the expected surface-layer flux-variance. The entrainment-related variance was estimated for different entrainment regimes, using the two approximations presented in Section 3.2.1 by Equations 3.11 and 3.18. We calculated the normalized humidity variances for the whole observed stability range, at 2.1 m.

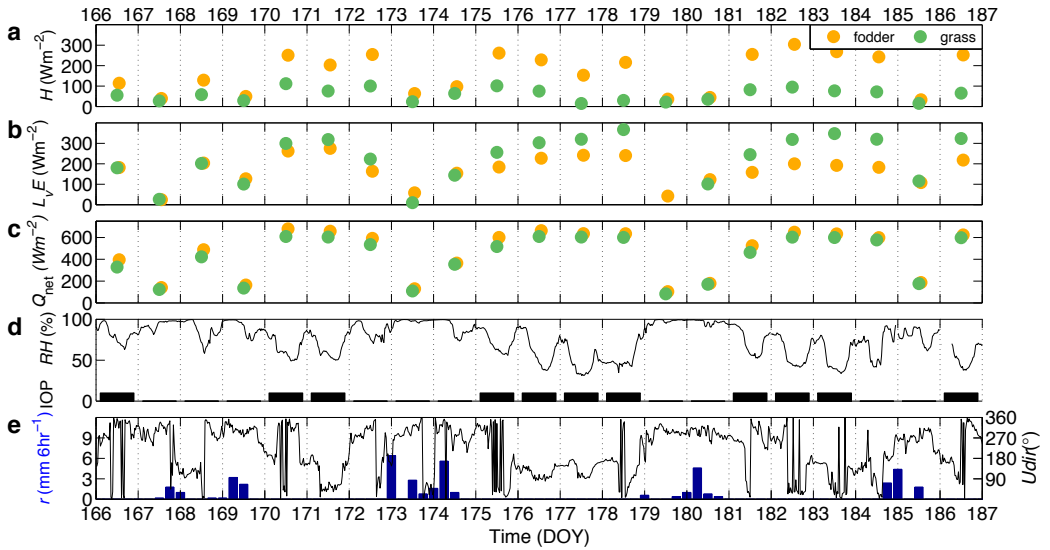


Figure 3.4: DOY numbers indicate the start of the day, for, **a** sensible heat flux (H), **b** latent heat flux (L_vE), **c** net radiation (Q_{net}) all averaged for 0900–1500 UTC and obtained from EC stations over the grass (green) and fodder (yellow) (see Figure 3.2), **d** relative humidity (RH), measured at the 60-m tower (Section 3.3.1); IOP days are indicated by a black bar. **e** wind direction (U_{dir}) measured at the EC station in the fodder; precipitation (r) measured at the 60-m tower

3.4 Results and Discussion

3.4.1 Meteorological Conditions

During the days that were selected as the IOP days, the Azores anticyclone extended to the Pyrenees and produced fair weather. On most other days, the influence of the high pressure system weakened, leading to a number of rain events. Throughout the campaign, midday sensible heat fluxes obtained over the grass varied less between the days than did the sensible heat fluxes over the fodder site. Latent heat fluxes obtained over the grass were significantly larger than were sensible heat fluxes (see Figure 3.4a, b), resulting in a Bowen ratio of ≈ 0.3 over the grass at around 1200 UTC. Over the drier fodder the Bowen ratio was higher, ≈ 0.5 during the first days of the campaign. Due to the ripening of the wheat within the fodder, the Bowen ratio over the fodder increased to values >1 . Due to an almost twice as large albedo of the grass compared to the fodder, the available energy was higher above the fodder than over the grass, for all days (see Figure 3.4c), although longwave outward radiation was slightly higher above the fodder.

A period with warm and dry boundary-layer conditions is recognized for DOY 176 through 178 and for DOY 182 through 183 (Figure 3.4d). In these periods, the relative humidity in the CBL is so low that the high available energy is used for evapotranspiration rather than for the sensible heat flux.

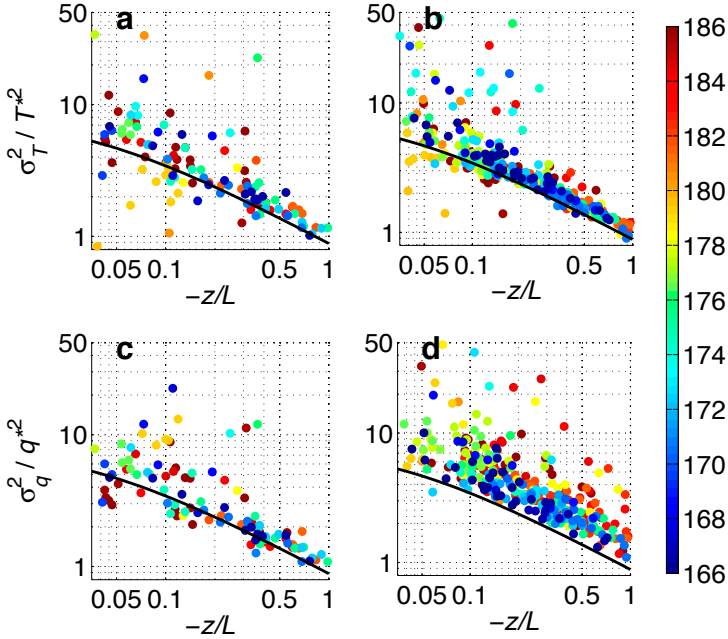


Figure 3.5: Normalized variances of temperature (top) and humidity (bottom) over the grass (left) and the fodder (right) depending on atmospheric stability (z/L) and on the DOY (colour bar) for 30-min intervals. The MO similarity function proposed by De Bruin et al. (1993) (Equation 3.2) is displayed as a solid black line

3.4.2 MO Similarity Theory for Different Surfaces and Scalars

In Figure 3.5, we show the agreement of the variances of temperature and humidity measured over the grass and the fodder with the similarity function of De Bruin et al. (1993) (Equation 3.2). For temperature over both the grass and fodder, observed variances are close to this similarity function with a fit for the first coefficient in Equation 3.2 of 9.9 ± 0.7 and 9.7 ± 0.3 respectively. This indicates that the similarity function (which has a value of 8.4 for the first coefficient) slightly underestimates the temperature variance for both fields.

For humidity over the fodder, variances were clearly higher than the similarity function predicted. The first coefficient in Equation 3.2 is identical to the values for temperature (9.6 ± 0.8) over the grass, whereas it has a clearly higher value of 14.7 ± 0.6 over the fodder. The colours in Figure 3.5 represent the day of the year. We see that the observed non-dimensionalized variances exceeded the values predicted by the similarity relationship especially later on in the campaign. This may be a consequence of ripening of the wheat, leading to a smaller latent heat flux, which makes the non-dimensionalized humidity variance more susceptible to disturbances. Furthermore, discrepancies in temperature variance mostly occur in the weakly unstable regime, since that is when the surface sensible heat flux is small and enhances the relative importance of larger scales.

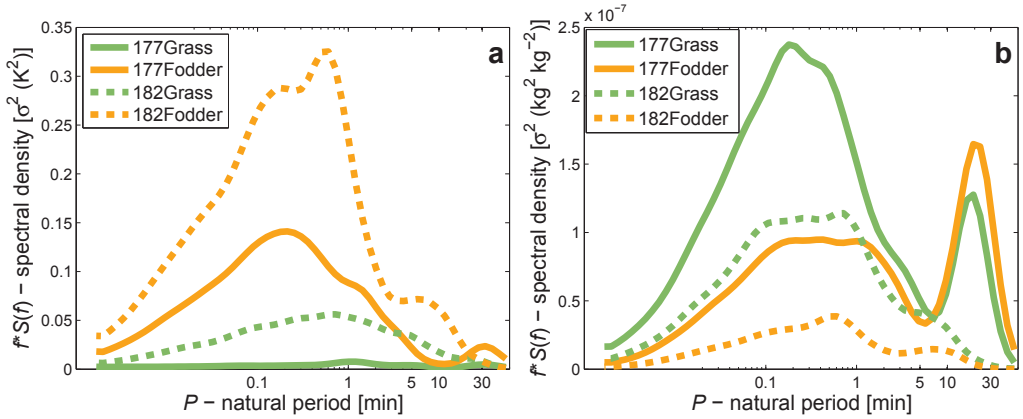


Figure 3.6: Unscaled wavelet spectra of **a** temperature and **b** humidity. The data were obtained over grass (green) and fodder (yellow) at 1300–1400 UTC. Solid lines refer to data from DOY 177, a day with significant large-scale fluctuations in humidity. Dashed lines refer to 1 h of data from DOY 182, a day without significant large-scale fluctuations

Note that less data remain for the grass field than remain for the fodder field, due to the homogeneity criterion (the footprint of the grass measurements exceeded field boundaries more often). However, we do not know to what extent the grass field and fodder field are internally homogeneous. Small-scale surface heterogeneity may give rise to additional variance production, see Section 3.4.5 and Moene and Schüttemeyer (2008).

3.4.3 Indications of Entrainment in ASL Observations

Spectral Analysis

In Figure 3.6 we show wavelet spectra of the temperature and humidity signals for two specific days on both fields; these days differ in the presence of large-scale variance in the humidity signal. In the spectra of vertical velocity (w), all fluctuations affecting w are of a time scale <10 min (not shown here). Thus the surface-flux related variance is expected to occur at time scales <10 min as well. In the data selected for Figure 3.6a, all temperature variance is produced by processes at a time scale ≤ 15 min on both days. However, for humidity we find a difference between the 2 days per field; large-scale processes contribute a lot to the humidity variance at DOY 177 (second peak in Figure 3.6b), while we do not find this direct contribution of large-scale processes at DOY 182 (also in Figure 3.6b). The *relative* contribution of large-scale motions to the total humidity variance at DOY 177 is much larger over the fodder, where fluctuations generated by the surface moisture flux are relatively low (first peak in Figure 3.6b). We noticed (not shown) that the power (amount of variance) for all frequencies in the inertial subrange of the humidity spectra over both fodder and grass is higher at DOY 177 than at DOY 182. This indicates that the large-scale processes on DOY 177 also increase the variance associated with smaller

3.4. RESULTS AND DISCUSSION

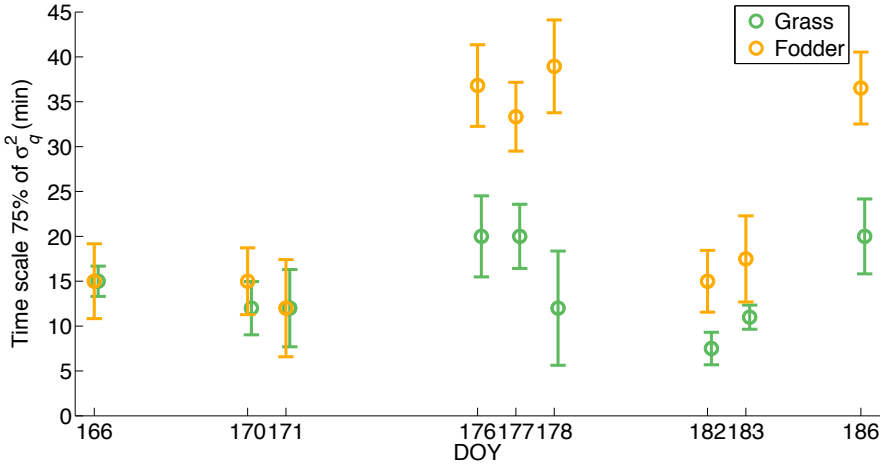


Figure 3.7: The daily median and standard deviation of time scales at which 75 % of the humidity variance was reached above grass (green) and fodder (yellow) per hour between 0800 and 1600 UTC on IOP days

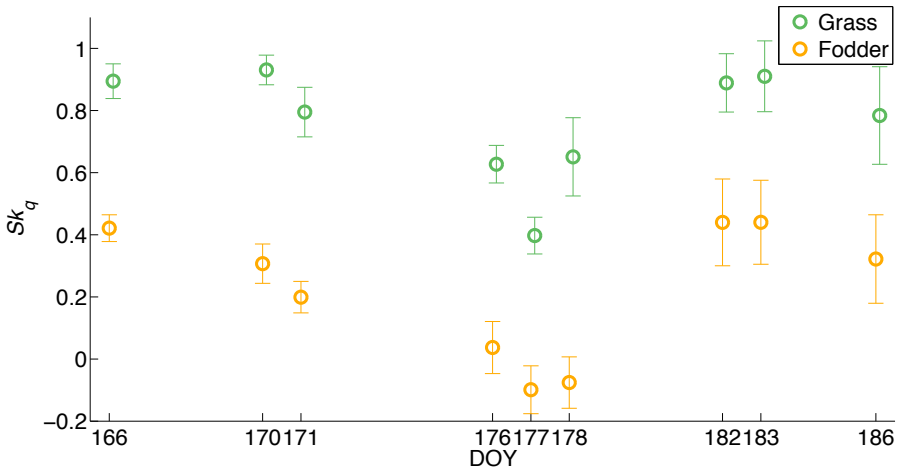


Figure 3.8: The daily median and standard deviation of Sk_q of 1 h of data above grass (green) and fodder (yellow) between 0800 and 1600 UTC at IOP days

time scales, mentioned as the ‘chewing-up’ in Section 3.2.2, Kimmel et al. (2002).

The time scale TS for humidity is approximately 10–15 min for most of the days above both fields (see Figure 3.7), but it reaches 35 min over the fodder for DOY 176–178 and DOY 186. This indicates that, on those days, processes at a spatial scale larger than the depth of the ASL affected surface-layer measurements. To ensure that the observed differences in TS were not due to a specific selection of the data, we examined different time intervals (0700–1700 UTC, 0800–1600 UTC, 0900–1500 UTC, and 1000–1400 UTC). However, the difference for the fodder TS between

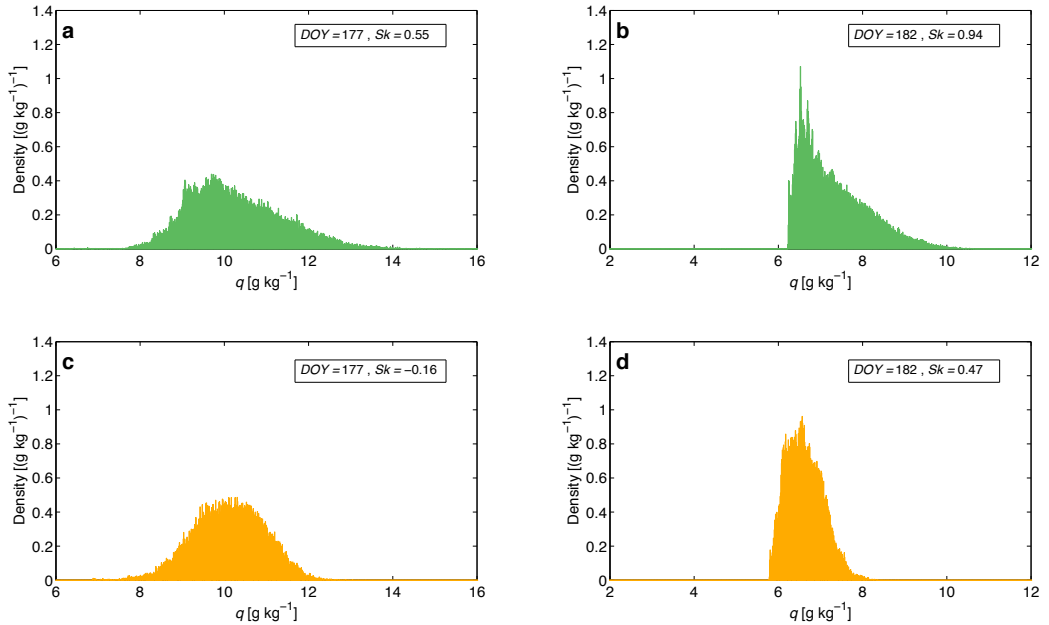


Figure 3.9: Density distributions of humidity at DOY 177 (left, a day with predominant large-scale influences) and DOY 182 (right, a day without a predominant large-scale influence) obtained over the grass (top, green) and the fodder (bottom, yellow) at 1300–1400 UTC

DOY 176–178 and 186 and the other days remained ≈ 20 min for all intervals. Moreover, we did not observe a trend in TS within the tested intervals.

Distribution of Humidity Signal

In Figure 3.8 we compare the midday skewnesses of humidity between the two fields. Over the grass we find values around 0.9, and only for DOY 176, 177 and 178, skewnesses are lower, around 0.5. For fodder, Sk_q is generally lower than for grass (around 0.4), caused by lower latent heat fluxes and thus a smaller humidity range at the right part of the distributions in Figures 3.9c, d. Consequently, the relative importance of non-local effects (left part of the distributions in Figures 3.9a, c) is larger above the fodder, which lowers the skewness even more. Sk_q values observed over the fodder reduce to zero on the same days as for which lower values were found over the grass (DOY 176–178). As discussed in Section 3.2.2, humidity skewnesses close to zero are an indication of the signal being not only influenced by surface-layer processes.

As entrained air from the free atmosphere is clearly drier than that of the CBL, we relate the extra variance on the dry side of the distribution at the fodder field to entrainment. An alternative explanation for the enhanced variance on the dry side of the distribution could be horizontal advection from the town of Lannemezan (2 km to the south-east of the site). However, south-easterly winds occur also on

days where the humidity signal does not show low skewnesses and large time scales. Furthermore, in the east-west direction the town is only ≈ 500 m wide. Hence, it is questionable whether the town has a significant impact on the humidity signal over the measurement site (e.g. in contrast to the study of Tapper (1990), which refers to a much larger town). For a further discussion on the effect of surface heterogeneity, see Section 3.4.5.

3.4.4 Relations Between ASL Observations and Entrainment Regime

We analyzed all radiosoundings to obtain the boundary-layer height, entrainment latent heat flux, and the local entrainment ratio (as presented in Section 3.2.2). Boundary-layer heights at 1400 UTC varied between 600 and 1400 m (above ground level, a.g.l.), and the entrainment latent heat flux varied considerably, between 24 and 972 W m^{-2} (see Tables 3.1 and 3.2 in Section 3.3.2).

In Section 3.4.3 we implied that entrainment processes influenced the observed turbulence at DOY 176–178 and partly on DOY 186. This is in agreement with the local entrainment ratios we found for humidity over the fodder; β_q was more than three times larger than was β_θ on DOY 176, 177, 178, 186 and also partly on DOY 170 (see also Tables 3.1 and 3.2).

A clear difference in β_q between the radiosoundings at a distance of 1 and 4 km is not apparent (last column in Tables 3.1 and 3.2); however, some ambiguity exists with respect to β_q . To determine whether this is site-dependent, more radiosondes should have been launched during daytime at both locations at exactly the same time. The calculation of β_q is very sensitive to the estimation of the area-averaged surface fluxes and to the determination of the jumps of θ_v and q at the boundary-layer top, for which we use local profiles of θ_v and q that may differ from the area-averaged profiles.

In Section 3.4.3 it was shown how entrainment enhances the large-scale variance in the ASL. In Figure 3.10 we show the contribution of large-scale variance (variance at time scales >10 min) to the total variance as a function of entrainment ratio. Above the grass, β_q is not large enough to confirm a clear relationship with the large-scale variance. At the fodder, the relative contribution increases with increasing entrainment ratio. However, observed relative variances do not confirm the black lines that show the sum of the entrainment term $\beta_q^2 f_e$ and covariance term $\beta_q f_{es}$ divided by the sum of all three terms following Equation 3.11. For f_e , we applied both the function presented in Figure 3.12a in Moeng and Wyngaard (1989) and Equation 3.8, which we derived from the LES data of Patton et al. (2003). Both top-down variance-related estimates do not fully explain the relative contribution of larger-scale processes that was detected in the data. The variance-budget derived estimate (thin dashed line) shows a better agreement with the measurements. However, also for this approach, the observations contain a greater large-scale humidity

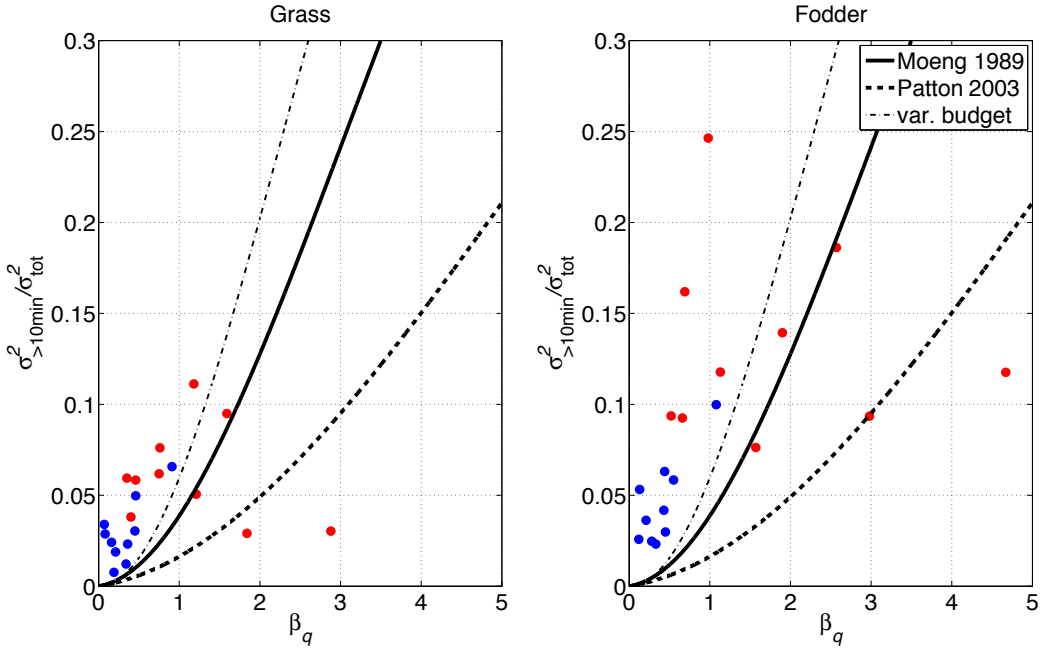


Figure 3.10: The contribution of variance at a time scale >10 min to the total variance increases with the entrainment ratio. Black lines: contribution of entrainment-related variance to the variance following Moeng and Wyngaard (1989), our fit after Patton et al. (2003), and Equation 3.18 derived from the variance budget. The dots are based on hours of humidity data for which also radiosonde data were available. The black line shows Equation 3.9 for representative values for ‘entrainment days’ (Tables 3.1 and 3.2). Red dots indicate observations on ‘entrainment days’ (Section 3.3.2)

variance than is estimated from the variance budget.

As we use the LES-derived scaling profiles of Moeng and Wyngaard (1989) and Patton et al. (2003) down to a level where in the simulations the subgrid-scale processes may dominate, the exact value of the scaling profile should be considered with some care. However, the strongest height dependence in the ratio of top-down variance to total variance is due to the height dependence of the surface-related variance. The higher surface flux combined with the same entrainment flux produces a smaller contribution of large-scale variance to the total variance above the grass than above the fodder. This indicates that surface-layer measurements are not affected by the larger-scale processes over the grass (with larger $L_V E$) on any day, in contrast to the fodder field measurements (smaller $L_V E$).

The observed simultaneous variation of entrainment ratio and skewness suggests that they are correlated. In Figure 3.11 we show that the entrainment ratio can be written as a function of humidity skewness,

$$\beta_q = 1.5 - 1.1 \frac{Sk_q}{Sk_{q \text{ ref}}}, \quad (3.21)$$

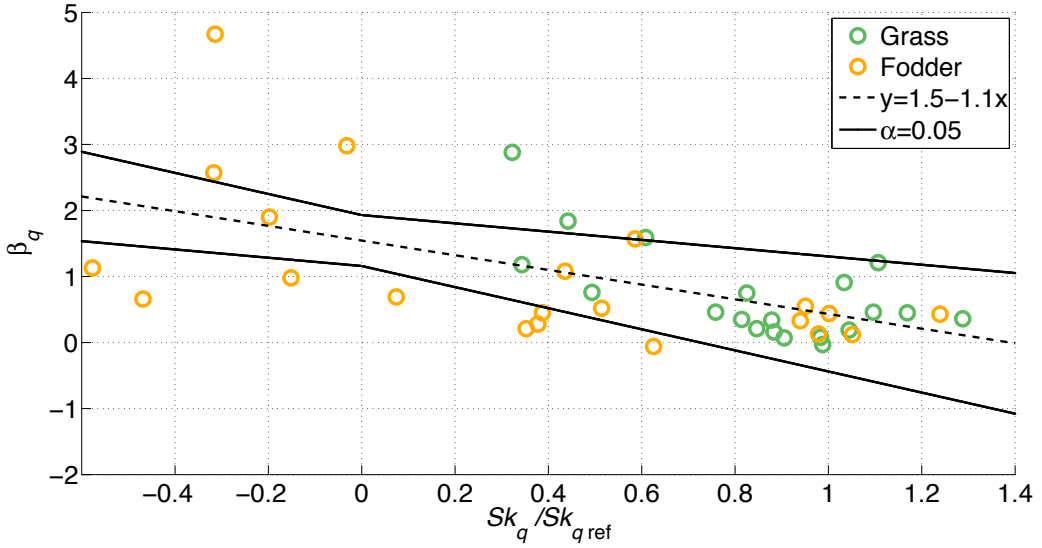


Figure 3.11: The normalized Sk_q (each based on 1 h of humidity data for which also radiosonde data were available) decreases with the entrainment ratio for both land-use types for a 95 % confidence interval (black continuous lines). $Sk_{q\text{ ref}} = 0.9$ for grass and 0.5 for fodder

in which Sk_q is normalized with a reference value ($Sk_{q\text{ ref}}$) of 0.9 and 0.5 for grass and fodder respectively. These reference values are the humidity skewnesses in the case of relatively weak entrainment (see Figure 3.8), which correspond to $\beta_q \approx 0.3$ (see Figure 3.11). The 95 %-confidence intervals for the offset and slope respectively are [1.2 2.0] and [-1.7 -0.7].

Equation 3.21 could be combined with Equations 3.11 and 3.18 to obtain a function for surface-layer scaling, in the case where only surface-layer measurements are available (note that z/z_i still needs to be estimated).

3.4.5 MO Similarity Theory in Relation to Entrainment Data

Figure 3.12 is similar to Figure 3.5d, but with different criteria for colouring the data, and with only data from IOP days. Red crosses are data from DOY 176–178 and DOY 186, days for which we found larger time scales in wavelet spectra, and a lower Sk_q than usual, and which we both relate to the impact of entrainment on surface-layer turbulence. MO similarity theory is especially invalid on those days; the red crosses ($c_1 = 15.8 \pm 0.6$) deviate more from the flux-variance relation with $c_1 = 8.4$ (De Bruin et al. 1993) than do the blue squares ($c_1 = 13.5 \pm 0.5$). We found (not shown) that although humidity variance observed above the grass is captured quite well by Equation 3.2, there is a slight difference (not significant) between the days with ($c_1 = 10.1 \pm 0.8$) and without ($c_1 = 9.1 \pm 0.3$) surface-layer indications for entrainment. Above the fodder for days that we marked as ‘no dominance of entrainment’, c_1 still deviates from its literature value. This means that, above the

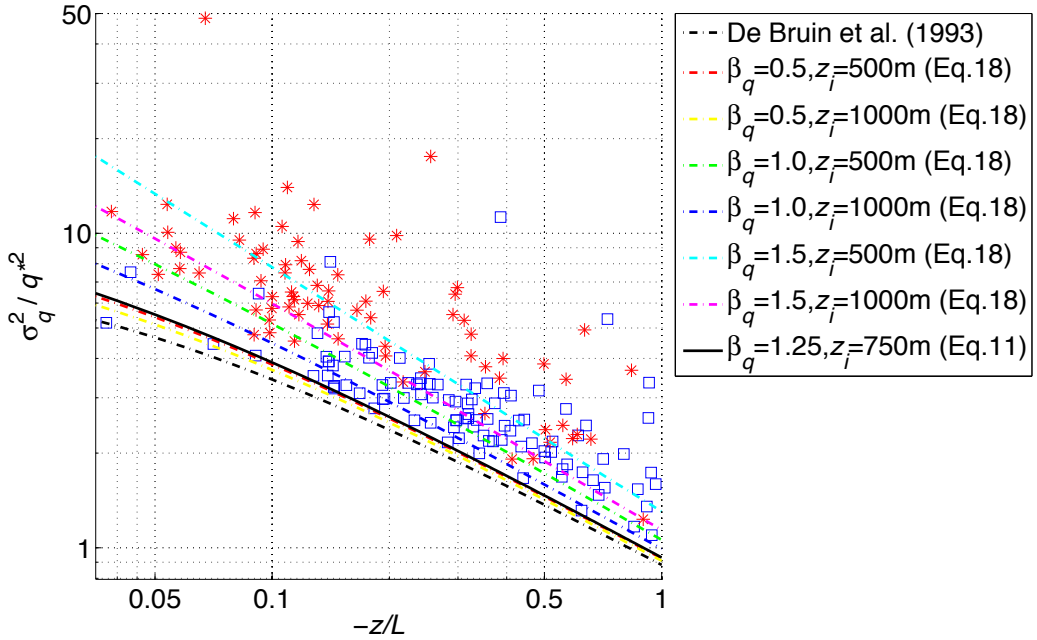


Figure 3.12: Normalized variances of humidity above the fodder depending on atmospheric stability for 30-min intervals, including the Monin–Obukhov similarity function proposed by De Bruin et al. (1993). Dashed lines show Equation 3.18 for a range of boundary-layer depths and entrainment ratios. The black line shows Equation 3.11 for representative values for ‘entrainment days’ (Tables 3.1 and 3.2). Red dots indicate observations on ‘entrainment days’ (Section 3.3.2). Blue squares indicate days without signs of direct entrainment influences on the ASL (only data of IOP days are shown here)

fodder, next to entrainment, other processes disturb the MO similarity relationships. De Bruin et al. (1999) argue that violation of MO similarity theory occurs if fluxes generated by surface heating or surface evaporation are of the same order as non-locally (entrainment or local advection) generated fluxes. In our case, violation of the theory occurs if $\beta_q > 0.6$ (for $\beta_{\theta_v} = -0.2$ and derived from days on which we found a high TS and a low Sk_q).

Our results presented in Figure 3.5a, b indicate that standard MO similarity is captured well for temperature. However, the results presented above imply that the standard MO similarity functions for humidity miss a relevant variable, especially under conditions of relatively strong entrainment. The variance produced by entrainment processes is, as expected, larger for a larger entrainment ratio, and it is smaller for deeper boundary layers (dashed lines in Figure 3.12, calculated solely from the boundary-layer scaling theory after Equation 3.18). The deviations from MO similarity theory observed in Figure 3.12 correspond to extra variance produced by entrainment processes for β_q between 1.0 and 1.5, and z_i between 500 and 1000 m, which are both realistic values for our measurement campaign. The sum of variance predicted from MO similarity theory and the LES-based function (Equation 3.11) at $\beta_q = 1.25$ and $z_i = 750$ m (representative values from Tables 3.1 and 3.2 for days

with significant entrainment influences) is clearly lower than the variance observed on days with signs of relatively strong entrainment (which we concluded before from Figure 3.10). This result indicates that, by using the budget-derived approach, we are able to correct the universal functions derived from MO similarity theory for a strong influence of entrainment relative to the surface. However, to improve the LES-based estimations of τ_D , $\frac{\partial \bar{q}_e}{\partial z}$, and $\frac{\partial \overline{w'q_e'^2}}{\partial z}$ (Section 3.2.1), they should be based on LES with a higher vertical resolution in the ASL than in Moeng and Wyngaard (1989).

Through the relation we observed between Sk_q and β_q (Equation 3.21), we can use Sk_q instead of β_q in the budget (and LES) derived equations to add the normalized variance produced due to entrainment to the normalized variance expected following MO similarity theory; z_i is still needed for both equations (Equations 3.11 and 3.18). However, a robust guess will suffice because $(z/z_i)^{-2/3}$ in the budget-derived equation and $(z_i/L)^{-2/3}$ in the LES-derived equation are both not very sensitive to z_i .

One could wonder whether advection or the horizontal turbulent transport of humidity variance plays a role here. A horizontal humidity gradient could produce extra variance in addition to the MO similarity functions. Therefore, we estimate these contributions from the humidity variance budget equation for stationary conditions, aligned with the mean wind with negligible mean vertical wind speed,

$$\bar{u} \frac{\partial \overline{q'q'}}{\partial x} = -2\overline{u'q'} \frac{\partial \bar{q}}{\partial x} - 2\overline{w'q'} \frac{\partial \bar{q}}{\partial z} - 2\epsilon_s - \frac{\partial \overline{u'q'q'}}{\partial x} - \frac{\partial \overline{w'q'q'}}{\partial z}. \quad (3.22)$$

We approximate the total normalized humidity variance for a horizontally heterogeneous flow from this budget by writing the dissipation term as $\epsilon_s \approx \frac{1}{2} \sigma_q^2 / \tau_D$ and transferring it to the left-hand side. We move the horizontal variance advection term to the right-hand side, normalize both sides with q_*^2 , and multiply both sides with the ASL dissipation time scale $\tau_D \approx \kappa z / u_*$. If we assume that vertical flux divergence is negligible, and estimate the budget terms following the relevant scales given in Moene and Schüttemeyer (2008) in their Section 3.2.1, we obtain

$$\frac{\sigma_q^2}{q_*^2} \approx \frac{\bar{u}}{u_*} \left(\frac{\Delta q_*}{q_*} \right)^2 \frac{\kappa z}{L_x} + \frac{\Delta q_*}{q_*} \frac{2\kappa z}{L_x} + 2 + \left(\frac{\Delta q_*}{q_*} \right)^2 \frac{\kappa z}{L_x}, \quad (3.23)$$

in which the terms are placed in the same order as in Equation 3.22, representing horizontal variance advection, production by a horizontal gradient, production by a vertical gradient, and horizontal turbulent transport. The order of magnitude of the production term due to a vertical gradient of humidity (which is approximately 2 in Equation 3.23), corresponds to the estimated variance from the MO similarity function of De Bruin et al. (1993) for unstable conditions. The other three terms increase with the magnitude of the relative horizontal contrast in humidity flux, $\Delta q_*/q_*$ (Δq_* is the horizontal difference between the turbulent scales of humidity for the two locations), and decrease with the horizontal length scale L_x at which this humidity

contrast is observed. The horizontal variance advection furthermore depends on \bar{u}/u_* , which is larger for neutral conditions.

With typical values for the fodder field of this study, the city at 2 km with a roughly estimated latent heat flux of 50 W m^{-2} theoretically creates extra normalized variance of $\approx 2 \times 10^{-3}$. This value is negligible compared to the variance observed above the fodder (shown in Figure 3.12). The estimate of the effect of the grass field next to the wheat field ($L_x = 50 \text{ m}$) is approximately 2×10^{-2} for humidity ($\Delta L_v E = 100 \text{ W m}^{-2}$) and 8×10^{-2} for temperature ($\Delta H = 175 \text{ W m}^{-2}$). From this we conclude that the extra variance we observed was mainly created by entrainment influences, and hardly any by surface heterogeneity or advection.

3.5 Conclusion

Monin–Obukhov similarity relationships for the variance of humidity were shown to deviate from their documented values for observations made a few metres above a drying fodder field. It turns out that on days with the largest deviations (DOY 176–178 and 186 during the BLLAST campaign in southern France in 2011) a number of metrics derived from the surface-layer observations suggest the effect of entrainment processes:

- Skewnesses of humidity distributions were significantly lower than they were on days with small deviations from Monin–Obukhov similarity theory (which we relate to entrainment in the case of a dry surface)
- Contributions to the humidity variance were observed at a time scale corresponding to z_i/w_* , the boundary-layer height divided by the vertical velocity scale ($\approx 20 \text{ min}$).

Analysis of radiosonde data, and in particular the magnitudes of the entrainment flux of humidity relative to the corresponding surface flux over the fodder field (local entrainment ratio β_q), revealed that indeed the affected days showed high entrainment ratios. Therefore, we could use the ASL observations to identify days with a predominance of entrainment.

The observed additional variance in q on days where the ASL is affected by entrainment is in accordance with the variance produced by entrainment processes, estimated from a simplification of the variance budget equation. We built on the work of e.g. De Bruin et al. (1999), Moene et al. (2006), and Lohou et al. (2010), and succeeded in developing a robust method to detect and quantify entrainment influences on surface-layer data, based on eddy-covariance data at low levels in the ASL.

We identified a surface-layer scaling function for humidity that includes the entrainment effect, and which requires atmospheric stability, a rough estimate of z_i , and either β_q or skewness statistics of the surface-layer humidity observations. This

relationship could be used for further surface-layer data analysis. Furthermore, the presented methods (and some of the equations) can be tested and applied for more scalars, such as CO₂ concentration or reactive species.

3A Appendix

Vertical profiles of temperature (red) and humidity (blue) from all successful radiosoundings at a site 1 km from our EC stations are shown in Figure 3A.1. We manually added a first-order jump model to every vertical profile (black lines). Corresponding surface and entrainment fluxes are given in Table 3.1. Soundings launched at a site 4 km from our EC stations and contributing calculated fluxes are shown in Figure 3A.2 and in Table 3.2 respectively.

Acknowledgments

We greatly thank Oscar Hartogensis, Olivier de Coster, Henk Pietersen (Wageningen UR, the Netherlands) and Martin Lennefer (University Bonn, Germany) for their help with EC measurements before, during and after the BLLAST campaign. Furthermore, we thank Christine Moene for assisting in mapping the surroundings of the EC stations. We also thank Miranda Braam for her assistance with data processing and visualizing Fig. 3.1, and Jordi Vilà-Guerau de Arellano and Huug Ouwersloot (Wageningen UR, the Netherlands) for their critical notes on our study. We thank Fabienne Lohou (Laboratoire d'Aérodynamique Toulouse, France) and two anonymous reviewers for their critical comments and helpful suggestions. Furthermore, we thank Ned Patton (NCAR Boulder, US) for providing the detailed data from his LES study of 10 years ago. This work was financed by the DFG (Deutsche Forschungsgemeinschaft) project GR2687/3-1 and SCHU2350/2-1; links between local-scale measurements and catchment-scale measurements and modelling of gas exchange processes over land surfaces. The BLLAST field experiment was made possible thanks to the contribution of several institutions and supports: INSU-CNRS (Institut National des Sciences de l'Univers, Centre national de la Recherche Scientifique, LEFE-IDAO program), Météo-France, Observatoire Midi-Pyrénées (University of Toulouse), EUFAR (EUropean Facility for Airborne Research) and COST ES0802 (European Cooperation in the field of Scientific and Technical). The field experiment would not have occurred without the contribution of all participating European and American research groups, which all have contributed in a significant amount (see supports). The BLLAST field experiment was hosted by the instrumented site of Centre de Recherches Atmosphériques, Lannemezan, France (Observatoire Midi-Pyrénées, Laboratoire d'Aérodynamique). BLLAST data are managed by SEDOO, from Observatoire Midi-Pyrénées. The MODEM radiosoundings were supported by CNRS, University of Toulouse and the FEDER program (Contract nr. 34172—Development of the instrumentation of Observatoire Midi-Pyrénées—PIRENEA—ESPOIR). The 60-m tower equipment was also supported by CNRS, Université Paul Sabatier and by the European POCTEFA FluxPyr program.

3. ENTRAINMENT INFLUENCES ON SURFACE LAYER MEASUREMENTS

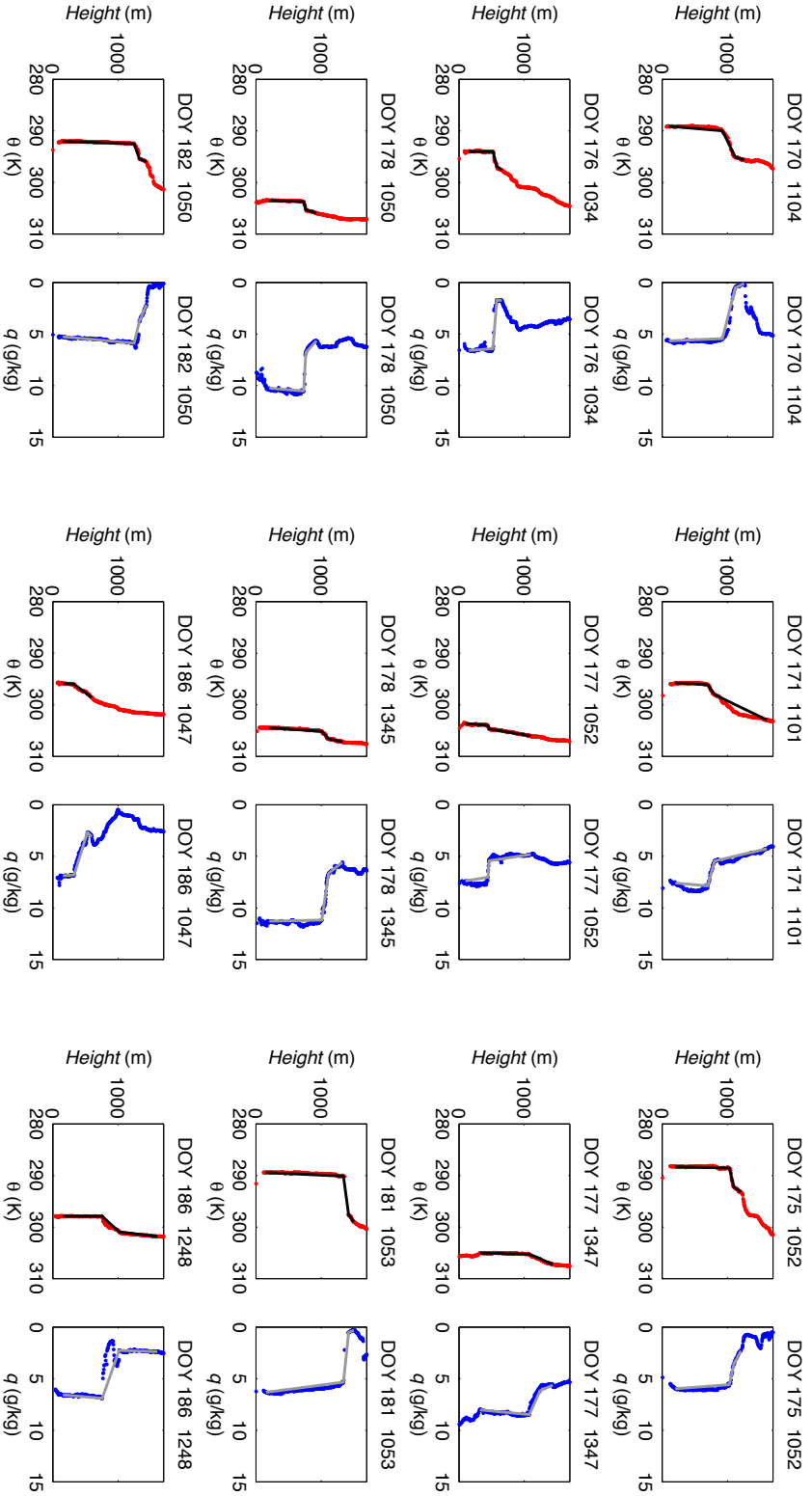


Figure 3A.1: Vertical profiles of temperature (red) and humidity (blue) obtained at a distance of 1 km from our EC stations, using radiosoundings (MODEM). From left to right, then from top to bottom, the sets of θ and q are placed in chronological order. Black lines indicate the first-order jump model. Corresponding DOY and time are given above every vertical profile

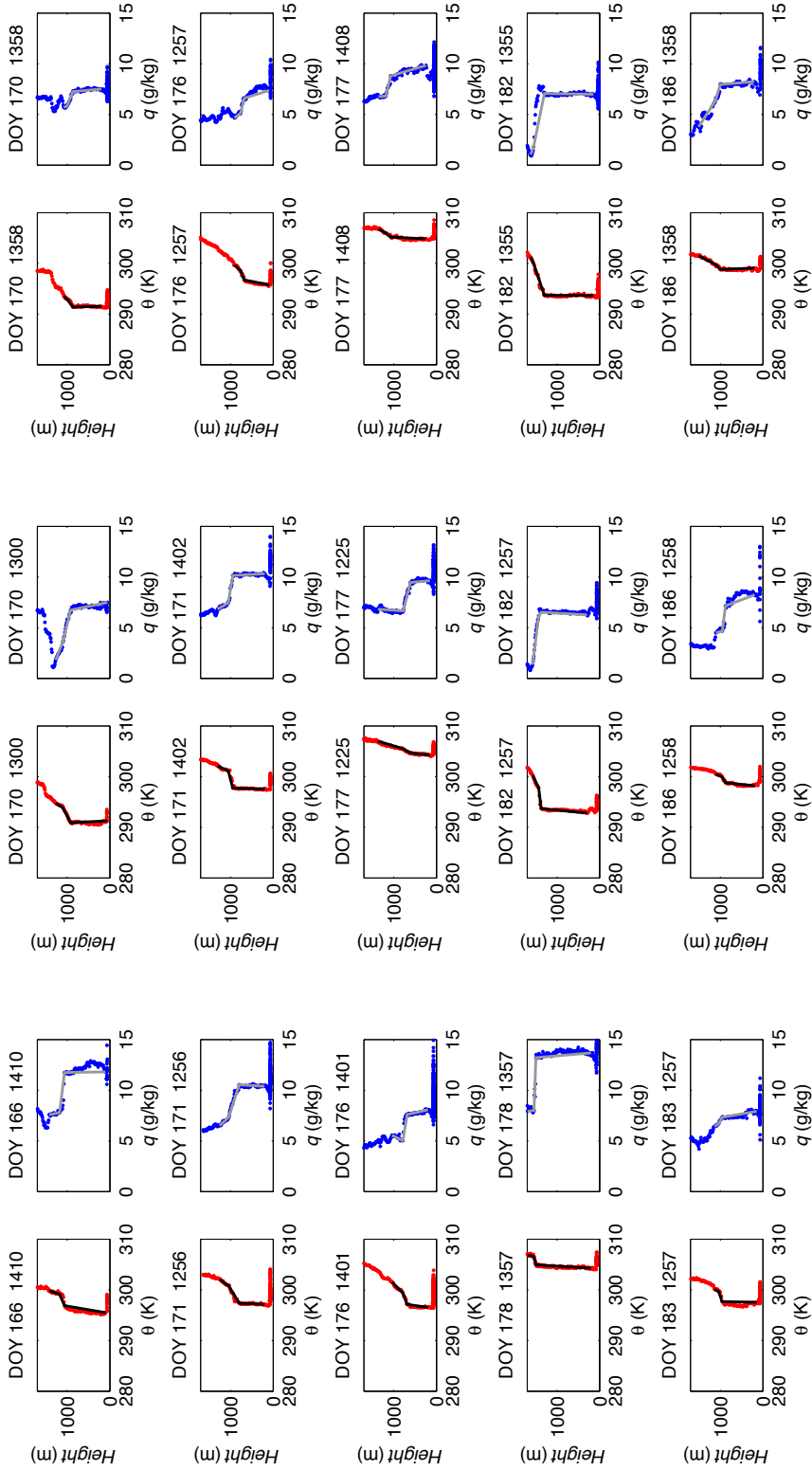


Figure 3A.2: Vertical profiles of temperature (red) and humidity (blue) obtained at a distance of 4 km from our EC stations, using radiosoundings (Vaisala). From left to right, then from top to bottom, the sets of θ and q are placed in chronological order. Black lines indicate the first-order jump model

4

Estimation of the refractive index structure parameter from single-level daytime routine weather data

Atmospheric scintillations cause problems for applications where an undistorted propagation of electromagnetic radiation is essential. These scintillations are related to turbulent fluctuations of temperature and humidity that are in turn related to surface heat fluxes. We developed an approach that quantifies these scintillations by estimating C_{n^2} from surface fluxes that are derived from single-level routine weather data. This approach allows for an efficient evaluation of the performance of e.g. infrared imaging systems, laser geodetic systems, and ground-to-satellite optical communication systems. We tested our approach for two grass fields in central and southern Europe, and for a wheat field in central Europe. Although there are uncertainties in the flux estimates, the impact on C_{n^2} is shown to be rather small. The C_{n^2} daytime estimates agree well with values determined from eddy covariance measurements for the application to the three fields. However, some adjustments were needed for the approach for the grass field in southern Europe because of dominant boundary-layer processes instead of surface-layer processes.

This chapter is published as van de Boer et al. (2014b).

4.1 Introduction

Atmospheric turbulence and the related fluctuations of the refractive index of air affect the propagation of electromagnetic waves. These scintillations are a problem for communication and imaging systems (e.g. ground-based telescopes) that use radiowaves, visible, or infrared radiation (Tunick, 2002). Fluctuations in the refractive index of air are mainly related to temperature, humidity, and pressure. Therefore, turbulent fluctuations of temperature and humidity determine the intensity of turbulence-induced refraction. Various instruments and calculation methods have been developed to obtain the structure parameter of the refractive index of air (C_{n^2}) for a certain wavelength, to qualify signals of imaging or communication systems that use electromagnetic radiation. However, these instruments (sonic anemometer, scintillometer, air refractometer) are not easy to operate and expensive, such that frequent observations are rare. A robust method to quantitatively estimate C_{n^2} based on readily available data is therefore needed.

Already forty years ago, Wyngaard et al. (1971) developed a semi-empirical theory which relates the temperature structure parameter C_{T^2} (which is related to C_{n^2}) to atmospheric stability and the vertical temperature gradient at a certain height in the atmospheric surface layer (the lowest meters of the atmosphere). In the years after, several studies showed that C_{n^2} does not only depend on C_{T^2} , but also on the humidity structure parameter C_{q^2} and on the joint structure parameter C_{Tq} (Wesely, 1976). For wavelengths in the visible and near-infrared, C_{n^2} mainly depends on C_{T^2} , while for radio wavelengths, C_{q^2} mainly determines C_{n^2} . A summary of past research on models and measurements for optical turbulence is presented in Tunick (2002). Friehe (1977) and Davidson et al. (1978) estimated C_{n^2} from dual-level meteorological data over the ocean for visible light. Andreas (1988) performed a sensitivity study for a) a C_{n^2} derivation method based on observed surface fluxes of heat, moisture and momentum using Monin-Obukhov similarity theory (Monin and Obukhov, 1954), and for b) a method based on dual-level meteorological data. He tested both methods above snow for a broad wavelength range (visible, infrared, millimeter, and radio).

However, fluxes or vertical gradients are usually not available from regular meteorological observations. Therefore, Sadot and Kopeika (1992) developed a method based on single-level standard weather-station data to estimate C_{n^2} in the atmospheric surface layer. Also, weather forecasts can be used to predict C_{n^2} by their method. The method needs, however, several empirical parameters which were only derived for a desert region, and which need to be first determined for other regions. Rachele and Tunick (1994) and Bendersky et al. (2004) developed methods to similarly obtain C_{n^2} from single-level weather data for prairie grasslands and coastal environments, which are, however, also not generally applicable. Cheinet and Cumin (2011) show how C_{n^2} at different heights within the boundary layer could be derived from atmospheric turbulence models. However, a very fine vertical resolution of

their model would be needed, which is usually not practical. Thus, robust and easy-to-use methods for estimating C_{n^2} from single-level weather data are lacking, which motivates our study.

The daily course of C_{n^2} depends on the atmospheric conditions which depend on the time of the day, the day of the year (DOY), and the weather type of that specific day. Observations of C_{n^2} above a grass field in the Netherlands are given in Figure 4.1 for cloudy and clear sky conditions, for a summer and an autumn day, for an optical and a millimetre wavelength. With our scheme, we hope to capture both the daily and seasonal changes of C_{n^2} for different locations.

We use an adaptation of the scheme introduced by Holtslag and van Ulden (1983) and de Rooy and Holtslag (1999), later referred to as dRH99, that estimates surface heat and moisture fluxes from air temperature, humidity, pressure, wind speed and incoming shortwave radiation. This scheme is based on the Penman-Monteith equation, which estimates evapotranspiration rates from atmospheric conditions and vegetation specific parameters (e.g. canopy resistance, surface albedo and roughness) that are all easy to estimate. Our implementation of the scheme of dRH99 is described in Section 5.2 and Appendix A. In Section 5.2, we also explain in more detail how C_{T^2} , C_{q^2} and C_{Tq} are derived from surface fluxes (using Monin-Obukhov similarity theory), and how C_{n^2} is derived from the meteorological structure parameters. Our method can be used to provide insight on optical turbulence at a specific location for a certain moment, but also for a period of several years. Estimates of optical turbulence effects on electro-optic or laser systems could be derived, mainly for horizontal atmospheric paths. The complete scheme that estimates C_{n^2} from standard single-level weather data follows from the Appendix and Section 4.2.2 and 4.2.3.

We validate estimated fluxes and structure parameters with summertime measurements from different locations and vegetation types: grass in the Netherlands, grass in the South of France, and wheat in the West of Germany. In Section 4.3, we describe the datasets, and in Section 4.4 we explain the evaluation of our scheme. We restrict ourselves to daytime data because at night, Monin-Obukhov similarity theory is often not valid. Moreover, we use surface flux observations for the scheme validation, which are ambiguous during the night because of low values. In Section 5.4, we compare fluxes and structure parameters derived using our method with high frequency measurements (eddy covariance). In contrast to other methods, our scheme only weakly depends on empirical assumptions and is computationally cheap.

4.2 Framework

In this section, we describe how we derive C_{n^2} from the atmospheric variables temperature, humidity, pressure, wind speed and radiation, and from the surface char-

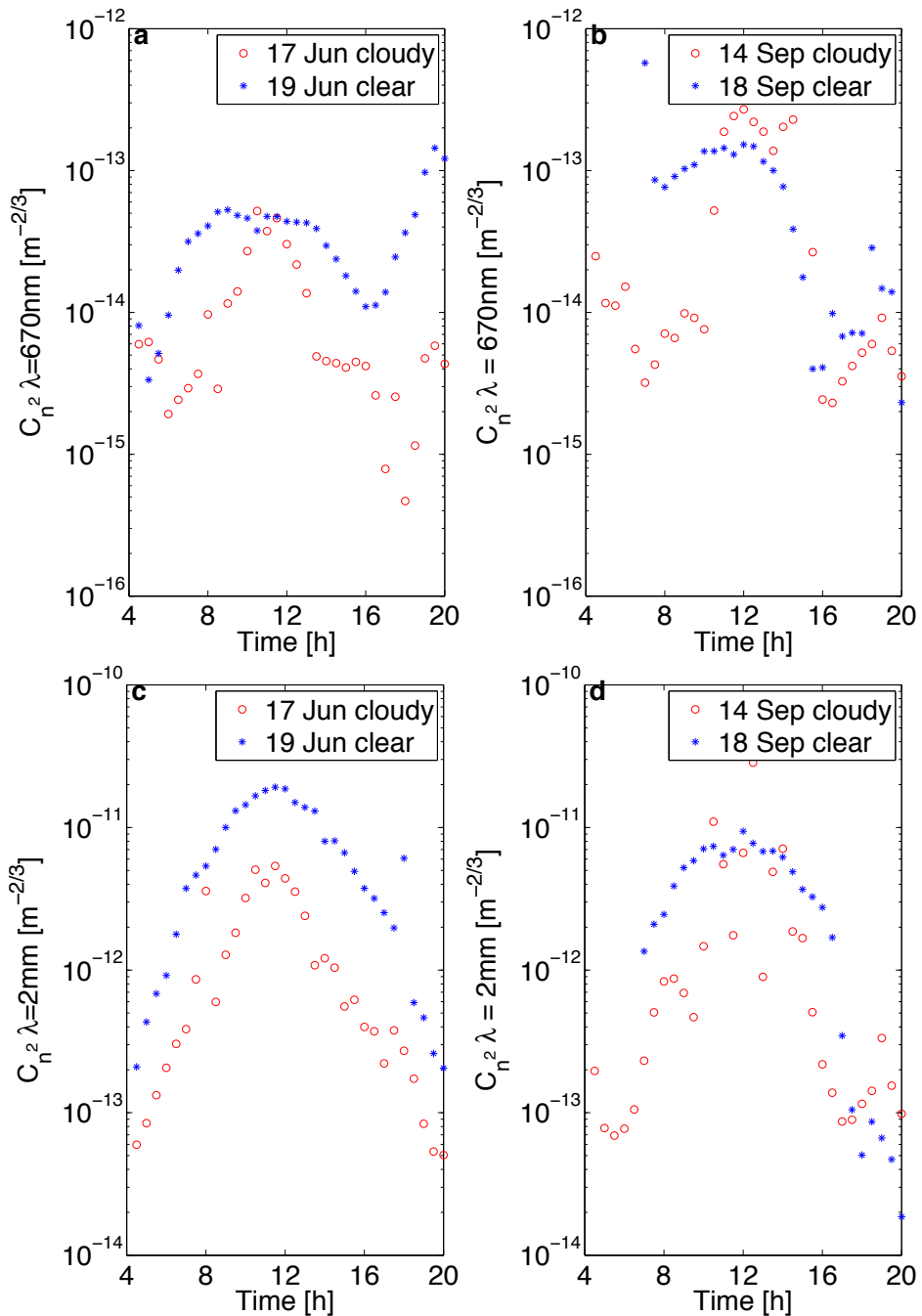


Figure 4.1: Daily course of observed values of C_{n^2} for $\lambda = 670\text{nm}$ (a and b) and $\lambda = 2\text{mm}$ (c and d) for different weather types (blue is clear sky, red is cloudy) and seasons; summer (a and c) and autumn (b and d) above a grass field in the Netherlands (Haarweg Wageningen, 2005).

acteristics albedo, roughness, leaf area index, vegetation height and the minimal stomatal resistance of the canopy. Our scheme follows three steps. First (Section 4.2.1), fluxes are estimated from the single-level weather data using an adaptation of an existing scheme. Then (Section 4.2.2), these fluxes are used to estimate the structure parameters C_{T^2} , C_{q^2} and C_{Tq^2} , following Monin-Obukhov similarity theory. C_{n^2} is finally estimated from the latter (Section 4.2.3) using theory described by Ward et al. (2013).

4.2.1 Estimation of surface fluxes from single-level weather data

dRH99 presented a scheme that relates surface fluxes of momentum and sensible and latent heat to only a few weather variables. They successfully tested their scheme for a full year of observations above a grass field in Cabauw, the Netherlands. The scheme consists of an iteration loop with the following parameters needed for the Penman-Monteith equation: net radiation Q_n , soil heat flux G , and canopy and aerodynamic resistances r_c and r_a . The canopy resistance together with the aerodynamic resistance determine the partitioning between sensible and latent heat flux. In the Penman-Monteith equation, the latent heat flux (L_vE) is calculated as

$$L_vE = \frac{s(Q_n - G) + \frac{\rho c_p}{r_a}(e_{\text{sat}} - e_a)}{s + \gamma(1 + \frac{r_c}{r_a})}. \quad (4.1)$$

The sensible heat flux H can be calculated as a residual of the surface energy balance $Q_n - G - L_vE$. In Equation 4.1, $e_{\text{sat}} - e_a$ is the water vapour deficit in Pa, where e_a is the water vapour pressure and e_{sat} is the saturation pressure of water vapour (which only varies with temperature). s is the slope of the saturated vapour pressure curve $s(T) = de_{\text{sat}}/dT$, ρ is the air density, c_p is the specific heat capacity of air at constant pressure (p) that depends on humidity, and γ is the psychrometric constant (given in Appendix A). Note that Equation 4.1 describes transpiration only. However, if r_c would be set to zero, evaporation of intercepted water is simulated.

To obtain L_vE , the estimation of the surface skin temperature is crucial because of its role in both Q_n and G . The estimation of the surface skin temperature depends on r_a , that in turn depends on the friction velocity u_* . Because u_* depends on atmospheric stability, the surface skin temperature is estimated via an iteration that starts with a neutral atmosphere (further explained in Sec. 4.4). The radiation balance and thus the available energy for heat fluxes further depends on the downward shortwave radiation (S_{in}), the surface albedo (α), cloud cover, surface longwave emissivity, and atmospheric longwave emissivity.

Our scheme to solve Equation 4.1 to estimate heat fluxes from single-level weather data is given in Appendix A. In this section, we discuss the adaptations that we made to the scheme of dRH99 regarding r_c and radiation calculations. Because the scheme of dRH99 was only tested for one specific grass field in the Netherlands,

its performance for other regions or vegetation types is uncertain. E.g. their empirical parametrization $r_c = 10^4 \Delta q = 10^4 (e_{\text{sat}} - e_a) \frac{R_d}{\rho R_v}$ is not generally applicable for warmer or dryer regions (Δq is the specific humidity deficit in kg kg^{-1} , calculated as $q_{\text{sat}} - q$, and R_d and R_v are the specific gas constants for dry air and for water vapour respectively; 287 and 462 $\text{J kg}^{-1} \text{K}^{-1}$).

We here show a comparison of the approximations for the dependency of r_c on water vapour deficit given by dRH99 and by Beljaars and Bosveld (1997), referred to as BB97, and three approximations used in the land-surface schemes of the weather and climate models of a) the National Centre for Meteorological Research in France (CNRM, the ISBA-Ags scheme), b) the United States National Centers for Environmental Prediction (NCEP, the Noah scheme), and c) the European Centre for Medium-range Weather Forecasts (ECMWF, the HTESSEL scheme). The Noah and HTESSEL schemes are based on the Jarvis-Stewart approach (Jarvis, 1976; Stewart, 1988), where

$$r_c = \frac{r_{s,\min}}{LAI} f_{dq} f_{\text{rad}} f_T f_\theta. \quad (4.2)$$

This approach is based on $r_{s,\min}$, a minimum stomatal resistance for optimal conditions, which is vegetation dependent (see Table 4.1), and that is scaled from a square meter of leaf surface to a canopy with a specific leaf area index (LAI , see Table 4.1 as well). The four functions represent the reaction of vegetation to environmental factors: global radiation, water vapour deficit, air temperature, and soil moisture. In this discussion, we only address the water vapour deficit dependency. In Noah, f_{dq} is calculated as $1 + h_s \Delta q$ (Chen and Dudhia, 2001), where h_s is an empirical coefficient that describes the reaction of stomatal resistance on humidity deficit. $h_s \approx 45 \text{ kg kg}^{-1}$, the inverse of K_3 in Stewart and Gay (1989). The Ags scheme contains a similar type of response, but with $h_s = 58 \text{ kg kg}^{-1}$. In HTESSEL, $f_{dq} = e^{g_D \frac{8}{5} \rho \Delta q}$ is used, which has a similar effect as the Noah implementation (see Figure 4.2) for $g_D = 0.02 \text{ mb}^{-1}$ ($g_D = 0.03 \text{ mb}^{-1}$ for trees and zero for crops in HTESSEL). BB97 calculate the canopy resistance as

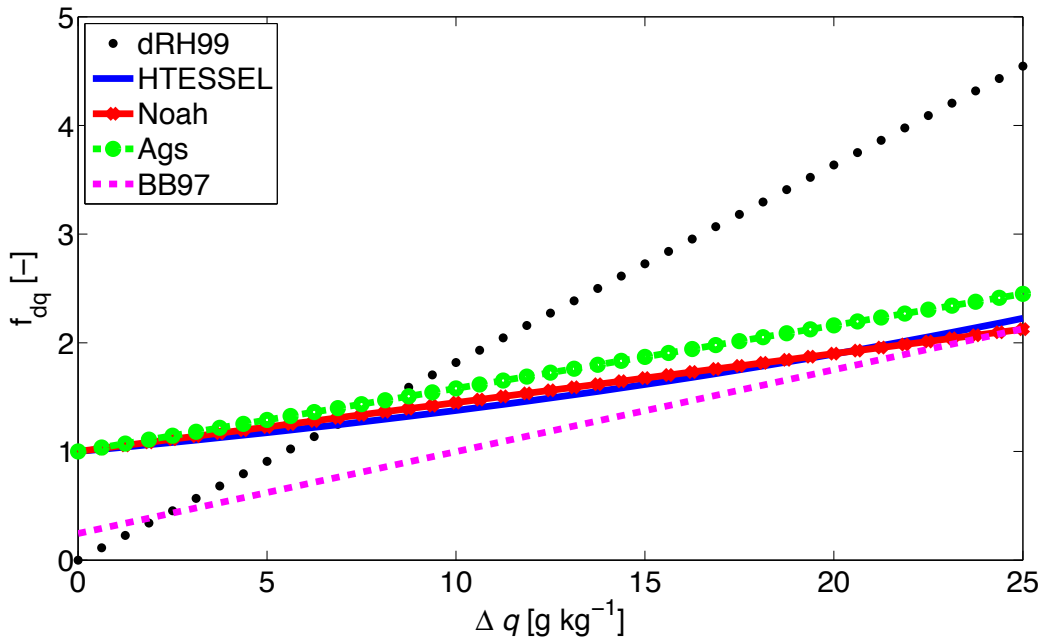
$$r_c = 25.9 f_{dq} f_{\text{rad}} f_\theta, \quad (4.3)$$

where $f_{dq} = 1 + h_s (\Delta q - \Delta q_0)$. $h_s = 160 \text{ kg}^{-1} \text{ kg}$, $\Delta q_0 = 0.003 \text{ kg}^{-1} \text{ kg}$, and the factor 25.9 represents a specific $\frac{r_{s,\min}}{LAI}$.

The approach of dRH99 significantly deviates from the other approximations (Figure 4.2). Their response function (and thus the canopy resistance) at zero water vapour deficit (relative humidity of 100%) is zero. Herewith, dRH99 empirically take into account that at low water vapour deficits, the evapotranspiration term is dominated by evaporation whereas it is assumed in the Penman-Monteith equation that transpiration is the only contribution to evapotranspiration. For the three land surface schemes, the response function is one ($r_c = r_{s,\min}/LAI$), and it is 0.24 according to BB97 for a saturated atmosphere. The other difference is that the function of dRH99 shows a much stronger increase of r_c with Δq than the other four functions,

Table 4.1: Vegetation types and parameter values after the ERA40 surface scheme (HTESSEL) used in the ECMWF model.

Vegetation	$r_{s,\min}$	LAI
Low crops, mixed farming	180	3
Irrigated low crops	180	3
Short grass	110	2
Tall grass	100	2
Low shrubs	225	3
Deciduous broadleaf trees	175	5
Needle-leaf trees	500	5
Tundra	80	1
Desert	250	0.5

**Figure 4.2:** The reaction of r_c to water vapour deficit Δq according to different schemes for the observed range of Δq . The reactions by dRH99 and by BB97 were defined for the same grass area (Cabauw, the Netherlands), and are therefore both calculated by $r_c \text{LAI} / r_{s,\min}$ ($\text{LAI} = 2$, $r_{s,\min} = 110 \text{ s m}^{-1}$, being representative for Cabauw).

which leads to large deviations for dry air conditions ($\Delta q > 10 \text{ g kg}^{-1}$). This is probably caused by the fact that they tested their scheme only for a Dutch grassland (Cabauw), where Δq typically ranges between 5 and 11 g kg^{-1} .

Given the above limitations, we replace the representation by dRH99 by a function that is also applicable for other locations and land use types (e.g. a function with a small r_c for very humid conditions and a weak dependence on Δq). We however found that r_c calculated from the water vapour deficit dependency as in Noah, HTESSEL and Aqs, is very different from r_c derived from measurements via the inverted

Penman-Monteith equation. Namely, the values obtained with Noah, HTESSEL, and Ags all stay within a very short range around $r_{s,\min}/LAI$. The function of BB97 is a nice integration between a small offset and a weak slope of the response functions. In our scheme, we use Equation 4.3, omitting f_θ (see Appendix A), and we replace the scaling factor 25.9 by $0.47r_{s,\min}/LAI$ (which equals 25.9 for $LAI = 2$ and $r_{s,\min} = 110\text{s m}^{-1}$, being representative for Cabauw). In this study, we define our scaling factor of 0.47 as f_r .

To estimate incoming longwave radiation, dRH99 use an expression given by Paltridge and Platt (1976), where L_{in} depends on the apparent emissivity of the atmosphere, the fractions of low and high clouds, and two empirical cloud coefficients. To avoid the dependence on low and high cloud information, we use relations described in Idso (1981) for clear skies, and Crawford and Duchon (1999) for cloudy skies, which depend on the total cloud cover only (as detailed in Appendix A). We also slightly adapted the albedo calculation of dRH99, such that it does not depend on the fraction of diffuse radiation, but on the total cloud cover fraction.

4.2.2 Estimation of temperature, humidity and joint structure parameters from surface fluxes

Based on Monin-Obukhov similarity theory, structure parameters have been estimated from surface fluxes by among others Wyngaard et al. (1971), Andreas (1988), Hill (1992), Thiermann and Grassl (1992), De Bruin et al. (1993), and Li et al. (2012). Maronga (2013) found, from a Large Eddy Simulation for resolving surface layer turbulence (vertical resolution of 2 m, horizontal resolution of 4 m), that the functions derived for C_{T^2} follow Monin-Obukhov similarity theory, while the functions for C_{q^2} are very sensitive to entrainment and not universal. Deviations from Monin-Obukhov similarity theory for variances were quantified by van de Boer et al. (2014a). Here we use the universal functions for the structure parameters of temperature and humidity, for unstable conditions presented by Li et al. (2012). They calculate the structure parameters from the surface fluxes via the temperature and humidity scales T_* and q_* (Equation 4A.4d in Appendix A):

$$\frac{(\kappa z)^{2/3} C_{T^2}}{T_*^2} = 6.7 \kappa^{2/3} \left(1 - 14.9 \frac{z}{L}\right)^{-2/3}, \quad (4.4a)$$

$$\frac{(\kappa z)^{2/3} C_{q^2}}{q_*^2} = 3.5 \kappa^{2/3} \left(1 - 4.5 \frac{z}{L}\right)^{-2/3}. \quad (4.4b)$$

In these equations, κ is the von Kármán constant with a value of 0.4. z is the height above the canopy, that depends on the measurement height z_m and the displacement height d following $z = z_m - d$, where d is estimated as $\frac{2}{3}z_c$ (z_c is the canopy height). L is the Obukhov length defined by Obukhov (1946) as a function of surface friction and buoyancy (see Appendix A).

For homogeneous turbulence, the joint structure parameter C_{Tq} can be estimated from the temperature and humidity structure parameters following Moene (2003):

$$C_{Tq} = r_{Tq} \sqrt{C_{T^2} C_{q^2}}, \quad (4.4c)$$

where r_{Tq} is the correlation coefficient between temperature and humidity. C_{Tq} has the value of the joint structure function in the inertial subrange, assuming that r_{Tq} is similar for all scales within the inertial subrange.

The step from surface fluxes to C_{T^2} and C_{q^2} introduces uncertainty in our C_{n^2} -scheme, because Monin-Obukhov similarity theory is not always valid (van de Boer et al., 2014a). Also, the step from C_{T^2} and C_{q^2} to C_{Tq} introduces uncertainty, because an estimate of r_{Tq} has to be made.

4.2.3 Estimation of C_{n^2} from temperature, humidity and joint structure parameters

The relationship between the structure parameter of the refractive index of air n , and the temperature, humidity and joint structure parameter is given by Hill and Clifford (1978) as

$$C_{n^2} = \frac{A_{T^2}}{\bar{T}_a^2} C_{T^2} + \frac{A_{q^2}}{\bar{q}^2} C_{q^2} + 2 \frac{A_T A_q}{\bar{T}_a \bar{q}} C_{Tq}, \quad (4.5a)$$

where A_T and A_q depend mainly on pressure, air temperature and specific humidity and the wavelength. Note that, although historically absolute humidity is used in the definitions of A_T and A_q , here we will follow Ward et al. (2013) and use specific humidity. Functions for A_T and A_q are given by Ward et al. (2013) as

$$A_T = -\frac{\bar{p}}{\bar{T}_a} \left(b_1 + \frac{b_2 \bar{q} R_v}{\bar{R}} \right), \quad (4.5b)$$

and

$$A_q = -\frac{\bar{p}}{\bar{T}_a} \frac{b_{q2} \bar{q} R_v}{\bar{R}} \left(1 - \frac{\bar{q} (R_v - R_d)}{\bar{R}} \right), \quad (4.5c)$$

where R is the universal gas constant ($8.314 \text{ J K}^{-1} \text{ mol}^{-1}$). The wavelength dependency of A_T and A_q is captured by the coefficients b_1 and b_2 (see Appendix B).

4.3 Data

In the first part of this section we describe the three measurement sites, specifications on instrumentation and vegetation, and the available data that we used to test our scheme. An overview of the measurements used for input or validation is given per site in Table 4.2. We choose to test our scheme for two vegetation types (grass 'G' and wheat 'W'), and two climatic regions (central 'C' and southern Europe 'S').

The names of the sites are: Haarweg (GC), Lannemezan (GS) and Merken (WC). In the second part of this section, we explain our data processing and selection.

4.3.1 Datasets

Haarweg: GC

The weather station at the Haarweg (<http://www.met.wau.nl/haarwegdata>) in Wageningen (the Netherlands, 7 m a.s.l.), an agrometeorological station, provided all four radiation components and the soil heat flux (7.5 cm below ground level). In 2005, additionally, fluxes of sensible and latent heat were measured using an eddy-covariance (EC) station (3.2 m above ground level, a.g.l.). Over the year, the grassland was mowed frequently to keep $z_c \approx 10$ cm. The soil at the Haarweg site contains clay and is rich in organic matter. We used data from the period 1 April to 30 September in 2005.

Merken: WC

Surface energy components were measured during the FLUXPAT campaign near Merken (Germany, 114 m a.s.l.) in the summer of 2009. This campaign was organized to study the soil-vegetation atmosphere system (see e.g. Graf et al. (2010) and van de Boer et al. (2013) for details). A station with an EC system (see Table 4.2 for details) at 2.4 m a.g.l. was installed in the middle of a flat winter wheat field. The four radiation components were measured at 1.7 m a.g.l., and the soil heat flux at 7.5 cm depth. The site contains a bouldered silt-loam soil. From 4 June on, the weight of green plant matter decreased, which we specified as the start of the ripening process. Data from 15 April to 3 June (DOY 104-154) were considered as the growing phase of the wheat, and data from 4 June to 27 July (DOY 155-208) as the ripening phase. The height of the wheat was between 55 and 85 cm, depending on the growth-state. The canopy height was 75 cm at the start of the ripening period (see Table 4.3).

Lannemezan: GS

The BLLAST campaign (Boundary Layer Late Afternoon and Sunset Turbulence) took place near the Pyrenees in southern France (582 m a.s.l.) from 14 June to 8 July 2011 (Lothon et al., 2012). The main objective of this campaign was to better understand the physical processes that control and follow from the transition of a convective boundary layer towards a stratified nocturnal boundary layer. Surface and boundary-layer measurements were performed around Lannemezan, a village located on a large plateau (200 km²) with several mainly agricultural land use types on a sandy loamy soil. An EC station was installed in a grass field, equipped with sensors for the main surface energy components: sensible and latent heat flux (2.55 m a.g.l.),

4.3. DATA

Table 4.2: Instrumentation specifications per input or validation variable for the three measurement sites

Instrument	Var	Inp	Valid	Haarweg	Merken, Lannemezan
Son. anemom.	T_a	x		CSAT3, Campb. Sci.	CSAT3, Campb. Sci.
	u	x			
	u_*		x		
	H		x		
	C_T^2		x		
Gas analyser	q	x		LI-7500, Li-cor	LI-7500, Li-cor
	$L_v E$		x		
	C_q^2		x		
Pyranometer	S_{in}	x		CM11, Kipp & Z.	CNR1, Kipp & Z.
	S_{out}		x		
Pyrgeometer	L_{in}		x	CG1, Kipp & Z.	CNR1, Kipp & Z.
	L_{out}		x		
Barometer	p	x		PTB101B, Vaisala	PTB101B, Vaisala
Soil heat plate	G		x	Thermopile, TNO	HFP01SC, Hukseflux

Table 4.3: Land-surface input variables per dataset. z_m is the height above ground of the heat flux observations, and z_c is the vegetation height.

Variable	GC	WC grow	WC ripe	GS
z_c (m)	0.1	*	0.85	0.25
z_m (m)	3.18	2.44	2.44	2.55
LAI ($m^2 m^{-2}$)	2	6	5	2
$r_{s,min}$ ($s m^{-1}$)	110	180	180	110
LAT	51°58'N	50°50'N	50°50'N	43°07'N
LON	5°38'E	6°24'E	6°24'E	0°21'E

$$* 0.1 + 0.65 \frac{DOY-105}{50}$$

incoming and outgoing shortwave and longwave radiation (1.68 m a.g.l.), and soil heat flux (3 cm below ground level), see Table 4.2 for details. The grass was cut before the installation, and grew throughout the campaign reaching 35 cm at the end of the campaign.

4.3.2 Data processing and selection

We first determined averages of temperature, specific humidity, wind speed, atmospheric stability, friction velocity and sensible and latent heat fluxes from the 20 Hz EC-data using the software ECPack-2.5.23-1.3 (van Dijk et al., 2004) for every measurement site. The averaging time was 30 minutes, which adequately captures surface-layer turbulence and excludes mesoscale processes. We performed a planar fit rotation (Wilczak et al., 2001) where the rotation angles were determined over a period of 7 days to adjust the coordinate system. Linear trends were removed and

Table 4.4: Land-surface input variables used for all sites (kept constant in our study although they can be site dependent). The albedos a_{\max} , a_{\min} , and a_{cloud} are used for shortwave radiation calculations in 4A.2b, and ϵ_s is the surface emissivity used for longwave radiation calculations. A_g determines the heat transfer between the vegetation top and the soil in $W m^{-2} K^{-1}$.

Variable	a_{\max}	a_{\min}	a_{cloud}	ϵ_s	A_g	r_{Tq}
Value	0.3	0.17	0.21	0.96	5	0.6

the Webb-correction (Webb et al., 1980) was applied to correct humidity fluctuations for density fluctuations induced by temperature fluctuations. The sonic temperature was corrected for humidity effects using the Schotanus correction (Schotanus et al., 1983). 95% confidence intervals were estimated by quantifying the sampling error for each scalar average and flux, following van Dijk et al. (2004).

Incoming and outgoing shortwave and longwave radiation, soil heat flux, and pressure measurements were averaged from 1-minute to 30-minute data. We used fixed upper and lower plausible limits for the radiation and flux components, and a storage term was added to the soil heat flux using the calorimetric method (Rouse, 1984), applying a volumetric soil heat capacity of $2.2 \times 10^6 J m^{-3} K^{-1}$ for all three sites (assuming that the contributions of sand, clay, organic matter, water and air are similar at the sites). Because the sum of observed H and L_v is generally lower than the observed available energy, we adjusted the sensible and latent heat fluxes to the total available energy ($Q_n - G$), while maintaining the value of the Bowen ratio ($H/L_v E$) following Twine et al. (2000).

We also used the ECpack software to obtain structure parameters of T_α , q , and their joint structure parameter based on the structure function and a separation of 0.9 m. We applied a constant path-averaging-factor of 1.12 to correct the structure parameters for the sonic anemometer measurement that originates from a finite path (0.12 m) instead of one point Kooijmans (2013). Furthermore, we applied a correction on the structure parameters obtained by ECpack (Equation 5 in Braam et al. (2012)) to improve the conversion from time to space (for a non-constant wind speed U) that is needed for the structure function following Bosveld et al. (1998). They derived this correction factor for the structure parameters from Wyngaard and Clifford (1977), who only determined it for $\frac{\sigma_y^2}{U^2} < 0.1$. If our data exceeded this limit, we applied a correction of $\frac{95}{90}$ (Equation 5 in Braam et al. (2012) for $\frac{\sigma_y^2}{U^2} = 0.1$). To obtain C_{n^2} from the calculated structure parameters, we used the expressions of Ward et al. (2013) described in Section 4.2.3. The observed correlation coefficient between T and q in Equation 4.4c was taken from ECpack output. We calculated C_{n^2} for an optical wavelength ($\lambda = 670$ nm) and for a millimetre wavelength ($\lambda = 2$ mm).

We selected daytime data between 10 and 15 UTC and eliminated stable situations by excluding data with $z/L > -0.02$, because the flux estimating part of our scheme might have difficulties if the surface fluxes are very small. We also excluded

rainy days from the data, because wet sonic anemometers and gas analysers introduce errors. Furthermore, turbulence in the lowest part of the atmosphere is very weak on rainy days. For GC, we removed 36 days such that 148 days remained. We also excluded rainy days for WC, such that 38 days were left for the growing period, and 30 days for the ripening period. For the grass data in Southern France, we excluded 6 days (DOY 167, 169, 173, 174, 180 and 185) at which rain events were observed (17 days remained).

4.4 Estimates and validation

From the 30-minute daytime data of T_a , q , p , u and S_{in} , we calculated the sensible, latent and soil heat fluxes, and the radiation components from the first step in our scheme as discussed in Section 4.2.1, following the parametrizations given in Appendix A. The required land surface characteristics that differ per measurement site are given in Table 4.3. Table 4.4 contains the constants in our scheme. These values can be made site dependent, however, our aim here is to present an easy to use scheme that performs reasonably at several locations.

The iteration loop for the energy balance components (Equation 4A.3c – 4A.4e) is initiated with neutral conditions, and is stopped when the sensible heat flux converged within 1 Wm^{-2} , or when the calculation needs > 10 iterations (3 iterations are usually enough). From the estimated values for z/L , H , $L_v E$, and u_* that follow from the iterations (also when forced to stop), we calculated the structure parameters C_{T^2} , C_{q^2} and C_{Tq} following the theory described in Section 4.2.2. In contrast to the derivation from observations (Section 4.3.2), we applied a fixed r_{Tq} of 0.6 in the scheme. We derived C_{n^2} for $\lambda = 670 \text{ nm}$ and $\lambda = 2 \text{ mm}$ via Equation 4.5.

We validated our estimates of the radiation components, fluxes and structure parameters with the values directly obtained by radiation and EC measurements. We also validate the key parameters of the first part of our scheme: T_s , r_a and r_c . These parameters are however not directly measured. To compare the estimated surface temperature T_s with measurements, we calculated the *measured* T_s using

$$T_s = \left(\frac{L_{out} - (1 - \epsilon_s)L_{in}}{\epsilon_s \sigma} \right)^{1/4} \quad (4.6)$$

in which we also used 0.96 for the surface emissivity ϵ_s , and $5.67 \times 10^{-8} \text{ Wm}^{-2}\text{K}^{-4}$ for the Stefan Boltzman constant σ . The *measured* resistances were calculated following

$$r_a = -\rho c_p \frac{T_a - T_s}{H}, \quad (4.7)$$

and

$$r_c = r_a \left(\frac{s(Q_n - G) + \frac{\rho c_p (e_{sat} - e_a)}{r_a}}{\gamma L_v E} - \frac{s}{\gamma} - 1 \right), \quad (4.8)$$

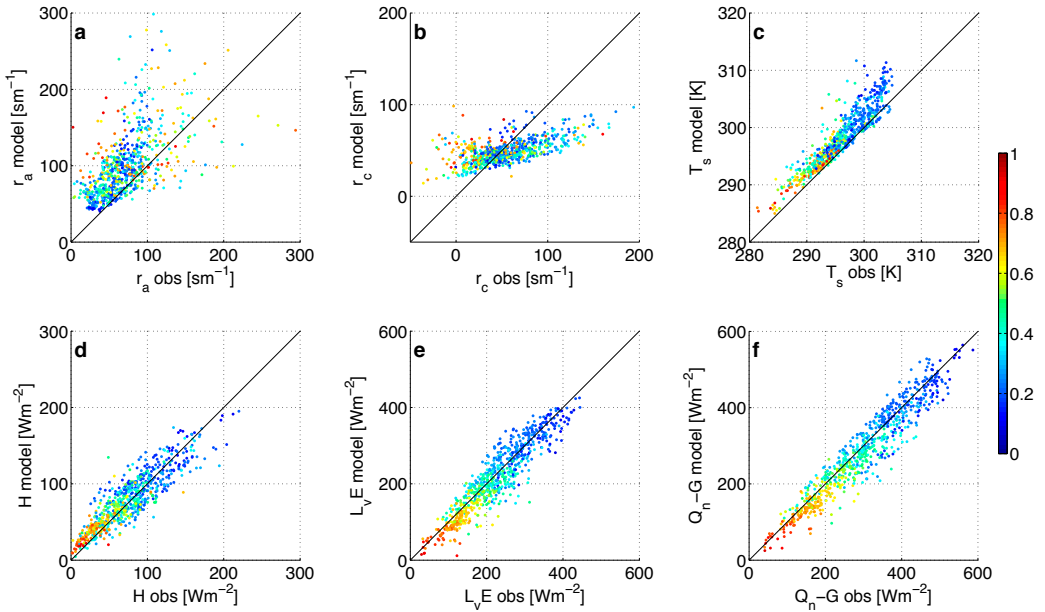


Figure 4.3: Validation of estimated estimates of r_α , r_c , T_s , H , $L_v E$, and $Q_n - G$ with measurements at a grass field in the Netherlands (GC) in 2005. Blue markers indicate clear-sky conditions, whereas red markers indicate very cloudy conditions.

which is an inverted form of the Penman-Monteith equation (Equation 4.1).

We calculated regression fits per variable (*var*) for the four datasets, using orthogonal distance regression. The offset was set to zero, and the slope was calculated, including its standard deviation. For this regression, we excluded outliers that we defined as data for which the shortest distance to the linear fit (i.e. perpendicular to the regression line) was larger than 3 times the average of these distances. We calculated new regressions until the slope changed by < 0.3 . We normalized the RMSE by dividing by the mean observed value of the specific variable to obtain the NRMSE to compare multiple regressions of different variables.

We tested the agreement of the datasets with Monin-Obukhov similarity theory by calculating the parameters in the similarity functions for the structure parameters as follows: we kept the second parameter c_2 in Eqs 4.4a and 4.4b constant (14.9 for T , 4.5 for q), and fitted the data to a regression with the prescribed shape of $y = c_1 (1 - c_2 x)^{-2/3}$. The structure parameter and stability data were weighted using the inverse of the confidence intervals for C_{T^2} , C_{q^2} , and z/L (via the intervals of u_* , T_α , q , $\overline{w'T'}$ and $\overline{w'q'}$) that were calculated by ECPack.

4.5 Results

We here discuss the results in the same steps and order as we described our scheme; first the estimation of fluxes from weather data, then the estimation of temperature

4.5. RESULTS

Table 4.5: Regression results of estimated versus observed fluxes, structure parameters and variables at the Haarweg (GC, left) and in Lannemezan (GS, right). Indicated with 'MO' are regression results using adapted Monin-Obukhov parameters for the scheme.

Var	GC			GS		
	Slope	NRMSE	n	Slope	NRMSE	n
H	0.98 ± 0.01	0.04	708	0.83 ± 0.02	0.09	108
$L_V E$	1.00 ± 0.00	0.02	707	0.95 ± 0.01	0.01	108
G	0.85 ± 0.01	0.23	714	0.89 ± 0.03	0.13	112
Q_n	0.98 ± 0.00	0.00	710	0.92 ± 0.00	0.01	112
u_*	0.85 ± 0.01	0.07	713	0.93 ± 0.02	0.06	112
r_c	0.77 ± 0.01	0.35	705	0.74 ± 0.03	0.29	105
r_a	1.25 ± 0.02	0.14	704	1.73 ± 0.06	0.23	109
$T_s - T_a$	1.40 ± 0.01	0.13	714	1.36 ± 0.03	0.11	112
L_{in}	0.98 ± 0.00	0.00	713	0.88 ± 0.00	0.02	112
L_{out}	1.02 ± 0.00	0.00	714	1.02 ± 0.00	0.00	112
C_{T^2}	1.18 ± 0.02	0.12	709	1.58 ± 0.06	0.22	112
C_{q^2}	1.32 ± 0.01	0.12	712	2.58 ± 0.06	0.39	112
C_{Tq}	1.23 ± 0.01	0.09	707	2.43 ± 0.07	0.37	112
$C_{n^2\lambda_{670nm}}$	1.16 ± 0.02	0.12	702	1.51 ± 0.06	0.21	112
$C_{n^2\lambda_{2mm}}$	1.31 ± 0.01	0.11	713	2.54 ± 0.05	0.38	112
$C_{T^2}MO$				1.08 ± 0.04	0.14	112
$C_{q^2}MO$				1.76 ± 0.04	0.21	112
$C_{Tq}MO$				1.67 ± 0.05	0.20	112
$C_{n^2\lambda_{670nm}}MO$				1.03 ± 0.04	0.15	112
$C_{n^2\lambda_{2mm}}MO$				1.73 ± 0.04	0.20	112

and humidity structure parameters from fluxes, and finally the estimation of C_{n^2} . The difference between the surface temperature T_s and air temperature T_a is very important for the calculation of the energy that is available for H and $L_V E$. This difference is however overestimated for all four datasets (see the regression fits and errors for all datasets in Table 4.5 and 4.6, and for GC Figure 4.3c). Despite the overestimation of this difference, and thus of T_s , the longwave radiation components are estimated fairly well for all datasets. Thereby, Q_n estimates fit the observations with a general underestimation of 2-8% (see also Figure 4.3f for GC). For GS, this is caused by an underestimated incoming longwave radiation. The surface reflectance of shortwave radiation (albedo) is however underestimated for all sites (not shown). G is estimated well for the Haarweg (GC) and Lannemezan (GS) dataset, whereas for both Merken datasets (WC), G is underestimated. However, its value is very low compared to Q_n such that this underestimation does not produce large errors for the energy that is available for H and $L_V E$.

r_c estimates are much lower than the values we derived from observations using the inverted Penman Monteith approach (Equation 4.8) for all datasets. However, we

Table 4.6: Regression results of estimated versus observed fluxes, structure parameters and variables during the growing (left) and ripening (right) season in Merken (WC).

Var	WC Growing			WC Ripening		
	Slope	NRMSE	n	Slope	NRMSE	n
H	1.54 ± 0.05	0.15	47	1.15 ± 0.03	0.11	154
$L_V E$	0.87 ± 0.03	0.08	47	1.00 ± 0.02	0.08	162
G	0.53 ± 0.03	0.86	47	0.60 ± 0.02	0.66	168
Q_n	0.93 ± 0.02	0.02	50	0.97 ± 0.01	0.01	167
u_*	1.04 ± 0.02	0.02	50	1.23 ± 0.01	0.05	167
r_c	0.56 ± 0.17	1.63	24	0.27 ± 0.04	3.30	146
r_a	1.08 ± 0.13	0.24	19	0.08 ± 0.03	5.51	162
$T_s - T_a$	1.77 ± 0.17	0.30	28	1.27 ± 0.08	0.48	168
L_{in}	1.03 ± 0.01	0.00	28	1.01 ± 0.00	0.00	168
L_{out}	1.01 ± 0.00	0.00	28	1.00 ± 0.00	0.00	168
C_{T^2}	3.29 ± 0.27	0.53	50	1.35 ± 0.09	0.53	157
C_{q^2}	1.08 ± 0.05	0.12	50	1.42 ± 0.05	0.22	166
C_{Tq}	2.39 ± 0.18	0.41	50	1.74 ± 0.09	0.38	168
$C_{n^2 \lambda_{670nm}}$	3.37 ± 0.28	0.54	50	1.27 ± 0.09	0.58	157
$C_{n^2 \lambda_{2mm}}$	1.22 ± 0.06	0.13	50	1.47 ± 0.05	0.23	167

did not validate our estimated r_c with direct observations, and thus the presented underestimation of r_c is uncertain. A high NRMSE was calculated for the regression of r_c . Nevertheless, the partitioning of the available energy into H and $L_V E$ is appropriate for GC and GS, which indicates that r_c is of the correct order of magnitude. For WC, H is generally overestimated, and $L_V E$ is slightly underestimated. However, the estimations of all variables are quite scattered for the growing phase of the WC dataset (see the standard deviations and NRMSE values given in the first columns in Table 4.6. This is not surprising, because we use several fixed values to describe the vegetation (e.g. LAI , a , surface roughness z_{0m} , d) whereas the vegetation develops in time. Furthermore, this is by far the smallest dataset we used (partly because of the stability criterion). r_a estimates are quite scattered, however, most of the data used here is in a r_c -regime in which the fluxes are not very sensitive to r_a , see Jacobs and De Bruin (1992).

Although H and $L_V E$ are predicted well for GC, C_{T^2} and C_{q^2} and thereby C_{Tq} are overestimated. For the growing wheat (WC), H is largely overestimated, which leads to a clear overestimation of C_{T^2} as expected from the relation between H^2 (or T_*^2) and C_{T^2} given in Equation 4.4a. For GS, the regression slopes for H and $L_V E$ are quite satisfying around 1.0, whereas the slopes for C_{T^2} and C_{q^2} are both more than twice as large. This is not expected from the relation between the slopes of H^2 and C_{T^2} as mentioned above. We think that this is partly related to the Monin-Obukhov parameters used for this relation. We determined the similarity relationships (Equations 4.4a and 4.4b) for GS where we kept c_2 to its literature values of 14.9 for tempera-

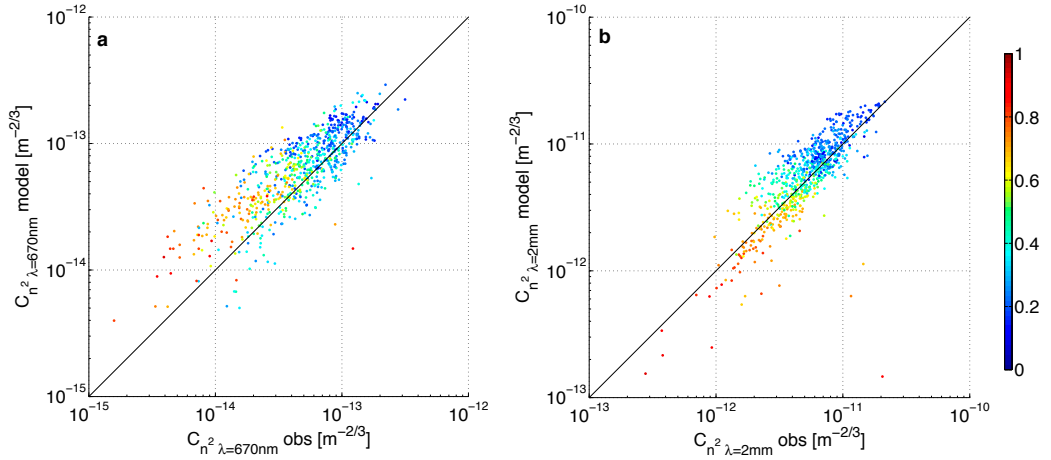


Figure 4.4: Validation of estimates of the structure parameters of n for an optical (a) and a millimetre wavelength (b), with derivations from measurements at a grass field in the Netherlands in 2005. Blue markers indicate clear-sky conditions, whereas red markers indicate very cloudy conditions.

ture and 4.5 for humidity. The obtained values for c_1 deviate largest for the GS data, for both temperature and humidity (4.7 and 2.4 respectively, compared to the coefficients we took from Li et al. (2012) as 6.7 and 3.5). The coefficients for the other datasets agree better with Li et al. (2012), with 6.8 and 3.9 for GC, 6.9 and 3.9 for the growing phase of the wheat (WC), and 6.4 and 3.4 for the ripening phase (WC). If we use the newly obtained coefficients for GS (4.7 and 2.4 for temperature and humidity respectively), we obtain improved regression slopes (indicated with MO in Table 4.5). However, C_{q^2} is still overestimated (albeit with a large NRMSE) while the estimation of $L_V E$ is close to perfect with a very low NRMSE. The large NRMSE for C_{q^2} is probably caused by the fact that at GS, humidity fluctuations were smaller than at GC and WC, and therefore more sensitive to instrumental errors.

The estimates of C_{T^2} , C_{q^2} and C_{Tq} lead to reasonable estimates of C_{n^2} , see Tables 4.5 and 4.6 and Figures 4.4 and 4.6. Note that the structure parameters occur in a large range (mind the logarithmic scale in the figures, and hence a slope of 2 should be interpreted as an error of much less than an order of magnitude. For GS, we see the overestimation of C_{q^2} again in the estimate for C_{n^2} for $\lambda = 2\text{mm}$ because at this wavelength, scintillations are more sensitive to humidity fluctuations than at nanometre wavelengths. For the growing season in Merken, we find the opposite. The large uncertainty of C_{T^2} for the data of both the growing and ripening phase leads to an overestimation of C_{n^2} for $\lambda = 670\text{nm}$, a wavelength at which C_{n^2} is more sensitive to temperature fluctuations.

As an example of the possible application of our scheme, we show in Figure 4.7 the performance of our scheme for a sunny and cloudy day at the Haarweg (GC). The scheme estimates the turbulence at the cloudy day very well, and for the clear sky day there is a slight overestimation. It can be seen that for the optical wave-

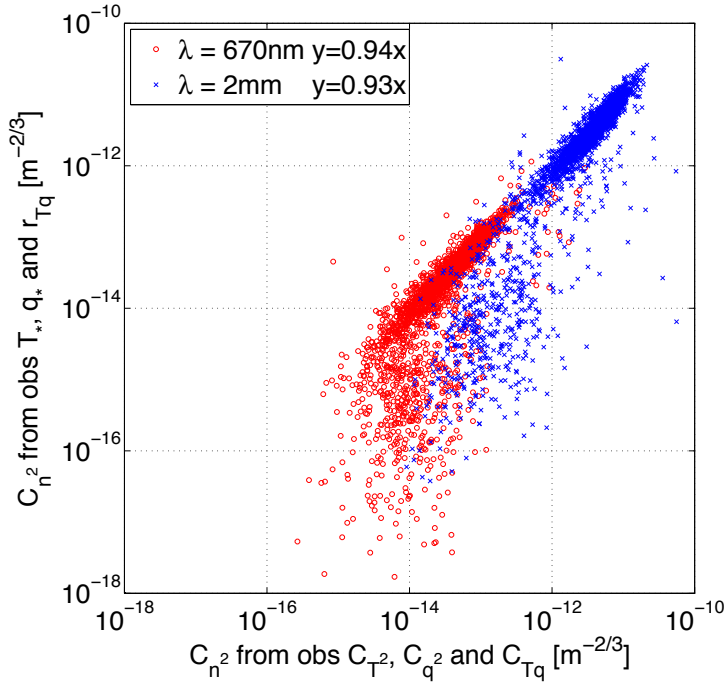


Figure 4.5: Validation of derivations of C_{n^2} from measured values for C_{T^2} , C_{q^2} , C_{Tq} and r_{Tq} , with derivations from flux measurements (T_* and q_*) at a grass field in the Netherlands in 2005. Red markers indicate an optical wavelength, blue markers indicate a millimetre wavelength.

length, scintillation values are highest around noon, decrease until sunset and increase again towards midnight. On the other hand, for the millimetre wavelength the scintillations decrease to zero in the night. Cloudy conditions weaken the scintillations, especially for the millimetre wavelength that is more sensitive to humidity fluctuations. For this case, our method performs better for $\lambda = 2\text{mm}$ than for $\lambda = 670\text{nm}$, because humidity fluctuations are larger and better defined.

4.6 Discussion

We developed a method to estimate C_{n^2} from single-level weather data that consists of three steps:

- a From single-level weather data to surface fluxes
- b From surface fluxes to structure parameters of temperature and humidity
- c From structure parameters to C_{n^2}

For step a, we applied an existing scheme of dRH99 that was developed for a grass field in the Netherlands (Cabauw). We adjusted their scheme for other field conditions, and tested it for another grass field in the Netherlands, a grass field in

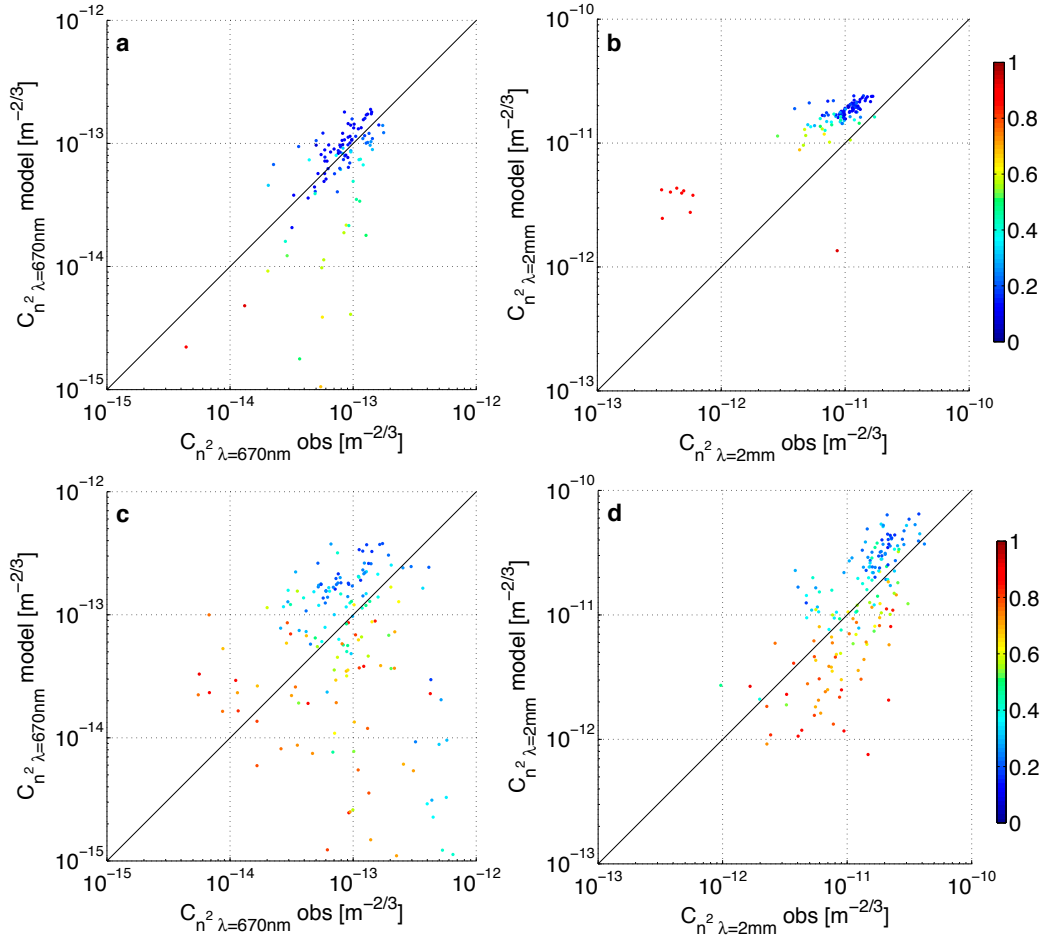


Figure 4.6: Validation of estimates of the structure parameters of n for an optical (a and c) and a millimetre wavelength (b and d), with derivations from measurements. Above: a grass field in southern France in 2011 for adjusted Monin-Obukhov parameters. Below: a wheat field in the ripening phase in western Germany in 2009. Blue markers indicate clear-sky conditions, whereas red markers indicate very cloudy conditions.

southern France, and a wheat field in western Germany. This scheme is based on the Penman-Monteith equation, which is an appropriate description of the process of transpiration. But this only holds provided that it is used with observations from the location of interest; a different surface results in different temperature, humidity and wind observations.

In our scheme, we replaced the water vapour deficit dependency of r_c described by dRH99 as $r_c = 10^4 \Delta q$ by the approach of BB97. In Figure 4.8 we show the performance of the scheme for $L_V E$ and r_c if we use the water vapour deficit dependency described by dRH99. When comparing these results with the results presented in Figure 4.3b and e, we see that the estimation of the latent heat flux is improved especially for dry air conditions by applying the water vapour deficit and global ra-

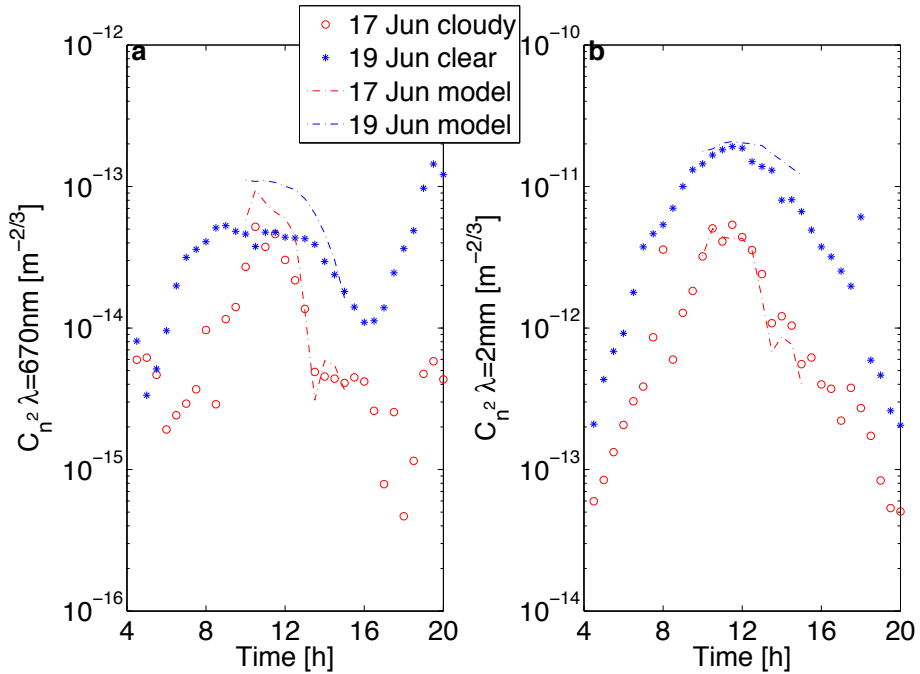


Figure 4.7: C_n^2 measured (markers) and estimated (lines) for a clear (red) and cloudy (blue) summer day (19 June 12 UTC, 2005) at the Haarweg (similar to Figure 4.1).

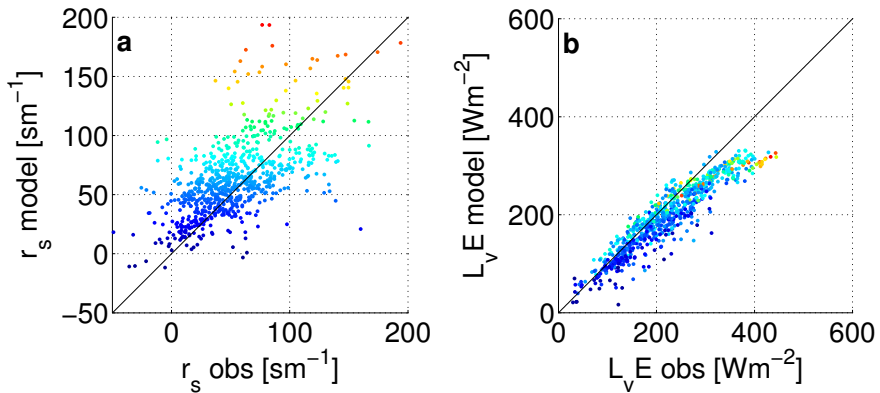


Figure 4.8: r_c and L_{VE} for the Haarweg (GC) using the approach for r_c from dRH99, coloured by Δq (blue is 0, red is 20 g kg^{-1}).

diation dependency of BB97. This result agrees with Figure 4.2, in which we see that the approach of dRH99 differs from the other approaches mainly for dry air conditions.

To investigate which parameters and constants have the largest influence on the derived C_n^2 , we performed a sensitivity analysis. In Table 4.7 we list the parameters of step a, and show for one midday summer situation the relative increase of

C_{n^2} for a realistic increase of the parameters. We see that the dependency on the parameters in f_{dq} are very strong. Furthermore, our scheme is very sensitive to the estimated LAI , canopy height and albedo. This indicates that for the first step of our method, a good estimate of the vegetation characteristics is the most crucial part. The increase of the parameters that lead to an increase or decrease of C_{n^2} for both wavelengths (e.g. N , a and A_g) are related to the available energy. If a certain increase leads to a decrease of C_{n^2} for one wavelength and an increase for the other wavelength, then the parameter is mainly related to the partitioning of energy between latent and sensible heat (e.g. LAI , $r_{s,min}$ and f_r).

Next to the values given for the HTESEL land-surface scheme, we tested our method with vegetation parameters from the Noah land-surface model (not shown). However, the flux and structure parameter validation results are much worse using values from Noah. It seems that the definition of LAI and $r_{s,min}$ cannot be separated from their appearance in the land-surface schemes. We did not implement the dependency of r_c on the type of carbon fixation the vegetation uses (C3 or C4). Adding such a plant-physiological process requires a clear separation between transpiration and evaporation processes. If C_{n^2} estimates are needed for partly wet vegetated surfaces, our method is empirically solid. However, we actually need a more realistic treatment to capture interception and soil evaporation. For that, a SVAT (soil vegetation atmosphere) could be used.

In step b, the uncertainties in the scheme are the validity of Monin-Obukhov similarity theory, and the value for r_{Tq} . In Figure 4.5 we show that even if measured fluxes (scaled as T_* and q_*) are used, the estimates of C_{n^2} are still quite scattered. Comparing Figure 4.4 with 4.5 (in which both wavelengths are presented in the same figure), we see that the scatter partly introduced by the flux estimation is only slightly larger than the scatter solely caused by the calculation of C_{n^2} from fluxes. Values for C_{n^2} calculated from measured fluxes using Monin-Obukhov similarity theory are somewhat smaller than C_{n^2} values derived from the observed structure parameters of T_a and q . This holds for both wavelengths for this data (GC), which indicates that here, the Monin-Obukhov similarity functions for both temperature and humidity should have a slightly larger c_1 or smaller c_2 (see Equation 4.4a and 4.4b). In the previous section we wrote that, indeed, we found a slightly larger value for c_1 for T_a and q for the GC data.

We found that for the GS dataset, we should certainly change the coefficients in the Monin-Obukhov relations. In the previous section, we calculated c_1 that fitted the data with a c_2 that was kept constant. However, we would like to point out that if we fit the GS data to the function without keeping c_2 , we get for temperature $c_1 = 4.2$ and $c_2 = 10.8$, and for humidity $c_1 = 2.5$ and $c_2 = 4.7$. These values are very unusual compared to reported values for several datasets Kooijmans (2013), especially for humidity.

Considering a fixed value for r_{Tq} , one would expect a value close to one because temperature and humidity are assumed to behave similar during daytime. However,

Table 4.7: Sensitivity estimates of C_{n^2} to the main input parameters and constants (or parameters directly derived from S_{in}) for 19 June 2005 12 UTC at the Haarweg.

Variable			Relative increment		
Name	Value	Unit	Input	$C_{n^2}\lambda = 670\text{nm}$	$C_{n^2}\lambda = 2\text{mm}$
LAI	2	$\text{m}^2 \text{m}^{-2}$	0.50^1	-0.16	0.17
$r_{s,\min}$	110	s m^{-1}	-0.10^2	-0.05	0.06
f_r	0.47	-	0.50^3	0.23	-0.20
h_s	160	$(\text{kg kg}^{-1})^{-1}$	-0.20^4	-0.06	0.07
Δq_0	0.003	kg kg^{-1}	2.00^5	-0.08	0.10
z_c	0.1	m	-0.80^6	-0.12	-0.17
A_g	5	$\text{W m}^{-2} \text{K}^{-1}$	2.00^7	-0.26	-0.08
z_{0h}/z_{0m}	0.1	-	-0.60^8	-0.04	-0.07
ϵ_s	0.96	-	0.02^9	-0.04	0.02
N	0.17	-	2.60^{10}	0.12	0.04
α	0.19	-	1.60^{11}	-0.32	-0.13

¹Reported LAI values for grassland vary between 0.5 and 3 (HTESSSEL).

²Reported $r_{s,\min}$ values for grassland vary between 100 and 110 s m^{-1} (HTESSSEL).

³The factor 25.9 s m^{-1} in BB97 is the optimal $r_{s,\min}$ for the best of their two tested Penman-Monteith schemes. The optimal factor for their other scheme is 39.2 s m^{-1} , which would result in a factor of $39.2 \frac{LAI}{r_{s,\min}} = 0.71$ for our approach.

⁴The optimum h_s of 160 $(\text{kg kg}^{-1})^{-1}$ was found by BB97. Land-surface models use a type of h_s that differs between 40-50 $(\text{kg kg}^{-1})^{-1}$. Assuming the same relative range, our h_s would maximum range between 130-190 $(\text{kg kg}^{-1})^{-1}$ (an increment of 0.20 leads to reversed values).

⁵From figure 14b in BB97 we derived that this value should be between 0.003 and 0.006 kg kg^{-1} .

⁶ ϵ_s varies between 0.95 and 0.98 for all kinds of crops, forest and bare soils.

⁷The height of maintained grassland is between 2 and 10 cm.

⁸In HTESSSEL, A_g doubles between low and high vegetation.

⁹Betts and Beljaars (1993) found a ratio for z_{0h}/z_{0m} between 12 and 26.

¹⁰The approaches by Kasten and Czeplak (1980) and Spena et al. (2010) give results within 0.11 and 0.44 for the estimation of the cloud cover for this case.

¹¹The maximum albedo given for this grassland is 0.3.

we found in our datasets that the daytime value differs from -1 to 1, with a median of ≈ 0.6 . It seems that our datasets suffered from non-local effects. This means that our assumption of a fixed r_{Tq} is actually not valid and introduces errors in the calculation of C_{Tq} and therefore also in C_{n^2} . We cannot omit this assumption when only weather data is available, because r_{Tq} cannot be derived from low frequency temperature and humidity data.

Step c is the most straightforward part of our method, because that part is based on physical theories. Only the dependency on the wavelength of interest influences the performance of our method. For the tested datasets, our method generally performs better for $\lambda = 670\text{nm}$ than for $\lambda = 2\text{mm}$. Note that a more elaborated C_{n^2} model would also include the scattering effect of aerosols on the wave propagation equation and thus on C_{n^2} .

4.7 Conclusions

A good estimation of the optical turbulence gives knowledge on the performance of communication and imaging systems. Often, weather data is available at only one level, precluding the use of methods based on vertical gradients (Sivasligil et al., 2013). Therefore, we here present an approach to estimate the structure parameter of the refractive index of air (C_{n^2}), based on single-level weather station data and Monin-Obukhov similarity theory. Our estimates of C_{n^2} are accurate enough to help in the development of systems based on the propagation of electromagnetic waves (e.g. radio wave communication and ground-based telescoping). Based on large time series of weather station data, the climatology of C_{n^2} for arbitrary wavelengths could be determined. For existing weather and imaging data, our estimates provide information on the quality of the images.

For a grass field in The Netherlands, the estimated values for C_{n^2} are in agreement with values derived directly from eddy covariance measurements. The results of a growing wheat field in western Germany contained more scatter than validation results from the Dutch and a French grass field, and the ripening phase of this wheat field, due to difficulties with the estimation of fixed land surface and vegetation input parameters. The scheme is most sensitive to the first part of the scheme; the estimation of surface fluxes from single-level weather data. Especially the parametrization of the canopy resistance is important, which differs per vegetation type and growing state. It determines the partitioning of energy between sensible and latent heat fluxes.

However, the scatter introduced by flux estimation uncertainties is only slightly larger than the scatter that is obtained when calculating C_{n^2} from observed surface fluxes. For the second step in which the structure parameters of temperature and humidity are estimated from surface fluxes, validity of Monin Obukhov similarity theory is of importance. For the grass field in southern France, we had to fit the Monin-Obukhov parameters to the data to obtain good validation results. In the third step, C_{n^2} is calculated from the structure parameters for one specific wavelength. For our datasets, estimated values for C_{n^2} agree slightly better with eddy covariance data for the optical wavelength than for the millimetre wavelength. The code for this application (MATLAB) can be obtained from the second author.

4A Appendices

4A.1 Appendix A; Scheme to estimate fluxes from weather data

First, our scheme that is adapted from dRH99 directly estimates air density ρ , air heat capacity $c_p (= 1004(1 + 0.84q))$, water vapour pressure e_a and saturated water vapour pressure e_{sat} (both in Pa) from air temperature (T_a), specific hu-

midity (q) and pressure (p). The slope of the saturated vapour pressure curve is $s(T) = de_{\text{sat}}/dT$, and the psychrometric constant is $\gamma = c_p \rho R_v / (L_v R_d)$, where R_d is the specific gas constant for dry air ($287 \text{ J kg}^{-1} \text{ K}^{-1}$), and R_v is the specific gas constant for water vapour ($462 \text{ J kg}^{-1} \text{ K}^{-1}$). The temperature dependency of e_{sat} , s and L_v can be found in Moene and van Dam (2014), page 355.

Secondly, the surface resistance is calculated following

$$r_c = f_r \frac{r_{s,\text{min}}}{LAI} f_{dq} f_{\text{rad}} \quad (4A.1a)$$

where the scaling factor $f_r = 0.47$, and f_{dq} is calculated following BB97:

$$f_{dq} = 1 + h_s (\Delta q - \Delta q_0), \quad (4A.1b)$$

in which Δq is the specific humidity deficit in kg kg^{-1} (calculated as $q_{\text{sat}} - q$), $h_s = 160 \text{ kg}^{-1} \text{ kg}$, $\Delta q_0 = 0.003 \text{ kg}^{-1} \text{ kg}$, and where

$$f_{\text{rad}} = \frac{1000 S_{\text{in}} + 230 (1000 - 2 S_{\text{in}})}{S_{\text{in}} (1000 - 230)}. \quad (4A.1c)$$

Thirdly, most of the radiation components can be calculated. Outgoing shortwave radiation (S_{out}) is calculated following

$$S_{\text{out}} = a S_{\text{in}}, \quad (4A.2a)$$

where a is the surface albedo that depends on the solar elevation angle α and the effective cloud cover fraction N as

$$a = a_{\text{max}} - (1 - N) \sin(\alpha) (a_{\text{max}} - a_{\text{min}}) - N (a_{\text{max}} - a_{\text{cloud}}). \quad (4A.2b)$$

a_{max} , a_{min} , and a_{cloud} are the surface albedo's for respectively a minimum solar elevation and a clear sky (the highest a), a maximum solar elevation and a clear sky (the lowest a), and a very cloudy sky. We calculated N as

$$N = \frac{\frac{S_{\text{in},0} - S_{\text{in}}}{S_{\text{in},0}} - 0.2}{0.8}, \quad (4A.2c)$$

where $S_{\text{in},0}$ is the solar constant I_0 ($\approx 1365 \text{ W}^2 \text{ m}^{-2}$) multiplied with the cosine of the zenith angle θ_z of the specific location and time and corrected for the orbital eccentricity via the difference in distance (d) to the sun,

$$S_{\text{in},0} = \bar{I}_0 \left(\frac{\bar{d}_{\text{sun}}}{d_{\text{sun}}} \right)^2 \cos \theta_z. \quad (4A.2d)$$

Incoming longwave (L) radiation is calculated as

$$L_{in} = \epsilon_a \sigma T_a^4, \quad (4A.2e)$$

where ϵ_a is the air emissivity, and σ is the Stefan Boltzmann constant (5.67×10^{-8}). We used the following expressions for the emissivity of air, adapted from Idso (1981)

$$\epsilon_{a,clear} = 0.63 + 5.95 \times 10^{-7} e_a e^{1500/T_a}, \quad (4A.2f)$$

and (Crawford and Duchon, 1999)

$$\epsilon_a = N + (1 - N) \epsilon_{a,clear}. \quad (4A.2g)$$

Fourthly, H is calculated from the energy balance equation, which we can write as

$$H = Q_{n,0} + Q_{n,T}(T_s - T_a) - G_0 - G_T(T_s - T_a) - L_v E_0 - L_v E_T(T_s - T_a), \quad (4A.3a)$$

where all energy terms consist of an isothermal term that is calculated using T_a instead of T_s (indicated with the subscript 0), and a correction term that corrects for that assumption of an isothermal atmosphere. This correction term therefore depends on $(T_s - T_a)$ (indicated with the subscript T). Thereby, the correction terms depend on H , via

$$T_s - T_a = \frac{H r_a}{\rho c_p}. \quad (4A.3b)$$

Because r_a depends on the atmospheric stability which is unknown, an iteration loop is needed to calculate H . Inserting the H -dependent correction terms in Equation 4A.3a results in

$$H = \frac{Q_{n,0} - G_0 - L_v E_0}{1 + Q_{n,T} + G_T + L_v E_T}, \quad (4A.3c)$$

where the isothermal terms are calculated following

$$Q_{n,0} = (1 - \alpha) S_{in} + (\epsilon_a - 1) \epsilon_e \sigma T_a^4, \quad (4A.3d)$$

$$G_0 = A_g (T_a - T_{24h}). \quad (4A.3e)$$

Here, A_g is the soil heat transfer coefficient, and T_{24h} is the temperature history of the last 24 h that represents the deep-soil temperature, and

$$L_v E_0 = \frac{\rho c_p}{\gamma} \frac{e_{sat} - e}{r_a + r_c}. \quad (4A.3f)$$

Note that $L_v E_0$ depends on r_a too, which means that the calculation of $L_v E_0$ is part of the iteration loop that is used for the calculation of H .

The correction terms are all part of the iteration loop, because via H , we introduced an r_a -dependency:

$$Q_{n,T} = \frac{r_a}{\rho c_p} \epsilon_s \sigma 4 T_a^3, \quad (4A.3g)$$

where ϵ_s is the surface emissivity,

$$G_T = \frac{r_a}{\rho c_p} A_g, \quad (4A.3h)$$

and

$$L_v E_T = \frac{r_a s(T_a)}{\gamma r_a + r_c}. \quad (4A.3i)$$

The loop starts with neutral conditions ($\Psi_T = \Psi_u = 0$) for a first estimate of the atmospheric-stability dependent r_a and u_* . The aerodynamic resistance is calculated as

$$r_a = \frac{1}{\kappa u_*} \left(\ln \frac{z}{z_{0h}} - \Psi_T \left(\frac{z}{L} \right) + \Psi_T \left(\frac{z_{0h}}{L} \right) \right). \quad (4A.4a)$$

κ is the von Kàrmàn constant (0.4), z the height ($z = z_m - d$, $d = \frac{2}{3} z_c$ is the displacement height), z_{0h} is the roughness length for heat, calculated as $0.1 z_{0m}$, the roughness length for momentum ($z_{0m} = 0.4 (z_c - d)$). Ψ_T is the Businger-Dyer integrated Monin-Obukhov flux profile relation function for temperature gradients as described in Paulson (1970). L is the Obukhov length calculated following Equation 4A.4c, and the friction velocity u_* is calculated as

$$u_* = \frac{u \kappa}{\ln \left(\frac{z}{z_{0m}} \right) - \Psi_u \left(\frac{z}{L} \right) + \Psi_u \left(\frac{z_{0m}}{L} \right)}, \quad (4A.4b)$$

where u is the wind speed, Ψ_u is the Businger-Dyer integrated Monin-Obukhov flux profile relation function for wind speed gradients. The Obukhov length L is calculated within the loop as

$$L = \frac{T_a u_*^2}{\kappa g T_{v*}}, \quad (4A.4c)$$

where the temperature scale T_{v*} is a scaled buoyancy flux. The scalar scales are calculated as

$$T_{v*} = \frac{-H_v}{\rho c_p u_*}, \quad T_* = \frac{-H}{\rho c_p u_*}, \quad q_* = \frac{-L_v E}{L_v \rho u_*} \quad (4A.4d)$$

where the buoyancy flux

$$H_v = H(1 + 0.61q) + 0.61 c_p T_a \frac{L_v E_0}{L_v} \quad (4A.4e)$$

and g is the acceleration due to gravity (9.81 m s^{-2}).

After H converged to one value, the following variables are extracted explicitly

for diagnosis:

$$T_s = T_a + \frac{Hr_a}{\rho c_p} + z\Gamma_d, \quad (4A.5a)$$

where Γ_d is the dry adiabatic lapse rate of 0.01 Km^{-1} . If T_s is known, the longwave outgoing radiation, net radiation, and soil and latent heat flux can be calculated following

$$L_{\text{out}} = \epsilon_s \sigma T_s^4 + (1 - \epsilon_s)L_{\text{in}}, \quad (4A.5b)$$

$$Q_n = S_{\text{in}} - S_{\text{out}} + L_{\text{in}} - L_{\text{out}} = Q_0 - \epsilon_s \sigma 4T_a^3 (T_s - T_a). \quad (4A.5c)$$

$$G = -A_g (T_{24h} - T_s) = G_0 + A_g (T_s - T_a), \quad (4A.5d)$$

and

$$L_v E = \frac{s(Q_n - G) + \frac{\rho c_p}{r_a} (e_{\text{sat}} - e_a)}{s + \gamma \left(1 + \frac{r_c}{r_a}\right)} = L_v E_0 + \frac{\rho c_p s (T_a) (T_s - T_a)}{\gamma (r_a + r_c)}. \quad (4A.5e)$$

4A.2 Appendix B; Coefficients capturing the wavelength dependency of C_{n^2}

For $\lambda < 1 \text{ mm}$

$$b_1 = 10^{-6} \left(\frac{0.237134 + 68.39397}{130 - \lambda^{-2}} + \frac{0.45473}{38.9 - \lambda^{-2}} \right), \quad (4A.6a)$$

$$b_2 = 10^{-6} (0.648731 + 5.8058 \times 10^{-3} \lambda^{-2} - 7.115 \times 10^{-5} \lambda^{-4} + 8.851 \times 10^{-6} \lambda^{-6}) - b_1, \quad (4A.6b)$$

$$b_{q2} = b_2, \quad (4A.6c)$$

and for $\lambda > 1 \text{ mm}$

$$b_1 = 0.776 \times 10^{-6}, \quad (4A.6d)$$

$$b_2 = 10^{-6} \left(\frac{7500}{T_a} - 0.056 \right), \quad (4A.6e)$$

$$b_{q2} = 10^{-6} \left(\frac{3750}{T_a} - 0.056 \right). \quad (4A.6f)$$

Acknowledgments

This work was financed by the DFG (Deutsche Forschungsgemeinschaft) project SI606/26-1 and GR2687/4-1, based on project SCHU2350/2-1; links between local-scale measurements and catchment-scale measurements and modelling of gas exchange processes over land surfaces. The Haarweg site was maintained by the Meteorology and Air Quality Group Wageningen, the Netherlands. Data from the EC station at the Merken site was provided by the DFG Transregional Collaborative Research Center 32, TR32, Germany. The BLLAST field experiment was hosted by the instrumented site of Centre de Recherches Atmosphériques, Lannemezan, France (Observatoire Midi-Pyrénées, Laboratoire d'Aérodologie).

5

Leaf water-use efficiency: impact on the estimation of evapotranspiration partitioning

Transpiration can be measured for a single plant, and soil evaporation can be measured on a squared meter of bare soil. However, measuring water vapor fluxes at a larger scale, e.g. using an eddy-covariance system, automatically leads to the sum of evaporation and transpiration, known as evapotranspiration. The same holds for observed CO₂ fluxes. Net ecosystem exchange (NEE) is observed at field scale, whereas gross primary production (GPP) is usually the variable of interest. Several partitioning methods exist for eddy-covariance data, of which one by Scanlon et al. (2010, Agr. Forest Meteorol. 150, 89-99). Their method is based on the observed correlation between CO₂ and water vapor fluctuations, and a water-use efficiency at leaf scale. We critically reevaluate their method and show some improvements on the determination of the water-use efficiency for growing wheat in Germany (western Europe).

5.1 Introduction

Crop-growth modelers, water-resource managers, farmers, and carbon and climate modelers, are all interested in plant transpiration, plant assimilation, soil evaporation and soil respiration on field scale. Field-scale instruments, however, only measure the total water-vapour and CO₂ fluxes. Continuous separate observations of the different soil and plant processes are not easy to obtain at field scale.

Models for estimating plant transpiration and soil evaporation are usually validated with data from lysimeters and from sap-flow measurements. Using a lysimeter, the weight of water that is lost from a certain volume of soil can be related to evaporation if no plants are in the volume, or under the canopy (Boast and Robertson, 1982). Using sap-flow measurements, transpiration rates can be derived for a single plant, by measuring the amount of heat that is taken up by the sap stream in the stem of the plant (Swanson, 1994). Transpiration estimates can also be derived using heavy stable isotopes of water (¹⁸O and ²H) as tracers of water movement in the soil and atmosphere (Zundel et al., 1978). However, this method only provides data occasionally.

Soil respiration is often measured using a so-called chamber, which is placed on top of the soil to measure the increase of CO₂ within the chamber (Graf et al., 2011). There are types that are easy to carry around to measure at several places temporally, and there are types that are installed at one location and provide data continuously. Assimilation of carbon by a plant is generally derived from measurements of chlorophyll fluorescence, or directly from the CO₂ exchange measured in the leaf cuvette of a mobile photosynthesis device (Long et al., 1996).

Sap flow instruments, lysimeters, chambers, and cuvettes only measure gas exchange very locally. None of these instruments provides both spatial and temporal variability of evaporation, transpiration, assimilation or respiration (except when using many instruments simultaneously or repetitively). Therefore, methods exist to derive the fluxes that correspond to these four processes indirectly from eddy-covariance observations. Eddy-covariance observations provide continuous field-scale values for the net exchange of CO₂ (*NEE*) and H₂O (evapotranspiration) between the surface and the atmosphere.

A method that is often used to estimate gross primary production (assimilation, *GPP*) from *NEE* is to derive daytime respiration from nighttime temperature and respiration data. However, despite a correction for the temperature-dependence of soil respiration, nighttime respiration is not representative for daytime respiration, due to a light dependency (Amthor and Baldocchi, 2001). Moreover, this method does not provide transpiration or evaporation values. Bos extended the Penman-Monteith model to describe the interactions between evaporation and transpiration in a partly wet plant canopy. Their modeled transpiration values compared well with sap-flow measurements obtained in a pine forest.

Scanlon and Kustas (2010), further referred to as SK10, developed an analytical

method to derive field-scale transpiration, assimilation, evaporation, and respiration from high-frequency eddy-covariance measurements. The method is based on the fact that there are two locations in the canopy that are the shared source or sink for both water vapour and CO₂. The soil is the origin of soil respiration and soil evaporation, whereas the stomata are the pathway that is shared by transpiration and assimilation. The latter two fluxes are quantitatively related by the water-use efficiency at leaf level. SK10 tested their method for data gathered over growing maize in Beltsville (USA). Palatella et al. (2014) applied the method to observations obtained over artichoke thistle (cultivated for biofuel) in southern Italy in April 2010. They speed-up the method by applying a different iterative method to solve the system (roots of the main function). Furthermore they stress that the resolvability of the system is very sensitive to the *WUE* estimate.

We here show an elaborated study on the sensitivity of the SK10-method to the *WUE*. Note that this leaf *WUE* is not the same as the ecosystem water-use efficiency, which could be derived from the ratio of the ecosystem CO₂ and H₂O fluxes (which would include the soil-related fluxes). We use eddy-covariance data observed over growing wheat to study the effect of different options in the calculation of the *WUE*. Those options are related to the way the internal concentrations (in the stomata) of water vapour and CO₂ are estimated. We compare different ways (described in Section 5.3.2) to derive the *WUE* for several environmental conditions, and investigate the impact of the uncertainties in the *WUE* on the resolvability of the system and on the partitioned fluxes.

5.2 Theory

5.2.1 General concept

The correlation between the atmospheric transport of temperature, humidity, and CO₂ has mainly been studied in the context of Monin-Obukhov similarity theory, according to which the transport of several scalars is similar. This implies that all observed scalar fluctuations are related to the same specific surface. For example, an eddy that is more moist than its environment because it just left a transpiring plant or evaporating surface, will also be warmer because of the relatively warm surface, leading to a positive temperature-humidity correlation ($r_{Tq} = 1$, with T for temperature and q for specific humidity), excluding any disturbances (e.g. entrainment, advection, non-stationarity). Over a bare soil, the two scalars related to evaporation (q) and respiration (CO₂, c) are positively correlated because both scalars are released from the soil, into the atmosphere ($r_{cq} = 1$). Above a fully vegetation-covered surface, plants are the only humidity source and CO₂ sink, due to photosynthesis, leading to an anti-correlation ($r_{cq} = -1$).

However, over a heterogeneous surface, there is a combination of several sources and sinks, such that scalar transport is not similar. A system of plants and

soil, where transpiration and evaporation together form the observed moisture flux, and where assimilation and respiration together form the observed CO₂ flux, will lead to an r_{cq} value between -1 and 1. Furthermore, de-correlation between temperature and humidity will then occur because the eddies come from different surface-types, moist versus dry and cold versus warm, see Moene and Schüttemeyer (2008). Entrainment of air at the top of the boundary layer might lower the scalar correlations at the surface as well, as was studied by van de Boer et al. (2014a), shown in Chapter 3.

5.2.2 Original method

Scanlon and Sahu (2008) developed a method based on eddy-covariance data, to relate an observed r_{cq} to the separate biophysical components of the moisture and CO₂ fluxes. The key parameter in this relationship is the water-use efficiency at leaf scale (WUE), i.e. the amount of CO₂ uptake, through stomata, that corresponds with a certain amount of water loss. The leaf WUE is based on the ratio of the CO₂ and H₂O fluxes at leaf level.

The humidity fluctuations that are related to transpiration (σ_{q_T}), and the CO₂ fluctuations that are related to assimilation (photosynthesis, σ_{c_A}), are related via the WUE :

$$\sigma_{c_A} = WUE \sigma_{q_T}. \quad (5.1)$$

Figure 5.1 shows how the WUE can be used to determine the range at which a combination of the four fluxes related to assimilation (A), transpiration (T), respiration (R) and evaporation (E) can be found. The ratio of A and T is known via the WUE , and the total humidity ($T+E$) and CO₂ ($A+R$) fluxes are the fluxes as observed at the field scale. Starting at the combination of the observed fluxes, and keeping A/T constant by following the WUE slope, a range of combinations (yellow in Figure 5.1) can be defined where both the respiration and evaporation flux are positive.

For the exact combination of flux contributions, a system of equations considering correlation coefficients has to be solved. Within this system, the correlation coefficient between transpiration related q -fluctuations and assimilation related c -variations r_{q_T, c_A} is -1 because transpired water vapour leaves the canopy, and assimilated carbon enters the canopy. Evaporated soil water and respired soil CO₂ both leave the soil, such that $r_{q_E, c_R} = 1$. Furthermore, plant transpiration and soil evaporation are equally well (or poorly) correlated as plant assimilation and soil respiration, with a reversed sign ($r_{q_T, q_E} = -r_{c_A, c_R}$). For the correlation between soil and plant related variations in humidity and CO₂ variations, the following assumptions are made:

$$r_{q_T, q_E} = \frac{Fq_E \sigma_{q_T}}{Fq_T \sigma_{q_E}}, \quad (5.2)$$

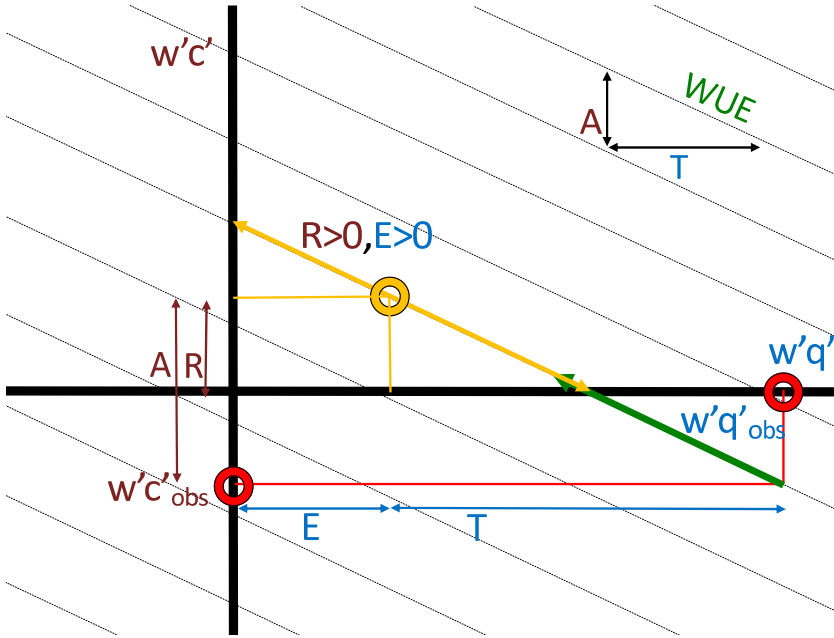


Figure 5.1: Schematic of how the WUE is used to obtain a range of combinations (thick, yellow arrow) of assimilation (A), transpiration (T), respiration (R), and evaporation (E), from the observed humidity and CO₂ fluxes ($w'q'_{obs}$, and $w'C'_{obs}$ respectively). Yellow circle: one of the possible combinations of respiration and evaporation that would cause the observed (kinematic) fluxes that are indicated with the red circles.

$$r_{CAcR} = \frac{F_C R \sigma_{CA}}{F_{CA} \sigma_{CR}} \quad (5.3)$$

From these assumptions and a few mathematical characteristics, it can be derived that:

$$WUE = \frac{F_c 1 \pm \tilde{q}}{F_q 1 \pm \tilde{c}'} \quad (5.4)$$

where F_c and F_q represent the total observed CO₂ and H₂O fluxes, and $\tilde{q} = F_q E / F_q T$ and $\tilde{c}' = F_C R / F_{CA}$. \tilde{q} and \tilde{c}' are determined by the roots of the two quadratic functions that relate the observed humidity and CO₂ variances (σ_q and σ_c), with the estimated WUE, r_{CAcR} and σ_{CA} . See for this implementation Palatella et al. (2014), which basically leads to the same as the implementation of SK10. Equation 5.4 provides an implicit relationship between observed quantities (fluxes, variances, correlation coefficients, WUE) and unknown quantities (in particular E/T and R/A). This relationship yields at most one physically realistic solution for E/T and R/A . From those ratios, in combination with the observed total fluxes, the component fluxes can be determined.

SK10 applied their method to data from a growing-maize field. Maize is a C4 plant, that means it uses a more efficient way to fixate carbon than C3 plants (e.g.

sugar beets, and grasses like wheat). I.e. the same amount of carbon fixation results in less water loss for a C4 plant compared to a C3 plant, corresponding to a higher *WUE*.

In SK10, c_e and q_e are estimated at leaf-level from the observed concentrations, applying an empirical vertical concentration profile that is based on Monin-Obukhov similarity theory (Brutsaert, 1982). Therefore, the method requires the roughness lengths for CO_2 and q (z_{0q}), that are both derived from the height at which the wind speed theoretically becomes zero (z_{0m}). These roughness lengths depend on the canopy height h_c , in SK10 following $z_{0m} = 0.1h_c$, and $z_{0h} = z_{0m}/e^2$. SK10 assume that c_i is 280 ppm for C3 plants, which equals $280 \times 10^{-6} p/(\rho R_c T) = 0.42 \text{ g kg}^{-1}$ for $\rho = 1.2 \text{ kg m}^{-3}$, $p = 1002.5 \text{ hPa}$, $T = 293 \text{ K}$, and $R_c = 189.9 \text{ J kg}^{-1} \text{ K}^{-1}$ (the gas constant for CO_2). For C4 plants, SK10 assume that $c_i = 0.44c_e$. Furthermore, q_i is assumed to be the saturated value at the leaf temperature $q_{\text{sat}}(T_a)$.

Because the partitioning method is based on the correlation coefficient between humidity and CO_2 , its performance is very sensitive to advection, entrainment and large-scale weather effects (see Section 5.2.1). Therefore, SK10 eliminate relatively large scale fluctuations. This is done by wavelet analysis, using the discrete Haar wavelet. A solution is derived, if any, for 15 levels of data elimination. For 20 Hz datasets of 30 min. (36.000 data points), this means that the first solution that is found is based on the first 27 minutes (2^{15} data points) of raw data, the second contains scales $<13.5 \text{ min.}$, the third $<6.8 \text{ min.}$, the fourth $<3.4 \text{ min.}$, etc.

5.2.3 Determination of *WUE*

In SK10, the *WUE* is estimated by dividing the CO_2 concentration difference between the stomata and the air just outside the leaf, by the humidity concentration difference between the stomata and the air:

$$WUE = -0.7 \frac{c_e - c_i}{q_e - q_i}, \quad (5.5)$$

where the subscripts 'e' and 'i' indicate the external and internal concentration in g CO_2 per kg air (c), and in kg H_2O per kg air (q). The factor 0.7 accounts for the difference in diffusivity between CO_2 and H_2O , which is approximately 1/1.6 as derived in Willmer and Fricker (1996). The internal CO_2 concentration should be lower than the external concentration to maintain CO_2 uptake. The internal H_2O concentration will then be higher than the external concentration, leading to a negative fraction, but to a positive *WUE* as defined in Equation 5.5 (SK10 define *WUE* negative).

The *WUE* should be evaluated for the height at which the exchange between plants and atmosphere takes place: at leaf-level. SK10 however assume an isothermal atmospheric surface layer, such that leaf temperature is equal to air temperature. We introduce the use of a non-isothermal atmospheric surface layer, in which the leaf temperature is higher than the observed air temperature (at daytime). Sim-

ilar to estimating c_e and q_e , we use the heat roughness length z_{0h} and an empirical profile derived from Monin-Obukhov similarity theory to estimate leaf temperature. It is however questionable what the exact leaf-level within a vegetation canopy is, i.e. where the sources and sinks are located on average within the canopy.

Furthermore, like SK10 state, if the distance from observation height increases, uncertainties arise in the extrapolation of q and CO_2 , and in case of the non-isothermal configuration in the derivation of the leaf temperature as well. These uncertainties in the WUE follow from assuming Monin-Obukhov similarity theory, and using surface fluxes that are not always well-defined. Moreover, the similarity relationships that are used for extrapolation are actually not valid within the canopy, in the so-called roughness sublayer (Harman and Finnigan, 2007). Scatter-wise, it might be more robust to evaluate WUE at observation height.

Denominator of WUE

Both the vertical profiles of temperature and humidity determine the vertical profile of the denominator of the WUE , $q_i - q_e$. This difference in specific humidity is related to the water vapor deficit vpd , which equals $e_{\text{sat}} - e_a = (q_i - q_e) \frac{\rho R_v}{R_d}$ (R_d and R_v are the gas constants for dry air and for water vapor, 287 and 461 J K⁻¹kg⁻¹ respectively). The WUE that is evaluated at a specific height, differs from the WUE derived from the same observations for a different height.

Before we quantify the change of WUE with height in Section 5.4.2, we first derive that there is a situation for which the vpd does not change that much with height, i.e. $(\delta q_{\text{sat}} - \delta q)/\delta z \approx 0$. To find the situation for which WUE does not depend on height, we use the vertical gradients derived for observation height. We rewrite the first term $(\delta q_{\text{sat}}/\delta z)$ to obtain a temperature gradient which we can rewrite in terms of the, from Monin-Obukhov similarity derived, flux-gradient relationship $\phi(z/L)$:

$$\frac{\delta q_{\text{sat}}}{\delta T} \frac{\delta T}{\delta z} = s \phi_h \frac{T_*}{\kappa z}, \quad (5.6)$$

where s is the increase of q_{sat} for a certain temperature increase, T_* is the heat flux divided by the friction velocity, $-H/(\rho c_p u_*)$ (where H is the sensible heat flux in W m⁻², ρ is the density of the air in kg m⁻³, c_p is the specific heat capacity of air at constant pressure (p) that depends on humidity, and u_* is the friction velocity in m s⁻¹), and κ is the von Kármán constant (0.4). The second term $\delta q/\delta z$ can be written in terms of ϕ as well, using $q_* = -L_v E/(\rho L_v u_*)$ (where $E = Fq$, L_v is the latent heat of vaporization in J kg⁻¹, and their product $L_v E$ is the latent heat flux in W m⁻²). Assuming that the ϕ -functions are equal for temperature and humidity leads to

$$s \frac{H}{c_p} = \frac{L_v E}{L_v}. \quad (5.7)$$

This means that the vpd does not change with height for the Bowen-ratio $\beta =$

$H/L_v E = \frac{1}{s} \frac{c_p}{L_v}$. A typical value would be $\beta = 0.5$, assuming a temperature of 293 K and humidity of 10 g kg^{-1} (then $s = 143 \text{ Pa}^{-1}\text{K}^{-1} = 889 \text{ mg K}^{-1}$). We will in this Chapter study the height-dependence of the WUE for a whole range of Bowen ratios.

Numerator of WUE

Instead of using a fixed internal CO_2 concentration, we introduce the use of a parameterization from the so-called $A-g_s$ -model to determine c_i . This plant-physiological model relates assimilation (A) to stomatal conductance g_s through the difference between internal and external CO_2 concentration, c_i and c_e respectively, (Ronda et al., 2001). The estimate of c_i is based on the v_{pd} :

$$c_i = (f_{\max} - a_d v_{pd})(c_e - \Gamma) + \Gamma. \quad (5.8)$$

For C_3 plants, $f_{\max} = 0.89$, $a_d = 7 \times 10^{-5} \text{ Pa}^{-1}$, and the CO_2 compensation concentration $\Gamma = 4.5 \times 10^{-5} 1.5^{\frac{T-298}{10}} \text{ kg kg}^{-1}$. For C_4 plants, $f_{\max} = 0.85$, $a_d = 15 \times 10^{-5} \text{ Pa}^{-1}$, and $\Gamma = 4.3 \times 10^{-6} \text{ kg kg}^{-1}$. Note that this parameterization introduces the v_{pd} -dependence in the numerator of WUE as well.

5.3 Methods

We elaborately studied the method that was developed by SK10. We applied their method to eddy-covariance data observed above a wheat field for the growing season, using several adaptations to their code.

5.3.1 Data

The FLUXPAT-2009 campaign was organized near Merken (Germany, 114 m a.s.l.) in the summer of 2009 to study the soil-vegetation atmosphere system (see Chapter 2 for more details). Among other stations, one station with an eddy-covariance system at 2.4 m a.g.l. was installed in the middle of a flat winter wheat field. All eddy-covariance stations provided 20 Hz wind speed, temperature, humidity and CO_2 concentration (CSAT3, LI-7500), and pressure data. Biweekly measurements of canopy height h_c were performed, from which we derived a linear wheat-canopy growth. The wheat was growing 65 cm in 50 days, starting at a height of 10 cm at 15 April (DOY 105). From 12 June on (DOY 163), the wheat height remained 0.85 m. The displacement height (at which momentum transfers between the air flow and the vegetation) is assumed to be $d = \frac{2}{3} h_c$.

As SK10 did, we allowed a maximum of 25% missing high-frequency samples, and filled the data gaps using a normal distribution or a generalized extreme-value distribution, depending on the skewness of the data (with < 0.2 as threshold for a normal distribution). The high-frequency data was verified for being within physical

limits ($-10 < u, v, w < 10 \text{ m s}^{-1}$, $-20 < T < 50^\circ\text{C}$, $0 < \text{H}_2\text{O} < 0.1 \text{ g m}^{-3}$, $0 < \text{CO}_2 < 0.02 \text{ mg m}^{-3}$, and $80 < p < 140 \text{ kPa}$).

5.3.2 Research strategy

We use the technique provided by SK10 and implement the different c_i and q_i approaches presented in Section 5.2.3. We use our scheme with different configurations, where T_a indicates an isothermal air layer above the surface, and where $c_i = f(T, q, c)$ indicates that we apply the $A-g_s$ parametrization:

$$\text{Ta-280: } c_i = 280 \text{ ppm, } q_i = f(T_a)$$

$$\text{Ts-280: } c_i = 280 \text{ ppm, } q_i = f(T_s)$$

$$\text{Ta-Ags: } c_i = f(T_s, q_s, c_s), q_i = f(T_a)$$

$$\text{Ts-Ags: } c_i = f(T_s, q_s, c_s), q_i = f(T_s)$$

$$\text{robust: } c_i = f(T_a, q_a, c_a), q_i = f(T_a)$$

We compare the WUE 's for the different configurations by presenting their daily (6-18 UTC) course for the growing ($DOY < 200$) and the ripening phase ($DOY > 200$) of the wheat data. Also, we compare probability density functions of the WUE for the isothermal and non-isothermal case, based on data obtained in the afternoons (12-16 UTC). We furthermore study the dependence of the WUE on the vertical temperature profile for varying conditions, for a relative humidity of 0.6-1, and for a Bowen ratio of 0.1-10.

For the same conditions, we quantify the influence on WUE of the height at which q_e and c_e are evaluated. Based on the explanation in Section 5.2.3, we compare the WUE evaluated at h_c , with the WUE evaluated at $0.75h_c$. To examine whether WUE can be evaluated at observation height instead of in the canopy, we also compare the WUE evaluated at $3h_c$ with the WUE evaluated at $0.75h_c$. We choose $0.75h_c$ as a reference because the correct evaluation height should roughly be in the upper half of the canopy (Graf et al., 2014).

Note that either all variables should be taken from observation height, or they should all be extrapolated to the same evaluation height that lays within the canopy (unlike in the original method of SK10, where the temperature is not extrapolated). We moreover quantify the effect of the WUE on the partitioning, based on two hours of data during the growing season of the wheat. These data were selected because for these hours, the method finds a partitioning solution without eliminating low-frequency data.

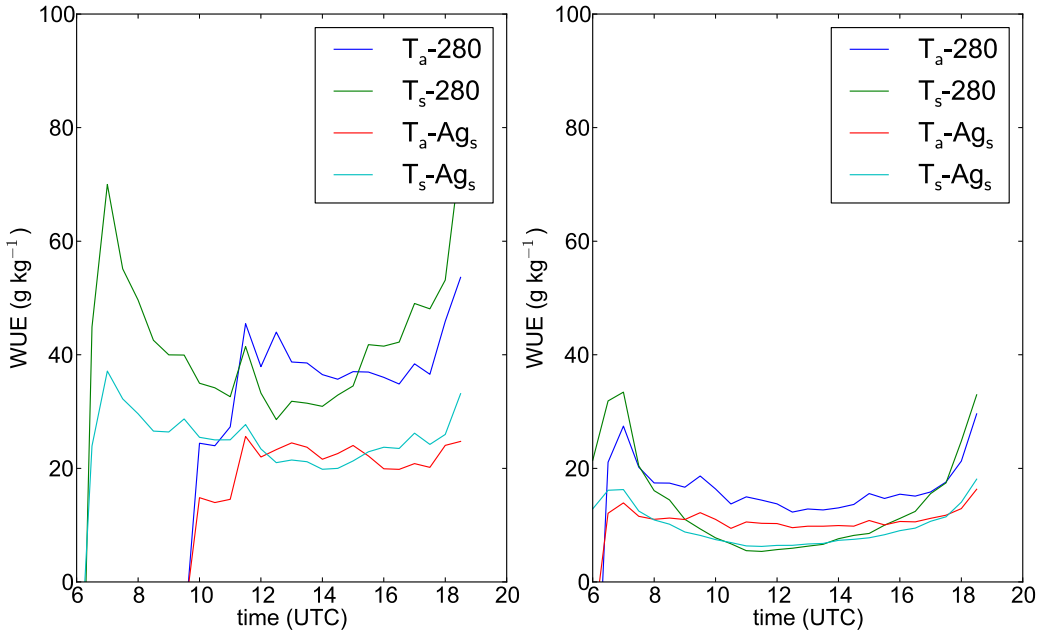


Figure 5.2: The daily course of the WUE in g kg^{-1} for the growing (left, $\text{DOY} < 200$) and ripening (right, $\text{DOY} > 200$) phase of a winter wheat, derived using the first four different methods that are described in Section 5.3.2, considering the estimations of the internal CO_2 and H_2O concentrations.

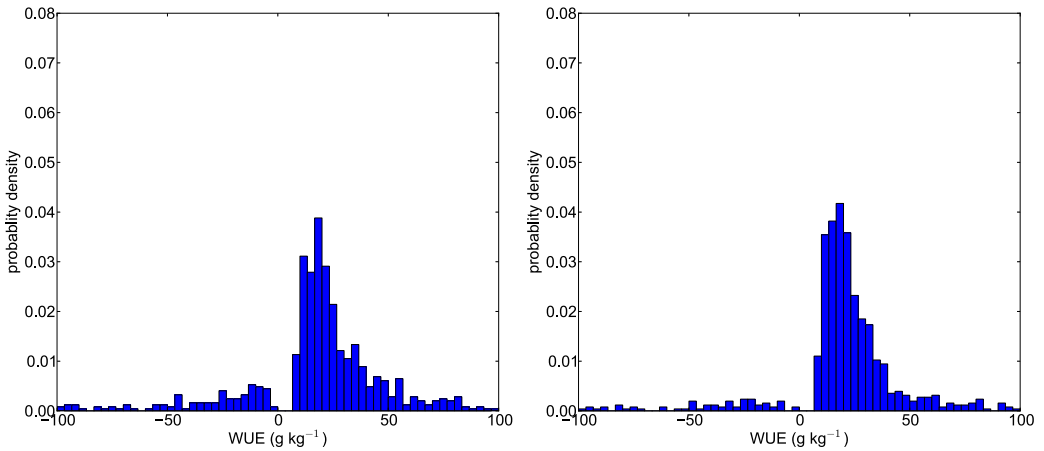


Figure 5.3: Probability density functions of WUE, for daytime data (12-16 UTC), obtained over a growing winter wheat. Left: $T_a\text{-}Ag_s$, right: $T_s\text{-}Ag_s$ (see Section 5.2.3).

5.4 Results

5.4.1 WUE: methods to derive external and internal CO₂ and H₂O concentration

In Figure 5.2, we show the *WUE* for the first four configurations described in Section 5.2.3. First of all, there is a clear difference in the early mornings between the isothermal and the non-isothermal configurations. Using the temperature at observation height for the determination of q_i (Ta-280 and Ta-Ags) results in a very small difference with q_e for humid conditions. This may result in either a very high, or a strongly negative *WUE* (which is physically impossible). As we can see in Figure 5.2, this occurs mostly in the early mornings, when the air is close to saturated. For these hours, the non-isothermal configurations lead to a plausible *WUE*. Figure 5.3 shows as well that the use of a surface temperature for deriving q_i , decreases the number of non-physical values for *WUE* significantly.

We furthermore show in Figure 5.2 that the *WUE* is lower at the end of the season for all configurations, especially the estimates using the 280 ppm-cases decrease significantly. In the growing phase, the *WUE* decreases during the afternoon, when the temperature increases. This effect is stronger for the isothermal cases. We moreover found that the external CO₂ concentration does not differ much throughout the season, such that the numerator of *WUE* depends mainly on c_i . The internal CO₂ concentration that was kept 280 ppm (0.42 g kg⁻¹) in the original model, is generally higher than 280 ppm using *A-g_s*, but lower than that at the end of the measurement campaign (not shown).

In Figure 5.3 we show the probability density functions using the observed air temperature to derive the internal leaf humidity concentration (left), and using a leaf temperature that was extrapolated from observed air temperature (right). Because the internal CO₂ concentration is known to depend on meteorological conditions (Lauer and Boyer, 1992), we only show the two *A-g_s* configurations. As already mentioned, much less negative values occur for *WUE* by introducing a leaf temperature. However, we here see that the scatter of the *WUE* is slightly larger for this non-isothermal case, which has a wider distribution around 20 g kg⁻¹, and a less clear peak.

Figure 5.4 shows the *WUE* for the observed range of relative humidity (*RH*) and Bowen ratio. In the first case (isothermal), we see that, for a given *RH*, the *WUE* decreases when the Bowen ratio increases (decreasing evapotranspiration) as will happen during the ripening phase of a crop. In the non-isothermal case, this effect of Bowen ratio on the *WUE* is reverse and also stronger. Furthermore, the limit where *WUE* = 0 is clearly visible (we excluded negative values).

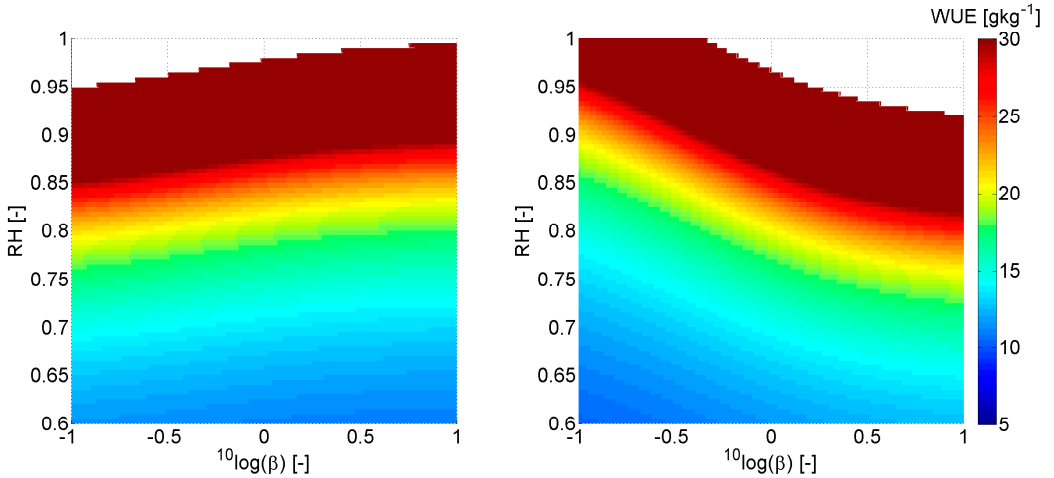


Figure 5.4: The effect of the Bowen ratio and the relative humidity on the WUE ($g\ kg^{-1}$). Left: Ta -Ags, right: Ts -Ags. Negative values are eliminated (white), and dark red indicates a very high WUE . Based on observations, we used $Q_n = 300\ Wm^{-2}$, $u_* = 0.3\ ms^{-1}$, $c_m = 5.5 \times 10^{-4}\ kg\ kg^{-1}$, $c_* = -12/700\ q_*\ K$, $h_c = 1\ m$, $z_m = 3\ m$, $p = 100.25\ kPa$, $\rho = 1.2\ kg\ m^{-3}$, $T_m = 293K$.

5.4.2 WUE: evaluation-height dependence

Here we describe the importance of the exact height for which the WUE is evaluated, applying a non-isothermal surface layer and the A - g_s parametrization (Ts -Ags). Figure 5.5 shows how the WUE relatively changes ($\Delta WUE/WUE$) when we evaluate WUE at two different heights. In the left figure, we compare the WUE determined for $z = 0.75h_c$ with the WUE at the canopy top. In the right figure, we compare the WUE determined for $z = 0.75h_c$ with the WUE determined for observation height. Both cases are based on observations at 3.0 m and $h_c = 1\ m$.

In both comparisons, we see the same pattern, with a specific β at which the method is not sensitive to the evaluation height (black line) as explained in Section 5.2.3. Until DOY 200 (19 July), the Bowen ratio of the wheat was 0.1 ($= 10^{-1}$). From DOY 200, the ripening of the wheat made β increase linearly to 4.5 ($\approx 10^{0.65}$) at DOY 215 (3 August), when the wheat was harvested. For $\beta = 0.1$, the WUE increases with increasing distance between observation height and evaluation height. For $\beta = 4$, the WUE decreases with increasing distance between observation height and evaluation height (see Figure 5.5).

For the within-canopy comparison, the sensitivity to the evaluation height is only significant in very humid conditions, when the vertical profiles of specific humidity and of saturated humidity content are almost equal. In other cases, it does not matter much whether the observed temperature, humidity, and CO_2 values are extrapolated towards the canopy top, or a bit lower than that top.

Evaluating the WUE at observation level leads to significantly lower values for a growing season, and to clearly higher values for very high Bowen ratios. However,

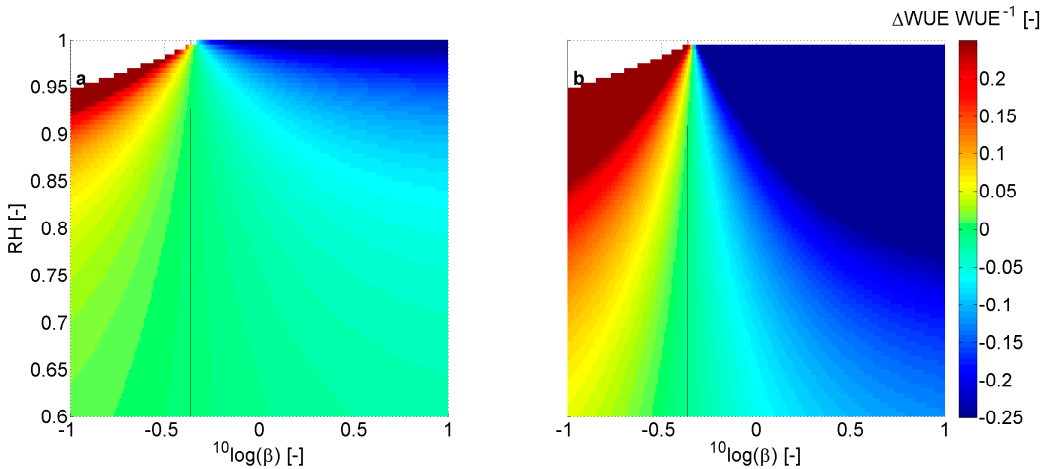


Figure 5.5: The relative increase in WUE per increase in evaluation height for the same cases as Figure 5.4, for Ts -Ags. Left: h_c vs. $0.75h_c$, right: $3h_c$ vs. $0.75h_c$ ($h_c = 1$ m). Dark blue and red indicates a large sensitivity of WUE to the evaluation height.

we show in Figure 5.6 that the scatter of the WUE using the Ta -Ags or the Ts -Ags configuration as shown in Figure 5.3 is reduced significantly by evaluating the WUE at observation height. For colder regions, the difference between evaluating at measurement height or in the canopy will even be higher for a growing season (we here used $T = 293$ K). This is, because s is lower for lower temperatures, such that the β at which the vpd does not change with height will be higher, and the whole figure will move rightward.

5.4.3 Hybrid method to derive WUE

We here propose a solution for the scatter that is introduced by the extrapolations of humidity, CO_2 , and temperature in the WUE determination. The ‘robust’ WUE that is derived directly from the observed variables reduces scatter (see Figure 5.6), but is biased (see Section 5.2.3) and thereby decreases the resolvability of the partitioning method. Therefore, we scale the robust WUE with the daytime median of the WUE that is derived from the variables that are all extrapolated into the canopy (Ts -Ags). Thereby, we obtain a WUE that generally leads to a solution of the flux partitioning, which is physically more substantiated than the original method.

The daily course of this so-called ‘hybrid’ WUE , derived from the wheat data, is presented in Figure 5.7. We show that compared to the Ts -Ags configuration, the hybrid configuration is of the same order of magnitude, which means that the bias of the ‘robust’ method is decreased in the hybrid method. Because the hybrid method is based on the ‘robust’ method, its probability density function will look similar as Figure 5.6, with low scatter. Thereby, the hybrid method will be an improvement on the WUE determination in SK10.

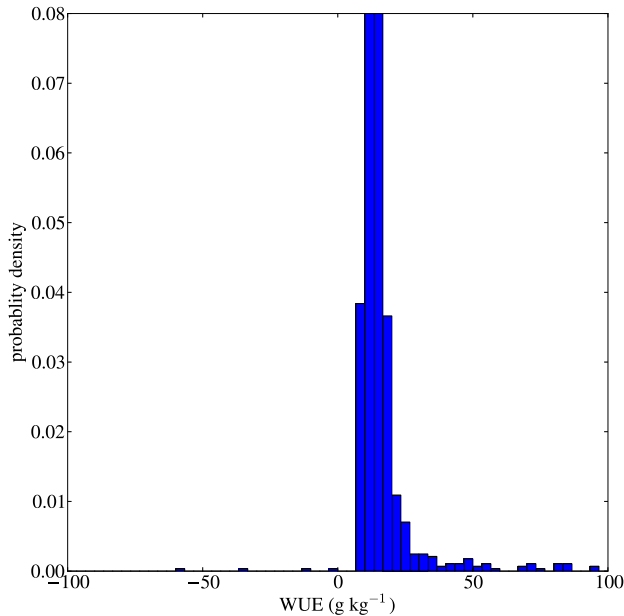


Figure 5.6: The probability density function of WUE , for daytime data (12-16 UTC), obtained over a growing winter wheat, derived using the $A-g_s$ parametrization and the observed air temperature, humidity and CO_2 concentration without extrapolating towards the canopy ('robust').

5.4.4 Partitioned fluxes: WUE dependence

In Figure 5.8 we show for two half hours of data, the influence of the WUE on the partitioning, and thereby the effect of the different configurations on the partitioning. First of all we see that there is a wide range of WUE 's for which the solution method of SK10 finds a solution to explain the observed fluxes, variances and correlations. Solutions are found for a WUE up to 7000 g kg^{-1} , for which all ET is assumed to be evaporation. No solution is found for these two cases for $WUE \lesssim 10$. That is, because an observed negative CO_2 flux can only be explained by photosynthesis and thus transpiration, which means that there is a certain base value for WUE .

The contribution of transpiration to the total humidity flux decreases with increasing WUE , because a higher WUE means that for the uptake of a fixed amount of CO_2 , less transpiration is needed. The different configurations lead for the data of DOY 149 (13 UTC) to a maximum WUE difference of 10 g kg^{-1} . This leads to a transpiration flux between 146 and 218 W m^{-2} . For DOY 153, the differences between the configurations is smaller, and the order of the configurations slightly changed. Still, the range of transpiration contributions is quite large (between 0.7 and 0.9).

The WUE for both data points determined using the 'robust' method are 10.5 and 8.6 g kg^{-1} (D149 and D153 respectively). These are however not shown in the Figure, because no partitioning solution is found for these low values for WUE .

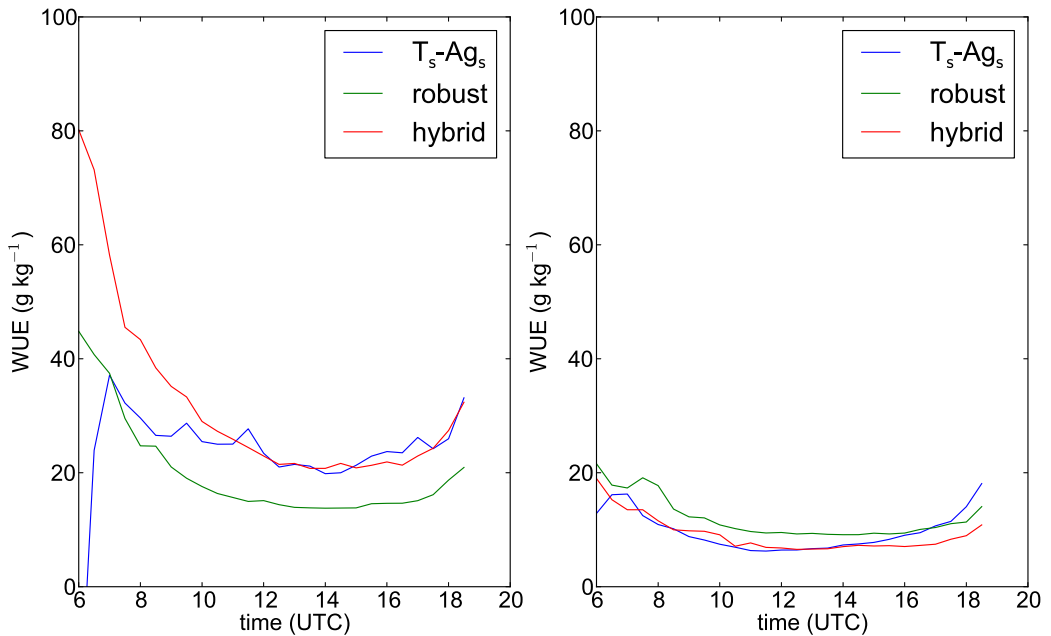


Figure 5.7: The daily course of the WUE for the growing (left) and ripening (right) phase of a winter wheat (comparable with Figure 5.2). In all cases, the $A-g_s$ parameterization was applied. In T_s-Ag_s , q , c , and T are extrapolated, in ‘robust’ none of the variables is extrapolated, and hybrid is a combination of both configurations (as described in Section 5.5).

5.5 Discussion

In this Chapter we show the influence of the surface temperature (which is assumed to be the leaf temperature) on the WUE and thereby on the partitioning of evapotranspiration. We use functions derived from Monin-Obukhov similarity theory to estimate the surface temperature. However, these functions introduce scatter by extrapolating air temperature. Moreover, their validity is uncertain, especially within the vegetation, that is located in the roughness sublayer (Harman and Finnigan, 2007). To overcome the scatter and uncertainty, the leaf temperature could be derived from outgoing longwave radiation measurements, if available, as described in Chapter 4.

We found that for obtaining a solution with the method of SK10, often many larger-scale frequencies (wavelet levels, see Section 5.2.2) have to be eliminated. We however show in Chapter 3 that surface-related turbulence is captured by timescales up to 15 min. By eliminating those scales, flux contributions are lost, and we found that that slightly changes the partitioning fractions. Furthermore, this part of the method is very time consuming. Therefore, we suggest to perform a sensitivity study on the flux-partitioning method, considering the wavelet part of the method. Ideally, it should only be necessary to exclude scales > 15 min.

The partitioning system did not solve, or only solved for a low wavelet level, for

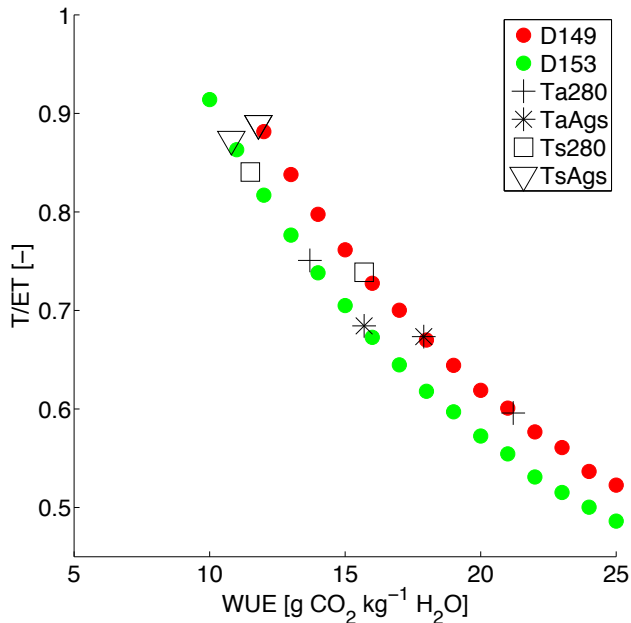


Figure 5.8: The contribution of transpiration to the total observed humidity flux, derived from a range of *WUE*'s that is defined from the different methods (see Section 5.3.2) to determine the *WUE* for the winter wheat, for DOY 149, 13 UTC and DOY 153, 14 UTC.

our wheat data in the ripening phase and for the period after harvest. Thereby, we could not study the development of the crop. A more elaborated study should therefore be performed on how to increase the success rate of the method. The assumption described in Equation 5.2 should thereby be taken into account. With a tool that often finds a solution for various environmental conditions, obtained respiration fluxes can be compared with chamber data and soil moisture data, to validate the flux output of the model. Also, quality checks can be performed by e.g. comparing the evaporation rate before and after harvesting, relating respiration fluxes with temperature observations, and linking precipitation events to the evaporative flux.

The concept of the *WUE* could be combined with existing methods to derive the four partitioned fluxes. This could for example be done with the method that derives daytime respiration from the observed nighttime CO₂ flux. From the total CO₂ and H₂O flux, the *WUE*, and the estimated respiration flux, the assimilation, transpiration and evaporation fluxes can be derived following the system described in Figure 5.1. However, the amplification of errors should hereby be taken into account, as the smallest flux is used to determine the other three fluxes by this method.

Once a well-established partitioning tool has been developed, the effect of the degree of plant-scale surface heterogeneity on Monin-Obukhov similarity functions can be studied. It is expected that when soil evaporation significantly contributes to the observed moisture flux, Monin-Obukhov similarity is less valid for moisture. That is, because the humidity source at the surface then actually consists of a source

exactly at the surface, and a source around canopy height.

5.6 Conclusions

In this chapter we demonstrate that the determination of WUE by SK10 often results in unphysical values for the data obtained over a growing wheat field, such that no solution is found in their partitioning method. This is mainly caused by their assumption that the leaf temperature is equal to the observed air temperature. In their method, the humidity just outside the leaf is extrapolated from the observed air humidity by applying flux-profile functions derived from Monin-Obukhov similarity theory. Meanwhile, the internal leaf humidity is determined as the saturated humidity at air temperature. This results often in a very large or a negative WUE , especially for relatively humid conditions. We show that extrapolating air temperature to leaf temperature avoids these unphysical values. However, this extrapolation based on not-always well-defined surface fluxes introduces scatter in the WUE , additional to the scatter caused by the extrapolation of observed H_2O and CO_2 concentrations.

Furthermore, we show that using the observed air temperature to derive the internal humidity, is not a problem for a surface with a Bowen ratio of ≈ 0.5 (based on $T = 293$ K). We moreover found that the exact height for which the WUE is determined, i.e. towards which the observations are extrapolated, does not significantly affect the WUE when evaluating somewhere between the canopy top and halfway the canopy. We show that the scatter of WUE is reduced significantly by using the observed temperature, humidity and CO_2 concentration directly, without extrapolating.

However, evaluating the WUE directly from the observations, without extrapolations, leads to a bias in WUE of which the sign and the magnitude depend on the Bowen ratio. At Bowen ratios representative for actively growing vegetation, the WUE is underestimated when evaluated with observation-level values. To reduce scatter and to prevent a bias, we propose to scale our robust method (no extrapolation), with the daytime median WUE that is estimated for an extrapolated temperature, humidity and CO_2 concentration. This hybrid method will more often lead to a solution of the flux partitioning method, compared to the original method.

The method of SK10 furthermore assumes a fixed internal CO_2 concentration. We show the effect of including a dependence on the external concentrations of humidity and CO_2 . Our parametrization that is based on the $A-g_s$ model generally lowers the WUE , which leads to a relatively higher contribution of transpiration to the observed evapotranspiration flux. The effect of the different WUE determinations on the flux partitioning is rather large. Taking into account the variations of the internal CO_2 concentration and an extrapolated leaf temperature, can change the fraction of transpiration from 0.6 to 0.9.

Acknowledgments

We thank Todd Scanlon for providing his code. The field dataset was contributed by the DFG (Deutsche Forschungsgemeinschaft) via the Transregional Collaborative Research Center 32, TR32, Germany. This work was financed by the DFG project SI606/26-1 and GR2687/4-1, that deal with links between local-scale measurements and catchment-scale measurements and modeling of gas exchange processes over land surfaces.

There is no theory of everything.

Stephen Hawking

6

Perspectives

6.1 Footprint modeling over complex terrain

In our studies on turbulent scalar transport between crops and the atmosphere, we were confronted with the influence of the spatial and temporal distribution of the scalar sources and sinks at the surface and at the top of the boundary layer. We can confirm that the variability and scaling properties of turbulence change strongly through surface heterogeneity and entrainment. These processes are however not fully incorporated in (semi-) analytical flux-footprint models, since these footprint models are based on Monin-Obukhov similarity theory. Such footprint models should therefore actually not be applied to heterogeneous terrain. However, we cannot test the accuracy of a footprint model on data obtained over a homogeneous terrain.

Our footprint-model study revealed that existing semi-analytical footprint models result in significantly different footprints for identical eddy-covariance measurements. This is a problem when using these models for other purposes than as a data quality check, e.g. for determining which part of the observed flux comes from a specific surface. For our studies on relatively flat and homogeneous areas, we selected a model configuration for which the estimated footprint was most similar to the footprint derived from a composite of known fluxes from the FLUXPAT 2009 campaign in Germany. However, it is important to further improve footprint models to make them applicable to more complex terrain (i.e. very heterogeneous, with contrasting land-surfaces and topography). This would allow integrating a footprint model into the FLUXNET database, that is collected within the global network of

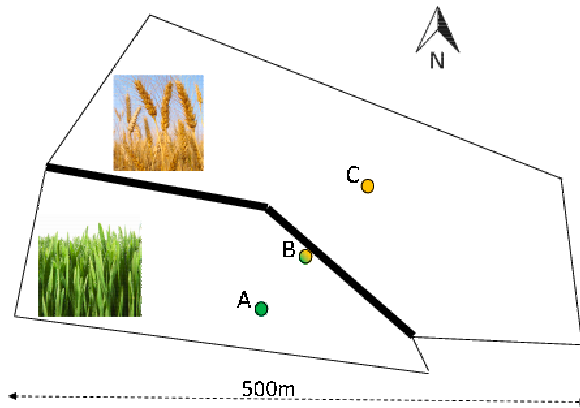


Figure 6.1: Locations of the three eddy-covariance stations (circles A, B and C) at the so-called edge-site during the BLLAST campaign in 2011 in Lannemezan, France. The thick black line indicates a ditch between the grass and the wheat field.

micro-meteorological flux measurement sites (Baldocchi et al., 2001). At several FLUXNET sites, the flux measurements have a heterogeneous fetch. An integrated, accurate but fast footprint model will lead to CO_2 and water vapor fluxes that can be upscaled, to verify remote sensing data, and to gain global insight in cycles and storage of these natural resources.

6.2 Footprint modeling for a highly turbulent atmosphere

For an eddy-covariance data-based study on the performance of footprint models, the exact location of the instruments at the border of different land-use types is very important. The distance of 50 m like used for the data described in Chapter 2 is too large, especially for unstable conditions when the footprint is respectively small. In the BLLAST campaign in 2011 in France, we took this into account. We measured surface fluxes in a wheat field, a grass field, and at the border between them, see the set-up in Figure 6.1. We installed the edge-station B exactly at the edge, next to a ditch. However, we found that this time, none of the footprint models we tested on the previous dataset performed well for the convective conditions observed during the BLLAST campaign.

In Figure 6.2 we present a comparison of the sensible heat fluxes observed at station B, with fluxes observed at station A (grass) and C (wheat), colored by wind direction. Because the measurement site was located 50 km north of the Pyrenees, we often observed a northerly wind at daytime (katabatic flow), and a southerly wind at nighttime. The estimated footprints of the daytime grass and wheat fluxes easily fitted within the fields, such that we assumed that these fluxes were representative for the two fields. From this, we could expect that the daytime flux that is observed

at station *B* is similar to the wheat flux, in case the wind direction is between 315° and 45° . These wind directions are colored dark red and dark blue in Figure 6.2. We see that for those wind directions, the sensible heat flux observed at station *B* is almost always larger than the grass flux, and clearly always smaller than the wheat flux. This indicates that the border measurements always consisted of a combination of the grass-related flux and the wheat-related flux, for all wind directions.

Footprint models generally predict an elongated ellipsoid upwind of the turbulence measurement, mainly based on atmospheric stability (via the Obukhov length) for the length, and the standard deviation of lateral horizontal wind speed (σ_v) for the width of the ellipse. When the turbulence intensity is that high such that the fluctuations in horizontal wind speed are as large as the mean wind speed itself, then vertical motions are relatively important for the dispersion. This corresponds to a relatively small circular footprint located around the instrument. This means that the footprint models should also calculate a footprint contribution downwind from the station, which is not possible with the current implementations. Kljun et al. (2004) presented an analytical footprint model that is based on an ensemble average of a 3D Lagrangian backward model for varying stratifications and heterogeneous surfaces. Their model captures downwind contributions for convective conditions in the alongwind direction, but unfortunately not yet in the crosswind direction. An improved version of their footprint model could be tuned by performing a natural tracer approach like described in Chapter 2, based on an eddy-covariance dataset like used in Chapter 3. An edge-station installed exactly at the border between two contrasting land-use types (like station *B*) is required, in combination with two stations with a homogeneous footprint for all wind directions in the two different fields (like station *A* and *C*).

6.3 Effect of surface heterogeneity on Monin-Obukhov similarity theory derived from observations

In Chapter 3 we quantify the effect of entrainment on Monin-Obukhov similarity functions, for the above-mentioned observations over grass and wheat. The station at the edge between the grass and wheat field was originally meant to quantify the effect of surface heterogeneity on Monin-Obukhov similarity theory. To study the influence of surface heterogeneity on atmospheric turbulence, we have to compare turbulence observed over a homogeneous area (were Monin-Obukhov similarity theory holds), with turbulence observed over a heterogeneous area. However, when do we define a certain site heterogeneous?

The heterogeneity of a site depends on the contrast between the surface flux of the scalar of interest. An area can be heterogeneous in terms of temperature,

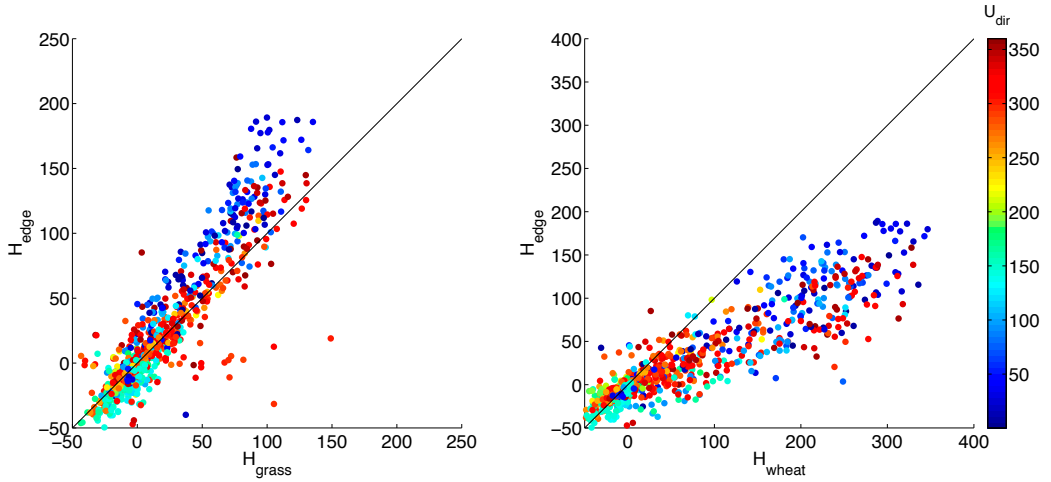


Figure 6.2: Comparisons between the sensible heat flux observed at the edge-station B (see Figure 6.1), with left the flux observed at the grass (station A), and right the wheat flux (from station C). Dark red and blue markers indicate northerly winds, observed during the BLLAST campaign (14 June - 5 July 2011) in Lannemezan, France. The black line indicates perfect equality between the fluxes.

and meanwhile homogeneous in terms of humidity. Considering the fetch of eddy-covariance measurements, the heterogeneity furthermore depends on the location of the footprint. We here define an index of heterogeneity (HI), that can be used to classify datasets. In case of two different land-use types, HI can be expressed as a function of both the contrast between the land-use types, and the contributions of the fields to the observed scalar variances:

$$HI = \left| \frac{F_1 - F_2}{(F_1 + F_2)/2} \right| \min(C_1, C_2), \quad (6.1)$$

where F_1 and F_2 represent the fluxes of land-use type 1 and 2, for a certain period (e.g. 30 min.), and C_1 and C_2 represent the contributions of the two fields to the observations in fractions. The flux-contrast part will be close to zero if the fluxes (e.g. H , CO_2 or $L_{\nu}E$) are similar, and will reach 2 for a maximum contrast (one of the fluxes is zero). Note that this definition only holds when F_1 and F_2 have the same sign. The contribution part will vary between 0 (the footprint is only located in one of the two fields) and 0.5 (the footprint has equal contributions of both fields), leading to a HI between 0 and 1. A footprint model that is accurate for various conditions, is essential for determining C_1 and C_2 .

We expect a relation between HI and the deviation from Monin-Obukhov similarity theory, e.g. the difference between the observed scalar variance and the variance expected from the flux-variance functions. This way, we are able to quantify the effect of surface heterogeneity on Monin-Obukhov similarity functions for several scalars (humidity and temperature). The fields observed during the BLLAST

campaign were especially contrasting in the sensible heat flux (H), because the relatively dry and high wheat canopy had a lower albedo than the growing grass. The latent heat flux observed over grass was only one third higher than observed over the ripening wheat, probably because the wheat field contained some other fodder types, of which some were still green at the end of the measurement campaign. If a whole range of wind directions would have occurred, we would have obtained turbulence data with various flux footprints, with various different degrees of heterogeneity in terms of H .

The degree of heterogeneity can be determined using a footprint model that is suitable for the observed atmospheric conditions (like discussed above). Until a footprint model is developed that performs well for a very unstable atmosphere, such a heterogeneity study should be performed using eddy-covariance data obtained at a station surrounded by two fields with contrasting heat fluxes in a not too convective atmospheric boundary layer ($z/L > -1/16$). Often, structure parameters and variances are used as a measure of turbulence. However, current footprint models are developed for fluxes (covariances). Therefore, differences between modeling the source area of turbulence quantities like (co-)variances and structure parameters should also be examined. Again, our natural tracer approach presented in Chapter 2 could be used for this, by examining whether a composite of structure parameters observed over two contrasting land-use types, using a flux-footprint model, leads to the structure parameter observed at a station at the edge between the fields.

6.4 Modeling deviations from Monin-Obukhov similarity functions

In Chapter 3 we derived a term that accounts for humidity variance caused by entrainment, from the humidity-variance budget. However, we thereby did not take any coupling between variances, covariances, dissipation, and TKE (turbulent kinetic energy) into account. We therefore recommend a more elaborated study on Monin-Obukhov dissimilarity, by using a closed set of equations that are combined by Vilà Guerau de Arellano et al. (1995). The equations consider the balancing production and dissipation of variances, covariances, and fluxes, that are non-dimensionalized using Monin-Obukhov similarity theory-derived scales. All diagnostic equations depend on the atmospheric stability (z/L), such that the system can be solved for certain similarity relationships for flux-gradients and variances of momentum, temperature, and any other scalar (e.g. humidity or CO_2).

We could compare observed similarity relationships (derived from e.g. eddy-covariance data) with those that follow from the system of equations described by Vilà Guerau de Arellano et al. (1995). Similar to our method described in Chapter 3, we could add justified terms in the equations within the system that has to be solved, to capture the observed processes. If for example the observed humidity

variance is higher than the model output, there is an indication that we need to add an entrainment term to the budget equations in the model.

Turbulent transport of CO_2 is different than that of humidity, because in contrast to humidity and temperature, the surface is a sink for CO_2 . In addition to that, the free atmosphere can be a source and a sink of CO_2 , depending on the season (a source in summer). Furthermore, CO_2 is a passive scalar, which means that its presence does not affect buoyancy. CO_2 transport is as relevant as humidity transport for climate-change related studies, therefore it would be interesting to apply our method presented in Chapter 3 to CO_2 . However, radiosonde CO_2 data is often not available, and it would be more feasible to apply the model by Vilà Guerau de Arellano et al. (1995), discussed above, to study the influence of surface heterogeneity and entrainment on Monin-Obukhov similarity theory for CO_2 .

Another method that is used to study the effect of surface heterogeneity and entrainment is the Dutch Atmospheric Large-Eddy Simulation, DALES (Heus et al., 2010). Using LES, various idealized cases can be simulated to obtain turbulence variables. Like for the method discussed above, spatial and temporal turbulence characteristics that follow from the simulation can be compared with eddy-covariance data. To study which processes influence the turbulence statistics for a certain eddy-covariance dataset, various simulations can be performed to achieve similar turbulence statistics for the LES and the observations. A surface consisting of two fields with different surface fluxes can for example be prescribed as done by Ouwensloot et al. (2011), who studied isoprene emissions over a land surface consisting of alternating cool and wet patches (high emission) with warm and dry patches (low emission).

The temperature variance that is caused by surface heterogeneity can be quantified by comparing simulations with different prescribed surfaces. To relate the amount of extra variance to a specific degree of surface heterogeneity, HI could be used as explained in the previous section. For studying surface-layer turbulence with DALES, a very fine resolution is needed for the lowest part. In DALES, the smallest turbulence scales are modeled within sub-grids, to save computing time. These sub-grid schemes are partly based on empiricism such that the resulting mean wind and temperature profiles do not follow Monin-Obukhov similarity theory. Because the smallest eddies especially occur in the surface layer, a direct numerical simulation (DNS) might be better than an LES to study surface-layer turbulence. However, a DNS resolves every scale, and is therefore too expensive (time wise) to simulate various cases.

6.5 Applications to urban areas

As the main land-use type is changing from agriculture to urban areas in developed countries, more and more research is performed on the urban climate. In urban studies, sensible heat and CO₂ fluxes and their source areas are of big interest. However, the obstacles in urban terrain differ extremely in height compared to a plant canopy. This is a problem for analytical footprint models, because they assume a flat terrain over which the height-dependent turbulent characteristics are calculated. A recent attempt of modeling CO₂-flux footprints over an urban area has been performed by Kotthaus and Grimmond (2012). The footprint-model validation method that we described in Chapter 2 is not very suitable for urban terrain, because the different surface types within a city are not as clearly defined as for agricultural fields. Therefore, modeled footprints from eddy-covariance data obtained over a well-defined urban area should be compared with the flux footprint within an LES of a similar case. The comparison of an analytical footprint model applied to data observed over a semi-arid shrub area, with an LES with a very high resolution close to the surface, presented in Leclerc et al. (1997) and in Steinfeld et al. (2008), could be taken as examples to study the feasibility of current footprint models for urban areas. LES studies for urban areas are already performed since the study by Liu and Barth (2002).

As discussed in Chapter 4, routinely observed surface-flux data are scarce. This especially holds for data observed over urban terrain. Therefore, we propose to make the scheme presented in Chapter 4 applicable to urban areas. Heat fluxes over an urban area could then be estimated from single-level weather station data, provided that incoming shortwave radiation is measured somewhere close by. These parameters could be obtained from weather stations installed on roof tops of the highest buildings. Bicycle traverse measurements through a city, e.g. by Heusinkveld et al. (2014), might be used as well. However, these measurements are taken within the roughness sublayer, where the wind profile does not correspond with Monin-Obukhov similarity theory. The aerodynamic resistance calculation should therefore be adjusted for the vertical wind profile observed between the buildings as described for vegetative canopies in Harman and Finnigan (2007). As a first test, weather data observed over a non-green district from a dry period should be used, such that the latent-heat flux can be neglected in the scheme. The only other required adjustments to the scheme, are the 'surface' heat transfer coefficient A_g , which is much higher compared to a well-watered soil, and the albedo α , which is much lower compared to a crop (Schubert and Grossman-Clarke, 2014). To validate the scheme for urban areas, the heat fluxes obtained from the scheme should be compared with flux data from an eddy-covariance station on top of a high building, or with scintillometer data obtained over an urban area.

6.6 Measurement campaigns

The BLLAST measurement campaign involved many different institutes. Thereby, we came across different possibilities to install the gas analyzer in the eddy-covariance mast, considering the orientation and the distance to the sonic anemometer. The larger the distance between the anemometer and the gas analyzer, the longer an air parcel needs to travel from one to the other (for the same wind speed and direction). A longer travel time means a larger time lag between the anemometer signal and the gas analyzer signal, and less accuracy in the derived flux. To minimize this time lag, the gas analyzer can be installed right below, above, or next to the anemometer. Furthermore, these configurations will have a different impact on the wind field that is measured by the anemometer. A comparison of turbulence statistics obtained with eddy-covariance stations with different configurations should be done, to investigate the effect of the configuration of the sonic anemometer and the gas analyzer on turbulence measurements. To avoid that small-scale surface heterogeneity causes differences in the observations, an extremely homogeneous and flat area (e.g. a salt plain) should be chosen for this comparison study. Also, identical instruments should be used, and the gas analyzers should all be calibrated right before the start of the comparison period.

When planning a campaign for studying atmospheric turbulence over a vegetated area, we recommend to also study the vegetation in detail. In order to simulate or explain observed atmospheric turbulence, the surroundings of the study site should be mapped carefully. Especially in a heterogeneous area, the different land-use types should be mapped at an accuracy of a few meters, for applying a footprint model. Surface heterogeneity within one land-use type should be observed as well. This could be done using an infra-red camera, installed in a mast or under a small unmanned air craft or multicopter. In case of developing crops, weekly measurements of the *LAI* and the canopy height of the different land-use types should be taken. Continuous observations of soil moisture content and soil respiration should be performed as well. From our studies on the BLLAST data, we learned that a mountain ridge within 50 km from the measurement site strongly influences the wind climatology, which should be taken into account for studying atmospheric turbulence.

Furthermore, we recommend to further invest in obtaining surface fluxes without the use of eddy-covariance. In many agricultural areas in the world there are no resources available to install an eddy-covariance station, whereas it is especially necessary for such areas to study for example the water usage of a certain crop. Also, the more spatial flux estimates can be made, the better remote sensing products (e.g. vegetation development) could be validated, for fine-tuning larger-scale models. The from-weather-to-fluxes approach discussed in this thesis would be suited for estimating evapotranspiration in remote areas. Currently, the FAO (Food and Agriculture Organization of the United Nations) estimates evapotranspiration from meteorological data and empirical crop coefficients by a simplified version of the

Penman-Monteith equation (Allen et al., 1998). Our approach requires the same input, but works with less assumptions and generalizations to obtain the surface fluxes over a certain crop. Furthermore, our approach is adjustable to distinguish the physiology of C3 and C4 plants, as we use the canopy resistance, which is higher for a C4 plant to limit the loss of water vapor.

References

- Allen, R., Pereira, L., Raes, D., and Smith, M.: Crop evapotranspiration: guidelines for computing crop water requirements, FAO Irrigation and drainage paper no. 56. Rome, Italy, 56, 1–174, 1998.
- Amthor, J. S. and Baldocchi, D. D.: Terrestrial Higher-Plant Respiration and Net Primary Production. In: Terrestrial Global Productivity: Past, Present and Future. Eds. J. Roy, B. Saugier and H. Mooney, Academic Press San Diego, 2001.
- Andreas, E. L.: Estimating C_{r2} over snow and sea ice from meteorological data, *J Opt Soc Am*, 5A, 481–495, 1988.
- Angevine, W. M.: Transitional, entraining, cloudy, and coastal boundary layers, *Acta Geophys*, 56, 2–20, 2008.
- Baldocchi, D., Falge, E., Gu, L., Olson, R., Hollinger, D., Running, S., Anthoni, P., Bernhofer, C., Davis, K., Evans, R., Fuentes, J., Goldstein, A., Katul, G., Law, B., Lee, X., Malhi, Y., Meyers, T., Munger, W., Oechel, W., Paw, K. T., Pilegaard, K., Schmid, H. P., Valentini, R., Verma, S., Vesala, T., Wilson, K., and Wofsy, S.: FLUXNET: A new tool to study the temporal and spatial variability of ecosystem-scale carbon dioxide, water vapor, and energy flux densities, *B Am Meteorol Soc*, 82, 2415–2434, 2001.
- Beljaars, A. and Bosveld, F. C.: Cabauw data for the validation of land surface parameterization schemes, *J Climate*, 10, 1172–1193, 1997.
- Bendersky, S., Kopeika, N. S., and Blaunstein, N.: Atmospheric optical turbulence over land in middle east coastal environments: prediction modeling and measurements., *Appl Opt*, 43, 4070–4079, 2004.
- Betts, A. K.: FIFE atmospheric boundary layer budget methods, *J Geophys Res*, 97, 18 523–18 531, 1992.
- Betts, A. K. and Beljaars, A. C.: Estimation of effective roughness length for heat and momentum from FIFE data, *Atmos Res*, 30, 251–261, 1993.
- Boast, C. W. and Robertson, T. M.: A micro-lysimeter method for determining evaporation from bare soil: description and laboratory evaluation, *Soil Sci Soc America J*, 46, 689–696, 1982.
- Bosveld, F. C., van der Vliet, J. C., and Monna, W. A. A.: The KNMI Garderen experiment: micro-meteorological observations 1988-1989, instruments and data set, 1998.
- Braam, M., Bosveld, F. C., and Moene, A. F.: On Monin-Obukhov scaling in and above the atmospheric surface-layer: the complexities of elevated scintillometer measurements, *Bound-Layer Meteorol*, 144, 157–177, 2012.
- Brutsaert, W.: Evaporation into the Atmosphere: Theory, History, and Applications, 1982.
- Canut, G., Lothon, M., Saïd, F., and Lohou, F.: Observation of entrainment at the interface between monsoon flow and the Saharan Air Layer, *Q J R Meteorol Soc*, 136, 34–46, 2010.
- Cheinet, S. and Cumin, P.: Local structure parameters of temperature and humidity in the entrainment-drying convective boundary layer: a large-eddy simulation analysis, *J Appl Meteor Climatol*, 50, 472–481, 2011.
- Chen, F. and Dudhia, J.: Coupling an advanced land surface-hydrology model with the Penn State-NCAR MM5 modeling system. Part I: Model implementation and sensitivity, *Mon Wea Rev*, 129, 569–585, 2001.
- Couvreux, F., Guichard, F., Masson, V., and Redelsperger, J.-L.: Negative water vapour skewness and dry tongues in the convective boundary layer: observations and large-eddy simulation budget analysis, *Bound-Layer Meteorol*, 123, 269–294, 2007.

- Crawford, T. M. and Duchon, C. E.: An improved parameterization for estimating effective atmospheric emissivity for use in calculating daytime downwelling longwave radiation, *J Appl Meteorol*, 38, 474–480, 1999.
- Cuxart, J., Morales, G., and Terradellas, E.: Pressure transport terms for the nocturnal stable boundary layer, *Bound-Layer Meteorol*, 105, 305–328, 2002.
- Davidson, K. L., Houlihan, T. M., Fairall, C. W., and Schacher, G. E.: Observation of the temperature structure function parameter, C_{T^2} , over the ocean, *Bound-Layer Meteorol*, 15, 507–523, 1978.
- de Arellano, J. V.-G.: Entrainment process of carbon dioxide in the atmospheric boundary layer, *J Geophys Res*, 109, 1–15, 2004.
- De Bruin, H., van den Hurk, B. J. J. M., and Kroon, L. J. M.: On the temperature-humidity correlation and similarity, *Bound-Layer Meteorol*, 93, 453–468, 1999.
- De Bruin, H. A. R., Kohsiek, W., and van den Hurk, B. J. J. M.: A verification of some methods to determine the fluxes of momentum, sensible heat, and water vapour using standard deviation and structure parameter of scalar meteorological quantities, *Bound-Layer Meteorol*, 63, 231–257, 1993.
- De Moortel, I., Munday, S., and Hood, A.: Wavelet Analysis: the effect of varying basic wavelet parameters, *Solar Phys*, 222, 203–228, 2004.
- de Rooy, W. C. and Holtslag, A. A. M.: Estimation of surface radiation and energy flux densities from single-level weather data, *J Appl Meteorol*, 38, 526–540, 1999.
- Deardorff, J.: Cloud top entrainment instability, *J Atmos Sci*, 37, 131–147, 1980.
- Detto, M., Montaldo, N., Albertson, J. D., Mancini, M., and Katul, G.: Soil moisture and vegetation controls on evapotranspiration in a heterogeneous Mediterranean ecosystem on Sardinia, Italy, *Water Resour Res*, 42, 1–16, 2006.
- Farge, M., Kevlahan, N., Perrier, V., and Goirand, E.: Wavelets and Turbulence, *Proc IEEE*, 84, 639–669, 1996.
- Foken, T. and Leclerc, M.: Methods and limitations in validation of footprint models, *Agric Forest Meteorol*, 127, 223–234, 2004.
- Friehe, C. A.: Estimation of the refractive-index temperature structure parameter over the ocean., *App Opt*, 16, 334–340, 1977.
- Gash, J.: A note on estimating the effect of a limited fetch on micrometeorological evaporation measurements, *Bound-Layer Meteorol*, 35, 409–413, 1986.
- Göckede, M., Markkanen, T., Mauder, M., Arnold, K., Leps, J.-P., and Foken, T.: Validation of footprint models using natural tracer measurements from a field experiment, *Agric Forest Meteorol*, 135, 314–325, 2005.
- Graf, A., Schüttemeyer, D., Geiß, H., Knaps, A., Möllmann-Coers, M., Schween, J. H., Kollet, S., Neininger, B., Herbst, M., and Vereecken, H.: Boundedness of turbulent temperature probability distributions, and their relation to the vertical profile in the convective boundary layer, *Bound-Layer Meteorol*, 134, 459–486, 2010.
- Graf, A., Prolingheuer, N., Schickling, A., Schmidt, M., Schneider, K., Schüttemeyer, D., Herbst, M., Huisman, J. A., Weihermüller, L., Scharnagl, B., Steenpass, C., Harms, R., and Vereecken, H.: Temporal downscaling of soil carbon dioxide efflux measurements based on time-stable spatial patterns, *Vadose Zone J*, 10, 239, 2011.
- Graf, A., van de Boer, A., Moene, A. F., and Vereecken, H.: Intercomparison of methods for the simultaneous estimation of zero-plane displacement and aerodynamic roughness length from single-level eddy-covariance, *Bound-Layer Meteorol*, 151, 373–387, 2014.
- Haenel, H.-D. and Grünhage, L.: Footprint analysis: a closed analytical solution based on height-dependent profiles of wind speed and eddy viscosity, *Bound-Layer Meteorol*, pp. 395–409, 1999.
- Hägeli, P., Steyn, D., and Strawbridge, K.: Spatial and temporal variability of mixed-layer depth and entrainment zone thickness, *Bound-Layer Meteorol*, 97, 47–71, 2000.
- Harman, I. N. and Finnigan, J. J.: A simple unified theory for flow in the canopy and roughness sublayer, *Bound-Layer Meteorol*, 123, 339–363, 2007.

-
- Heus, T., van Heerwaarden, C. C., Jonker, H. J. J., Pier Siebesma, A., Axelsen, S., van den Dries, K., Geoffroy, O., Moene, a. F., Pino, D., de Roode, S. R., and Vilà-Guerau de Arellano, J.: Formulation of the Dutch Atmospheric Large-Eddy Simulation (DALES) and overview of its applications, *Geosci Model Dev*, 3, 415–444, 2010.
- Heusinkveld, B. G., Steeneveld, G. J., van Hove, L. W. A., Jacobs, C. M. J., and Holtslag, A. A. M.: Spatial variability of the Rotterdam urban heat island as influenced by urban land use, *J Geophys Res: Atmos*, 119, 677–692, 2014.
- Hill, R. J.: Review of optical scintillation methods of measuring the refractive-index spectrum, inner scale and surface fluxes, *Waves in Random Media*, 2, 179–201, 1992.
- Hill, R. J. and Clifford, S. F.: Modified spectrum of atmospheric temperature fluctuations and its application to optical propagation, *J Opt Soc Am*, 68, 892–899, 1978.
- Högström, U.: Review of some basic characteristics of the atmospheric surface layer, *Bound-Layer Meteorol*, 78, 215–246, 1996.
- Holtslag, A. and van Ulden, A.: A simple scheme for daytime estimates of the surface fluxes from routine weather data, *J Clim Appl Meteorol*, 22, 517–529, 1983.
- Horst, T. and Weil, J.: Footprint estimation for scalar flux measurements in the atmospheric surface layer, *Bound-Layer Meteorol*, pp. 279–296, 1992.
- Horst, T. W.: The footprint for estimation of atmosphere-surface exchange fluxes by profile techniques, *Bound-Layer Meteorol*, pp. 171–188, 1999.
- Hsieh, C., Katul, G., and Chi, T.-w.: An approximate analytical model for footprint estimation of scalar fluxes in thermally stratified atmospheric flows, *Adv Water Resour*, 23, 765–772, 2000.
- Hudgins, L., Friehe, C. A., and Mayer, M.: Wavelet transforms and atmospheric turbulence, *Phys Lett*, 71, 3279–3283, 1993.
- Hutjes, R., Vellinga, O., Gioli, B., and Miglietta, F.: Dis-aggregation of airborne flux measurements using footprint analysis, *Agric Forest Meteorol*, 150, 966–983, 2010.
- Idso, S. B.: A set of equations for full spectrum and 8 to 14 μm and 10.5 to 12.5 μm thermal radiation from cloudless skies, *Water Resour Res*, 17, 295–304, 1981.
- Jacobs, C. M. J. and De Bruin, H. A. R.: The sensitivity of regional transpiration to land-surface characteristics: significance of feedback, *J Climate*, 5, 683–698, 1992.
- Jarvis, P. G.: The interpretation of the variations in leaf water potential and stomatal conductance found in canopies in the field, *Philos Trans Roy Soc Lond B, Biol Sci*, 273, 593–610, 1976.
- Kaimal, J. C., Wyngaard, J. C., Izumi, Y., and Coté, O. R.: Spectral characteristics of surface-layer turbulence, *Q J R Meteorol Soc*, 98, 563–589, 1972.
- Kasten, F. and Czeplak, G.: Solar and terrestrial radiation dependent on the amount and type of cloud, *Solar Energy*, 24, 177–189, 1980.
- Katul, G. G., Sempreviva, A. M., and Cava, D.: The temperature-humidity covariance in the marine surface layer: a one-dimensional analytical model, *Bound-Layer Meteorol*, 126, 263–278, 2008.
- Kimmel, S. J., Wyngaard, J. C., and Otte, M. J.: ‘Log-Chipper’ turbulence in the convective boundary layer, *J Atmos Sci*, 59, 1124–1134, 2002.
- Kljun, N., Rotach, M. W., and Schmid, H. P.: A three-dimensional backward lagrangian footprint model for a wide range of boundary-layer stratifications, *Bound-Layer Meteorol*, 103, 205–226, 2002.
- Kljun, N., Kormann, R., Rotach, M., and Meixner, F.: Comparison of the langrangian footprint model LPDM-B with an analytical footprint model, *Bound-Layer Meteorol*, 106, 349–355, 2003.
- Kljun, N., Calanca, P., Rotach, M. W., and Schmid, H. P.: A simple parameterisation for flux footprint predictions, *Bound-Layer Meteorol*, 112, 503–523, 2004.
- Kooijmans, L. M. J.: Testing the universality of Monin-Obukhov similarity functions, 2013.
- Kormann, R. and Meixner, F. X.: An analytical footprint model for non-neutral stratification, *Bound-Layer Meteorol*, 99, 207–224, 2001.

- Kotthaus, S. and Grimmond, C.: Identification of Micro-scale Anthropogenic CO₂, heat and moisture sources - Processing eddy covariance fluxes for a dense urban environment, *Atmos Environ*, 57, 301–316, 2012.
- Lauer, M. J. and Boyer, J. S.: Internal CO₂ measured directly in leaves : abscisic acid and low leaf water potential cause opposing effects., *Plant physiology*, 98, 1310–6, 1992.
- Leclerc, M. Y. and Foken, T.: *Footprints in Micrometeorology and Ecology*, Springer Berlin Heidelberg, Berlin, Heidelberg, 2014.
- Leclerc, M. Y., Shen, S., and Lamb, B.: Observations and large-eddy simulation modeling of footprints in the lower convective boundary layer, *J Geophys Res*, 102, 9323, 1997.
- Lenschow, D. H., Wulfmeyer, V., and Senff, C.: Measuring second- through fourth-order moments in noisy data, *J Atmos Oceanic Tech*, 17, 1330–1347, 2000.
- Li, D., Bou-Zeid, E., and De Bruin, H. A. R.: Monin-Obukhov similarity functions for the structure parameters of temperature and humidity, *Bound-Layer Meteor*, 145, 45–67, 2012.
- Liu, C.-H. and Barth, M. C.: Large-eddy simulation of flow and scalar transport in a modeled street canyon, *J Appl Meteorol*, 41, 660–673, 2002.
- Lohou, F., Saïd, F., Lothon, M., Durand, P., and Serça, D.: Impact of boundary-layer processes on near-surface turbulence within the West African Monsoon, *Bound-Layer Meteor*, 136, 1–23, 2010.
- Long, S., Farage, P., and Garcia, R.: Measurement of leaf and canopy photosynthetic CO₂ exchange in the field, *J Exp Botany*, 47, 1629–1642, 1996.
- Lothon, M., Couvreux, F., Donier, S., Guichard, F., Lacarrère, P., Lenschow, D. H., Noilhan, J., and Saïd, F.: Impact of coherent eddies on airborne measurements of vertical turbulent fluxes, *Bound-Layer Meteor*, 124, 425–447, 2007.
- Lothon, M., Couvreux, F., Durand, P., Hartogensis, O., Legain, D., Lohou, F., Pardyjak, E. R., Pino, D., Reuder, J., Vilà-Guerau de Arellano, J., Alexander, D., Augustin, P., Bargain, E., Barrié, J., Bazile, E., Bezombes, Y., Blay-Carreras, E., van de Boer, A., Boichard, J. L., de Coster, O., Cuxart, J., Dabas, A., Darbieu, C., Deboudt, K., Delbarre, H., Derrien, S., Faloona, I., Flamant, P., Fourmentin, M., Garai, A., Gibert, F., Gioli, B., Graf, A., Groebner, J., Guichard, F., Jonassen, M., van den Kroonenberg, A. Lenschow, D., Martin, S., Martinez, D., Mastroiello, L., Moene, A. F., Molinos, F., Moulin, E., Pietersen, H., Piguet, B., Pique, E., Román-Gascón, C., Saïd, F., Sastre, M., Seity, Y., Steeneveld, G. J., Toscano, P., Traullé, O., Tzanos, D., Yagüe, C., Wacker, S., Wildmann, N., and Zaldei, A.: The boundary layer late afternoon and sunset turbulence 2011 field experiment, in: *20th Symposium on Boundary Layers and Turbulence/18th Conference on Air-Sea Interaction*, Boston, Massachusetts, USA, 13 July 2012, 14B.1, 2012.
- Mahrt, L.: Boundary-layer moisture regimes, *Q J R Meteorol Soc*, 117, 151–176, 1991.
- Mahrt, L.: Computing turbulent fluxes near the surface: Needed improvements, *Agric Forest Meteorol*, 150, 501–509, 2010.
- Mahrt, L. and Park, S.-U.: The influence of boundary layer pumping on synoptic-scale flow, *J Atmos Sci*, 33, 1505–1520, 1976.
- Maronga, B.: Monin-Obukhov similarity functions for the structure parameters of temperature and humidity in the unstable surface layer: results from high-resolution large-eddy simulations, *J Atmos Sci*, 71, 716â–733, 2013.
- Mauder, M., Desjardins, R. L., Oncley, S. P., and MacPherson, I.: Atmospheric Response to a Partial Solar Eclipse over a Cotton Field in Central California, *J Appl Meteorol Climatol*, 46, 1792–1803, 2007.
- Metzger, S., Junkermann, W., Mauder, M., Beyrich, F., Butterbach-Bahl, K., Schmid, H. P., and Foken, T.: Eddy-covariance flux measurements with a weight-shift microlight aircraft, *Atmos Measurement Techniques*, 5, 1699–1717, 2012.
- Michels, B. I. and Jochum, A. M.: Heat and moisture flux profiles in a region with inhomogeneous surface evaporation, *J Hydrol*, 166, 383–407, 1995.
- Moene, A. F.: Effects of water vapour on the structure parameter of the refractive index for near-infrared radiation, *Bound-Layer Meteor*, 107, 635–653, 2003.
- Moene, A. F. and Schüttemeyer, D.: The effect of surface heterogeneity on the temperature-humidity correlation and the relative transport efficiency, *Bound-Layer Meteor*, 129, 99–113, 2008.

-
- Moene, A. F. and van Dam, J. C.: Transport in the atmosphere-vegetation-soil continuum, Cambridge University Press, New York, USA, 2014.
- Moene, A. F., Michels, B. I., and Holtslag, A. A. M.: Scaling variances of scalars in a convective boundary layer under different entrainment regimes, *Bound-Layer Meteorol*, 120, 257–274, 2006.
- Moeng, C.-H. and Wyngaard, J. C.: Evaluation of turbulent transport and dissipation closures in second-order modeling, *Am Meteorol Soc*, 46, 2311–2330, 1989.
- Monin, A. S. and Obukhov, A. M.: Basic laws of turbulent mixing in the surface layer of the atmosphere, *Trudy geofiz inst AN SSSR*, 24, 163–187, 1954.
- Neftel, A., Spirig, C., and Ammann, C.: Application and test of a simple tool for operational footprint evaluations., *Environ pollution*, 152, 644–52, 2008.
- Obukhov, A. M.: Turbulence in an atmosphere with a non-uniform temperature, *Trudy Inst Theor Geofiz AN SSSR*, 1, 95–115, 1946.
- Ogunjemiyo, S. O., Kaharabata, S. K., Schuepp, P. H., MacPherson, I. J., Desjardins, R., and Roberts, D. a.: Methods of estimating CO₂, latent heat and sensible heat fluxes from estimates of land cover fractions in the flux footprint, *Agric Forest Meteorol*, 117, 125–144, 2003.
- Oncley, S. P., Friehe, C. A., Larue, J. C., Businger, J. A., Itsweire, E. C., and Chang, S. S.: Surface-layer fluxes, profiles, and turbulence measurements over uniform terrain under near-neutral conditions, *J Atmos Sci*, 53, 1029–1044, 1996.
- Ouwensloot, H. G., Vilà-Guerau de Arellano, J., van Heerwaarden, C. C., Ganzeveld, L. N., Krol, M. C., and Lelieveld, J.: On the segregation of chemical species in a clear boundary layer over heterogeneous land surfaces, *Atmos Chem Phys*, 11, 10 681–10 704, 2011.
- Palatella, L., Rana, G., and Vitale, D.: Towards a flux-partitioning procedure based on the direct use of high-frequency eddy-covariance data, *Bound-Layer Meteorol*, 153, 327–337, 2014.
- Paltridge, G. W. and Platt, C. M. R.: Radiative processes in meteorology and climatology, Amsterdam-Oxford-New York, Elsevier Scientific Publishing Company, 1976.
- Pasquill, F.: Some aspects of boundary layer description, *Q J R Meteorol Soc*, 98, 469–494, 1972.
- Patton, E. G., Sullivan, P. P., and Davis, K. J.: The influence of a forest canopy on top-down and bottom-up diffusion in the planetary boundary layer, *Q J R Meteorol Soc*, 129, 1415–1434, 2003.
- Paulson, C. A.: The mathematical representation of wind speed and temperature profiles in the unstable atmospheric surface layer, *J Appl Meteorol*, 9, 857–861, 1970.
- Pino, D., Vilà-Guerau de Arellano, J., and Duynkerke, P. G.: The contribution of shear to the evolution of a convective boundary layer, *J Atmos Sci*, 60, 1913–1926, 2003.
- Rachele, H. and Tunick, A.: Energy balance model for imagery and electromagnetic propagation, *J Appl Meteorol*, 33, 964–976, 1994.
- Reth, S., Göckede, M., and Falge, E.: CO₂ efflux from agricultural soils in Eastern Germany - comparison of a closed chamber system with eddy covariance measurements, *Theor Appl Climatol*, 80, 105–120, 2005.
- Ronda, R. J., de Bruin, H. A. R., and Holtslag, A. A. M.: Representation of the canopy conductance in modeling the surface energy budget for low vegetation, *J Appl Meteorol*, 40, 1431–1444, 2001.
- Rouse, W. R.: Microclimate at Arctic tree line 3. The effects of regional advection on the surface energy balance of upland tundra, *Water Resour Res*, 20, 74–78, 1984.
- Sadot, D. and Kopeika, N. S.: Forecasting optical turbulence strength on the basis of macroscale meteorology and aerosols : models and validation, *Opt Eng*, 31, 200–212, 1992.
- Scanlon, T. M. and Kustas, W. P.: Partitioning carbon dioxide and water vapor fluxes using correlation analysis, *Agric Forest Meteorol*, 150, 89–99, 2010.
- Scanlon, T. M. and Sahu, P.: On the correlation structure of water vapor and carbon dioxide in the atmospheric surface layer: A basis for flux partitioning, *Water Resour Res*, 44, 1–15, 2008.
- Schmid, H.: Source areas for scalars and scalar fluxes, *Bound-Layer Meteorol*, 67, 293–318, 1994.

- Schmid, H.: On the Do's and Dont's of footprint analysis in difficult conditions., in: iLEAPS Specialist Workshop, iLEAPS Specialist Workshop Flux Measurements in difficult conditions, Boulder, USA, 2006.
- Schmid, H. and Oke, T. R.: A model to estimate the source area contributing to turbulent exchange in the surface layer over patchy terrain, *Q J R Meteorol Soc*, pp. 965–988, 1990.
- Schmid, H. P.: Footprint modeling for vegetation atmosphere exchange studies : a review and perspective, *Science*, **113**, 159–183, 2002.
- Schotanus, P., Nieuwstadt, F., and de Bruin, H.: Temperature measurement with a sonic anemometer and its application to heat and moisture fluxes, *Bound-Layer Meteor*, **26**, 81–93, 1983.
- Schubert, S. and Grossman-Clarke, S.: Evaluation of the coupled COSMO-CLM/DCEP model with observations from BUBBLE, *Q J R Meteorol Soc*, 2014.
- Schuepp, P., Leclerc, M., Macpherson, J., and Desjardins, R.: Footprint prediction of scalar fluxes from analytical solutions of the diffusion equation, *Bound-Layer Meteor*, **50**, 355–373, 1990.
- Sempreviva, A. M. and Gryning, S.-E.: Mixing height over water and its role on the correlation between temperature and humidity fluctuations in the unstable surface layer, *Bound-Layer Meteor*, **97**, 273–291, 2000.
- Sempreviva, A. M. and Højstrup, J. r.: Transport of temperature and humidity variance and covariance in the marine surface layer, *Bound-Layer Meteor*, **87**, 233–253, 1998.
- Sivasligil, M., Erol, C. B., Polat, O. M., and Sari, H.: Validation of refractive index structure parameter estimation for certain infrared bands, *Appl Opt*, **52**, 3127–3133, 2013.
- Sorbjan, Z.: Effects caused by varying the strength of the capping inversion based on a large eddy simulation model of the shear-free convective boundary layer, *J Atmos Sci*, **53**, 2015–2024, 1996.
- Spena, A., D'Angiolini, G., and Strati, C.: First correlations for solar radiation on cloudy days in Italy, in: ASME-ATI-UIT 2010 Conference on Thermal and Environmental Issues in Energy Systems, Sorrento, Italy, may 2010, 2010.
- Stannard, D. I.: A theoretically based determination of bowen-ratio fetch requirements, *Bound-Layer Meteor*, pp. 375–406, 1997.
- Steinfeld, G., Raasch, S., and Markkanen, T.: Footprints in homogeneously and heterogeneously driven boundary layers derived from a Lagrangian stochastic particle model embedded into Large-Eddy Simulation, *Bound-Layer Meteor*, **129**, 225–248, 2008.
- Stewart, J. and Gay, L.: Preliminary modelling of transpiration from the fife site in Kansas, *Agric Forest Meteorol*, **48**, 305–315, 1989.
- Stewart, J. B.: Modelling surface conductance of pine forest, *Agric Forest Meteorol*, **43**, 19–35, 1988.
- Swanson, R. H.: Significant historical developments in thermal methods for measuring sap flow in trees, *Agric Forest Meteorol*, **72**, 113–132, 1994.
- Tapper, N. J.: Urban influences on boundary layer temperature and humidity: results from Christchurch, New Zealand, *Atmos Environ*, **24B**, 19–27, 1990.
- Terradellas, E., Morales, G., Cuxart, J., and Yagüe, C.: Wavelet methods: application to the study of the stable atmospheric boundary layer under non-stationary conditions, *Dyn Atmos Oceans*, **34**, 225–244, 2001.
- Thiermann, V. and Grassl, H.: The measurement of turbulent surface-layer fluxes by use of bichromatic scintillation, *Bound-Layer Meteor*, **58**, 367–389, 1992.
- Tunick, A.: A critical assessment of selected past research on optical turbulence information in diverse microclimates, *Tech. rep.*, Army Research Laboratory, 2002.
- Twine, T. E., Kustas, W. P., Norman, J. M., Cook, D. R., Houser, P., Meyers, T. P., Prueger, J. H., Starks, P. J., and Wesely, M. L.: Correcting eddy-covariance flux underestimates over a grassland, *Agric Forest Meteorol*, **103**, 279–300, 2000.
- van de Boer, A., Moene, A. F., and Schuettmeyer, D.: Sensitivity and uncertainty of analytical footprint models according to a combined natural tracer and ensemble approach, *Agric For Meteorol*, **169**, 1–11, 2013.

-
- van de Boer, A., Moene, A. F., Graf, A., Schüttemeyer, D., and Simmer, C.: Detection of entrainment influences on surface-layer measurements and extension of Monin-Obukhov similarity theory, *Bound-Layer Meteorol*, 152, 19–44, 2014a.
- van de Boer, A., Moene, A. F., Graf, A., Simmer, C., and Holtslag, A. A. M.: Estimation of the refractive index structure parameter from single-level daytime routine weather data, *Appl Opt*, 53, 5944–5960, 2014b.
- van Dijk, A., Moene, A. F., and de Bruin, H. A. R.: The principles of surface flux physics : theory , practice and description of the ECPACK library, Internal Report 2004/1, Meteorology and Air Quality Group, Wageningen University, Wageningen, the Netherlands, p. 99 pp., 2004.
- Vilà Guerau de Arellano, J., Duynkerke, P. G., and Zeller, K.: Atmospheric surface layer similarity theory applied to chemically reactive species, *J Geophys Res*, 100, 1397–1408, 1995.
- Waldhoff, G.: Land use classification of 2009 for the Rur catchment, 2010.
- Ward, H. C., Evans, J. G., Hartogensis, O. K., Moene, A. F., De Bruin, H. A. R., and Grimmond, C. S. B.: A critical revision of the estimation of the latent heat flux from two-wavelength scintillometry, *Q J R Meteorol Soc*, 139, 1912–1922, 2013.
- Webb, E., Pearman, G., and Leuning, R.: Correction of flux measurements for density effects due to heat and water vapour transfer, *Q J R Meteorol Soc*, 106, 85–100, 1980.
- Wesely, M. L.: The combined effect of temperature and humidity fluctuations on refractive index, *J Appl Meteorol*, 15, 43–49, 1976.
- Wilczak, J. M., Oncley, S. P., and Stage, S. A.: Sonic anemometer tilt correction algorithms, *Bound-Layer Meteorol*, 99, 127–150, 2001.
- Willmer, C. and Fricker, M.: *Stomata*, Springer Science & Business Media, 1996.
- Wyngaard, J. C. and Clifford, S. F.: Taylor’s hypothesis and high-frequency turbulence spectra, *J Atmos Sci*, 34, 922–928, 1977.
- Wyngaard, J. C., Coté, O. R., and Izumi, Y.: Local free convection, similarity, and the budgets of shear stress and heat flux, *J Atmos Sci*, 28, 1171–1182, 1971.
- Zundel, G., Miekeley, W., Grisi, B. M., and Firstel, H.: The H_2^{18}O enrichment in the leaf water of tropic trees: Comparison of species from the tropical rain forest and the semi-arid region in Brazil, *Radiation Environ Biophys*, 15, 203–212, 1978.

Samenvatting

Atmosferische turbulentie is het onregelmatig bewegen van lucht. In de grenslaag, de luchtslaag die direct door het aardoppervlak beïnvloed wordt, ontstaat turbulentie overdag door opwarming van lucht nabij het aardoppervlak en door wrijving van de luchtstroom met het aardoppervlak. 's Nachts speelt alleen wrijving een rol. De nachtelijke grenslaag is daardoor vele malen dunner. In Figuur 1.1 illustreren we dat turbulente luchtwervels, *eddies*, zorgen voor het verspreiden van onder andere vocht, warmte en CO₂.

De mate van turbulent transport hangt vooral af van de vochtigheid en ruwheid van het oppervlak en van de hoeveelheid niet-weerkaatste stralingsenergie. Atmosferische turbulentie-gegevens bevatten dus informatie over de interacties en processen die in de bodem en vegetatie plaatsvinden. Deze land-atmosfeer interacties, en zo atmosferisch transport, hebben een grote invloed op onder andere het weer en klimaat.

Turbulent transport is chaotisch, en daarom ingewikkeld na te bootsen in een model. Vereenvoudigde modellen worden gebruikt voor het simuleren van vocht-, warmte- en CO₂-uitwisseling in de oppervlaktelaag, de onderste laag van de grenslaag zoals weergegeven in Figuur 1.1. Daarbij worden de variabelen statistisch uitgedrukt. De mate waarin bijvoorbeeld de vochtconcentratie op de tijdschaal van secondes varieert, de vochtvariantie, zegt iets over hoe turbulent de atmosfeer is. Maar in hoeverre zijn deze benaderingen voor de interacties tussen land en atmosfeer geldig? En kunnen we bestaande theorieën uitbreiden zodat ze geldig zijn voor meerdere situaties?

We hebben vier bestaande theorieën onderzocht die allen een gedeelte beschrijven van de interactie tussen de bodem, vegetatie en atmosfeer. Door deze theorieën te toetsen met waarnemingen van uitwisselingen van vocht, warmte en CO₂ boven verscheidene gewassen, kunnen we iets zeggen over de toepasbaarheid. Ook kunnen we de theorieën zo eventueel verbeteren. Dit helpt andere onderzoekers onder meer bij het simuleren van water-beschikbaarheid, gewasgroei, en het klimaat, wat weer belangrijk is voor bijvoorbeeld voedselproductie en gezondheid wereldwijd.

De getoetste theorieën beschrijven, in volgorde van dit proefschrift:

- de grootte en vorm van het gebied dat invloed heeft op een puntmeting van atmosferisch transport in de oppervlaktelaag

- een verband tussen de hoeveelheid vochtuitwisseling aan het aardoppervlak, en de vochtvariantie in de oppervlaktelaag
- een relatie tussen een aantal weer-parameters, en uitwisseling van warmte en vocht aan het aardoppervlak
- samenhang tussen statistische vocht- en CO₂-gegevens, en de aandelen bodemverdamping en plant-transpiratie in uitwisseling van vocht en CO₂

Om de theorieën te testen en te verbeteren, hebben we ze toegepast, en de uitkomsten vergeleken met transportmetingen. Deze waarnemingen zijn verzameld door zogenoemde 'eddycovariantiesystemen'. Zo'n systeem meet minstens 10 keer per seconde de doorstroming van bijvoorbeeld CO₂-deeltjes, in alle richtingen. Door zo vaak te meten, kan men de turbulente luchtbewegingen statistisch benaderen en bepalen wat het gemiddelde transport is. Een eddycovariantiemeting zegt daarmee iets over de uitwisselingen op veldschaal.

Eddycovariantiesystemen zijn duur en onderhoudsgevoelig, waardoor ze niet standaard op meteorologische stations staan. Toch stond in 2005 een systeem geïnstalleerd op het meteorologisch station 'de Haarweg' in Wageningen. Deze uitwisselingswaarnemingen hebben we gebruikt voor ons onderzoek naar een relatie tussen weer-parameters en uitwisseling van warmte en vocht aan dit grasoppervlak. Voor het onderzoeken van andere gewastypen en voor de andere onderzoeksvragen, hebben wij metingen gebruikt van twee meetcampagnes, waarbij enkele eddycovariantiesystemen tijdelijk werden opgesteld.

In 2009 vond een intensieve meetcampagne plaats in een landbouwgebied tussen Aken en Keulen, in Merken, Duitsland. Verscheidene onderzoekers hebben daar gedurende het groeiseizoen vooral gemeten aan de bodems en de gewassen, maar ook aan de atmosfeer. Er stond een eddycovariantiestation in een suikerbietenveld, een aangrenzend graanveld, en in een aangrenzend gerstveld.

In juni 2011 hebben we deelgenomen aan een campagne in Zuid-Frankrijk, waarbij de nadruk op atmosferische metingen lag. Ongeveer 100 km ten zuidwesten van Toulouse, bij een observatorium in Lannemezan, hadden we onder andere eddycovariantiestations geïnstalleerd in een graanveld en in een aangrenzend grasveld. Vooral op zonnige dagen werden bovendien veel weerballonnen opgelaten en vliegtuigvluchten gemaakt om temperatuur, vocht, en wind boven de grenslaag te meten.

Wanneer de interacties tussen bodem, vegetatie en atmosfeer onderzocht worden met behulp van gemeten luchtbewegingen vlak boven het oppervlak, is het zeer belangrijk te weten welk deel van het oppervlak precies invloed had op de transportmeting. Als bijvoorbeeld een groot opwaarts vochttransport gemeten wordt op 3 meter boven de grond, hoeft dat niet per se van de verdampende plant recht onder het meetinstrument te komen.

Met behulp van een zogenaamd 'footprint' model, kan berekend worden welk gebied invloed had op de transportmeting van een bepaald moment. Dit model is echter gebaseerd op een aantal aannames, die eigenlijk niet helemaal gelden boven een gebied met verschillende bodemtypen of gewassen. Echter, juist boven zo'n heterogeen gebied wil men weten waar de gemeten luchtwervels precies vandaan kwamen.

Daarom hebben wij een aantal modellen geïmplementeerd, toegepast op eddy-covariantiemetingen uit Duitsland, en de footprints met elkaar vergeleken. Ook hebben we de footprints vergeleken met onze verwachting van de footprint naar aanleiding van de transportmetingen van een aantal nabijgelegen velden. Daaruit bleek dat alle geteste modellen een grotere footprint berekenen dan was afgeleid uit de waarnemingen.

Bovendien hebben we gekeken naar de onzekerheid van de parameterwaarden waarmee we het model aansturen. Door een gevoeligheidsanalyse uit te voeren kwamen we er achter dat vooral opgepast moet worden het oppervlak niet te glad in te schatten. Tevens moet de invloed van verticale luchtbewegingen niet onderschat worden. Maar de verschillen tussen de modellen zijn duidelijk groter dan de verschillen die verkregen worden door de ingevoerde gegevens iets aan te passen.

In de 'Perspectives' hebben we uitgewerkt dat behalve de grootte, ook de vorm van de footprint niet goed gemodelleerd wordt. Het model van Hsieh et al. (2000) komt het dichtst bij de footprint die is afgeleid uit waarnemingen van meerdere stations. Echter, wij raden aan het model van Kljun et al. (2002) aan te passen. Dit model bevat namelijk al de eerste stappen om de vorm van de footprint aan te passen aan verschillende maten van turbulentie.

Een aantal van de aannames die onder andere in footprint modellen gebruikt worden, gaat over een verband tussen de hoeveelheid uitwisseling aan het aardoppervlak, en de transportwaarneming vlak daarboven. Dit is een verband dat volgt uit de zogenoemde Monin-Obukhov gelijkvormigheidstheorie (Monin and Obukhov, 1954).

Volgens de Monin-Obukhov gelijkvormigheidstheorie, is een waarneming van turbulentie in de onderste 100 m van de atmosfeer alleen maar gerelateerd aan wat er aan het aardoppervlak gebeurt. In weer- en klimaatmodellen worden de luchtbewegingen voor de onderste luchtlaag dan ook berekend aan de hand van de oppervlakte-eigenschappen. Verscheidene onderzoekers hebben de laatste jaren aangetoond dat niet alleen het aardoppervlak, maar ook de lucht boven de grenslaag invloed heeft op de luchtbewegingen en gasconcentraties in de oppervlakte-laag.

Wij hebben onderzocht of 'eddies' die afkomstig zijn van de luchtlaag boven de grenslaag, ons eddycovariantiesysteem op 3 m hoogte bereikten. Met behulp van de weerballondata konden we aantonen dat dat in Zuid-Frankrijk inderdaad af en toe zo was. Dit betekent dat de Monin-Obukhov gelijkvormigheidstheorie dan niet

overeenkomt met de metingen, en daar dus niet altijd toepasbaar is.

Vervolgens hebben we geprobeerd de relaties, die afgeleid worden uit de theorie, aan te passen. We hebben een methode ontwikkeld om te schatten hoeveel variantie in het vocht signaal niet veroorzaakt wordt door oppervlakteprocessen, maar door inmenging van droge lucht van bovenaf. Behalve droger, zijn deze luchtballen ook nog eens veel groter dan luchtballen die met het oppervlak te maken hebben, waardoor we ze konden detecteren in onze waarnemingen.

De instrumenten die voor de nauwkeurige en zeer frequente waarneming van wind, temperatuur, vocht en CO₂ nodig zijn, zijn behalve duur ook ingewikkeld in het gebruik. Er zijn dus wereldwijd maar weinig locaties waar de uitwisselingen tussen land en atmosfeer gemeten worden. Daarom hebben wij een methode verbeterd (de Rooy and Holtslag, 1999), waarmee het transport van waterdamp en warmte geschat kan worden aan de hand van waarnemingen die wél op elk weerstation uitgevoerd worden.

Voor deze studie hebben we temperatuur-, wind-, straling- en vochtwaarnemingen van overdag van een aantal maanden gebruikt om de uitwisseling van warmte en vocht te schatten. We hebben de geschatte uitkomsten met eddycovariantiemetingen vergeleken voor twee verschillende gewassen en voor twee verschillende regio's. De hier gebruikte waarnemingen in Nederland en zuid-Frankrijk waren verzameld boven gras, en de gebruikte waarnemingen in west-Duitsland waren boven graan verzameld.

Voor het schatten van vochttransport bleek lastig. De sleutelvariabele daarbij was de weerstand voor het transport uit de bladeren, transpiratie. Door het schema van de Rooy and Holtslag (1999) aan te passen, konden we het vocht- en warmtetransport boven gras en graan in Nederland en Duitsland goed nabootsen. De schattingen voor zuid-Frankrijk verschilden echter van de waarnemingen. Dit komt vermoedelijk door de aanwezigheid van grote droge luchtballen zoals hierboven beschreven.

De mate van atmosferische turbulentie is belangrijk voor het gebruik van bijvoorbeeld telescopen, radars, en zendmasten, omdat de hiervoor gebruikte elektromagnetische stralen verstrooid worden door turbulente luchtbewegingen. Hoe meer turbulentie, hoe meer problemen met deze apparatuur. We hebben een bestaande methode toegepast om deze zogenaamde optische turbulentie te kwantificeren aan de hand van het geschatte vocht- en warmtetransport dat volgt uit bovengenoemde methode. Daarmee laten we zien dat de mate van atmosferische turbulentie af te leiden is uit waarnemingen van een eenvoudig weerstation.

Voor bovenstaande studies hebben we eddycovariantiemetingen gebruikt, waaruit we transport van warmte, vocht en CO₂ kunnen afleiden. Het vochttransport dat gemeten wordt, wordt veroorzaakt door verdamping van water uit de bodem, en door het uitademen van water door planten. Voor sommige onderzoeken is enkel

bodemverdamping van belang, voor andere juist alleen de transpiratie van het gewas. Betreffende CO₂-transport, moet een onderscheid gemaakt worden tussen uitgedemd CO₂ door bodemorganismen en plantenwortels, en ingedemd CO₂ door bovengrondse vegetatie.

We hebben een bestaande theorie getest, die gebruikt wordt om CO₂- en vochttransport dat gemeten is met een eddycovariantiesysteem op te splitsen in bodemverdamping, bodemrespiratie, transpiratie en assimilatie. We hebben ontdekt dat bij gebruik van deze methode, het heel belangrijk is wat de watergebruiksefficiëntie van het betreffende gewas is. Dat wil zeggen, hoeveel koolstof er kan worden opgenomen bij een bepaald watergebruik van de plant.

De splitsingsmethode van Scanlon and Kustas (2010) kwam vaak niet tot een oplossing voor de waarnemingen verkregen boven groeiend graan in Duitsland. We hebben ons verdiept in de berekening van de watergebruiksefficiëntie van het gewas en in de uitwisseling van CO₂ en H₂O op bladniveau. We hebben vervolgens de berekening aangepast, waardoor de methode vaker leidt tot een oplossing voor onze metingen.

Bovendien hebben we ontdekt dat het veel uitmaakt voor de fractie transpiratie van het gemeten vochttransport, voor welke hoogte de watergebruiksefficiëntie berekend wordt. Een vervolgstap zou zijn om de verbeterde methode te valideren met verdampings- en transpiratiemetingen. Deze zijn op veldschaal niet beschikbaar, maar op plantschaal kan de transpiratie bijvoorbeeld afgeleid worden uit sapstroommetingen, en kan bodemverdamping gemeten worden met een zogenoemde kamermeting tussen de planten.

In dit proefschrift presenteren we de validatie van vier theorieën. Voor een aantal methodes presenteren we verbeteringen. Ons onderzoek is relevant voor vele vakgebieden, variërend van astronomie tot hydrologie. Elementen van dit onderzoek kunnen gebruikt worden om weer-, klimaat-, gewasgroei-, koolstof-, en hydrologische modellen te verbeteren, om zo te werken aan wereldproblemen als het voedseltekort en de opwarming van de aarde.

Dankwoord

Dit 'boekje', waar jullie mij heel 2014 veel over gehoord hebben, is door mij samengesteld. Mijn begeleider Arnold heeft hier veel aan bijgedragen. *Arnold*, bedankt! We hebben veel van elkaar geleerd. Ook wil ik jou en mijn promotor *Bert* bedanken voor de vrijheid in onderwerpen en tijdsbesteding. Ik ben heel blij dat ik naast mijn data analyses en het schrijven van artikelen, aanmoediging kreeg om mee te doen aan het project *Academici* voor de Klas, aan pitch wedstrijden, en andere activiteiten. *Alex*, I'm very happy that you dare to sit on the podium as well during my defense. I hope this makes you realize I really had pleasant and productive months in Jülich.

Oscar, Hank, O4, jullie wil ik bedanken voor de fijne samenwerking in Lannezean. Het verzamelen van data was een van mijn hoogtepunten van mijn PhD, mede dankzij jullie! *Miran*, dankjewel voor, veel te kort samengevat, je hulp met het ordenen van mijn gedachten. Dat verdient een paranimf positie! Evenals jij die aan mij gunde. We hebben heel veel fijne, vertrouwelijke gesprekken gehad, en ik hoop dat dat zo blijft. *Michal*, we hadden een moeilijke start daar op de 5^{de} in Atlas, maar daardoor leerden we elkaar wel snel kennen. Ik vond het heel fijn met jou een kantoor te delen.

Daan, ik vond het zo gezellig met jou op kantoor in de containers, dat ik je na de tweede verhuizing weer op mijn kamergenotenlijst had gezet! En wat moet ik nu zonder jouw geheugen? Ik voel me heel vereerd dat ik jouw paranimf ben. *Jordi* en *Huug*, bedankt voor jullie inzichten. *Kees* en *Caroline*, bedankt voor jullie technische en administratieve ondersteuning. *Mieke*, bedankt voor het medeleven tijdens de afhandeling van mijn ingewikkelde belastingsituatie. Ooit zal het opgelost zijn!

Sieg, we zijn er allebei trots op, vriendinnen sinds onze 2^{de}. Poppen opereren in een boomhut is nu verruild voor het bespreken van onze eigen lichamelijke kwaaltjes, maar ik vind het nog steeds erg gezellig! Mijn waardering voor je steun blijkt uit je erebaantje als paranimf op de dag van mijn verdediging. *Rens*, *Tim*, *Bart*, ook jullie bedankt voor de support de afgelopen jaren. Echte Thym-workers zijn we. Onze weekendjes Dublin, Milaan, Eifel, Ardennen, en al die etentjes, superfijn en opbeurend altijd!

WAffies, thanks a lot for all those great practices, games, lunches and dinners. Although my head was not always ready for tactics after a hard working-day, you all helped me relaxing at least twice a week! *Bram*, jij vooral bedankt. Jouw motivatie en benadering hebben er mede voor gezorgd dat ik bij de Nationaladies terecht kwam! *Tartléten* en specifiek *Trimsalonniers*, bedankt voor het gemoedelijke samenwonen op Droef! *Suus, Renée, Marlou, Airen*, heerlijk om twee keer per week met jullie de werkdag volledig af te sluiten onder het genot van frisse lucht, zware oefeningen of fietsen, en oneindig geklets!

Elske en *Karst*, bedankt voor de goede zorgen en het relativerende geouwehoer op de maandagen van het afgelopen jaar. Die dokterstitels hebben we mooi in de buze! *Rammie*, jouw turbulentie heeft mij ook goed gedaan de laatste jaren. Je werkt voor mij inspirerend, om mijn vastgeroeste patronen eens de boel te laten! *Esther*, bedankt voor al die fijne saunagesprekken. De andere bezoekers vinden het vast heel fijn dat we die gesprekken nu hebben, als we met je kleintje uit wandelen gaan!

Marijk, Maaik, Vera, ik vind het jammer dat ik niet meer in Friesland woon, en dat we mekaar nog maar weinig kunnen zien. Maar áls het ons weer gelukt is bijeen te komen, dan moet ik altijd bewust adempauzes inlassen, voor mij een teken van gezelligheid! *BWA-dames*, hoe uniek dat ook wij nog af en toe samenkomen! *Kerstin, Nina*, thanks for all your cards from everywhere around the world! Finding a fully-written postcard in my mailbox after a tough day is always cheerful. *Elly* en *Carel*, jullie ook bedankt voor de aanmoedigende kaartjes en de mooie tijd in Australië!

Vati en *muti*, dank jullie wel voor de nuchterheid. Bij jullie op de boerderij kan ik altijd weer helemaal bijtanken! Ik zou graag bij jullie en oma in de buurt wonen, onder het motto 'doe maar gewoon', maar mijn Brabander heeft al problemen met aarden in Twente. *Sjon, Geert*, bedankt voor je hulp bij het maken van de voorkant en de figuren in de introductie. Ik ben er trots op, en ik hoop jij ook!

Mansje. Ik in Duitsland, vervolgens jij in Australië, vervolgens ik weer in Duitsland, jij naar Enschede, naar Barcelona, ouders in het noorden en zuiden van het land, wat een uitdagingen. We hebben het elkaar niet makkelijk gemaakt, maar ik ben zo blij en trots dat we dat al vijf jaar hebben overwonnen! Xje daarvoor, en ook voor al die uren die je via skype, telefoon, of live naar mijn PhD-perikelen hebt weten te luisteren. Jij bent de enige die mij echt rustig krijgt!

The author



<i>Name</i>	Anneke van de Boer
<i>Born</i>	05.02.1986 in Heerenveen
<i>Pre-university education</i>	Stellingwerf College, Natural sciences
<i>Bachelor of Science</i>	Wageningen UR, Soil, Water and Atmosphere
<i>BSc thesis</i>	Identification of Monsoon depressions
<i>Study abroad</i>	University of Oslo, Meteorology and Oceanography
<i>Management</i>	Thymos, full-time Commissioner of Sports
<i>Master of Science</i>	Wageningen UR, Meteorology
<i>MSc thesis</i>	Atmospheric turbulence in a pine forest
<i>MSc internship</i>	FZ-Jülich, Flux-footprint models
<i>PhD</i>	Wageningen UR, University Bonn, 01.09.2010-31.12.2014
<i>Award</i>	Best poster-presentation, Symposium Bonn, March 2013
<i>PhD education</i>	see page 144

Journal publications by the author

van de Boer, A., Moene, A.F., Schüttemeyer, D., Graf, A.: Sensitivity and uncertainty of analytical footprint models according to a combined natural tracer and ensemble approach, *Agr. For. Meteorol.*, 169, 1–11, doi:10.1016/j.agrformet.2012.09.016, 2013 (**Chapter 2**).

Graf, A., Werner, J., Langensiepen, M., **van de Boer, A.**, Schmidt, M., Kupisch, M.: Validation of a minimum microclimate disturbance chamber for net ecosystem flux measurements, *Agr. For. Meteorol.*, 174-175, 1–14, doi:10.1016/j.agrformet.2013.02.001, 2013.

Graf, A., **van de Boer, A.**, Moene, A.F., Vereecken, H.: Intercomparison of Methods for the Simultaneous Estimation of Zero-Plane Displacement and Aerodynamic Roughness Length from Single-Level Eddy-Covariance Data, *Bound.-Layer Meteorol.*, 151, 373-387, doi:10.1007/s10546-013-9905-z, 2014.

van de Boer, A., Moene, A.F., Graf, A., Schüttemeyer, D., Simmer, C.: Detection of Entrainment Influences on Surface-Layer Measurements and Extension of Monin-Obukhov Similarity Theory, *Bound.-Layer Meteorol.*, 152, 19-44, doi:10.1007/s10546-014-9920-8, 2014 (**Chapter 3**).

Lothon, M., Lohou, F., Pino, D., Couvreux, F., Pardyjak, E. R., Reuder, J., Vilà-Guerau de Arellano, J., Durand, P., Hartogensis, O., Legain, D., Augustin, P., Gioli, B., Faloon, I., Yagüe, C., Alexander, D. C., Angevine, W. M., Bargain, E., Barrié, J., Bazile, E., Bezombes, Y., Blay-Carreras, E., **van de Boer, A.**, Boichard, J. L., Bourdon, A., Butet, A., Campistron, B., de Coster, O., Cuxart, J., Dabas, A., Darbieu, C., Deboudt, K., Delbarre, H., Derrien, S., Flament, P., Fourmentin, M., Garai, A., Gibert, F., Graf, A., Groebner, J., Guichard, F., Jimenez Cortes, M. A., Jonassen, M., van den Kroonenberg, A., Lenschow, D. H., Magliulo, V., Martin, S., Martinez, D., Mastrorillo, L., Moene, A. F., Molinos, F., Moulin, E., Pietersen, H. P., Pignatelli, B., Pique, E., Román-Cascón, C., Rufin-Soler, C., Saïd, F., Sastre-Marugán, M., Seity, Y., Steeneveld, G. J., Toscano, P., Traullé, O., Tzanos, D., Wacker, S., Wildmann, N., Zaldei, A.: The BLLAST field experiment: Boundary-Layer Late Afternoon and Sunset Turbulence, *Atmos. Chem. Phys.*, 14, 10789–10852, doi:10.5194/acpd-14-10789-2014, 2014.

Blay-Carreras, E., Pino, D., Vilà-Guerau de Arellano, J., **van de Boer, A.**, De Coster, O., Darbieu, C., Hartogensis, O., Lohou, F., Lothon, M., Pietersen, H.: Role of the

residual layer and large-scale subsidence on the development and evolution of the convective boundary layer, *Atmos. Chem. Phys.*, 14, 4515–4530, doi:10.5194/acp-14-4515-2014, 2014.

van de Boer, A., Moene, A.F., Graf, A., Simmer, C., Holtslag, A.A.M.: Estimation of the refractive index structure parameter from single-level daytime routine weather data, *Appl. Opt.*, 53, 5944–5960, doi:10.1364/AO.53.005944, 2014 (**Chapter 4**).

Pietersen, H., Vilà-Guerau de Arellano, J., Augustin, P., de Coster, O., Delbarre, H., Durand, P., Fourmentin, M., Gioli, B., Hartogensis, O., Lothon, M., Lohou, F., Pino, D., Ouwersloot, H. G., Reuder, J., **van de Boer, A.**: Study of a prototypical convective boundary layer observed during BLLAST: contributions by large-scale forcings, *Atmos. Chem. Phys. Discuss.*, 14, 19247–19291, doi:10.5194/acpd-14-19247-2014, 2014.

van de Boer, A., Moene, A.F., Graf, A.: Influence of leaf water-use efficiency on the partitioning of eddy-covariance-derived evapotranspiration, in preparation, 2015 (**Chapter 5**).



*Netherlands Research School for the
Socio-Economic and Natural Sciences of the Environment*

D I P L O M A

For specialised PhD training

The Netherlands Research School for the
Socio-Economic and Natural Sciences of the Environment
(SENSE) declares that

Anneke van de Boer

born on 5 February 1986 in Heerenveen, The Netherlands

has successfully fulfilled all requirements of the
Educational Programme of SENSE.

Wageningen, 6 February 2015

the Chairman of the SENSE board

Prof. dr. Huub Rijnaarts

the SENSE Director of Education

Dr. Ad van Dommelen

The SENSE Research School has been accredited by the Royal Netherlands Academy of Arts and Sciences (KNAW)





The SENSE Research School declares that **Ms Anneke van de Boer** has successfully fulfilled all requirements of the Educational PhD Programme of SENSE with a work load of 56.8 EC, including the following activities:

SENSE PhD Courses

- o Biogeochemistry and biophysics of the lower atmosphere, Cyprus (2010)
- o Environmental Research in Context, Apeldoorn (2011)
- o Research Context Activity: Organising 3rd Scintillometer Workshop, Wageningen (2011)
- o Pitch presentation workshop, Wageningen (2012)
- o Bridging the scale gap between atmospheric scales, Wageningen (2012)

Other PhD and Advanced MSc Courses

- o PhD competence assessment (2011)
- o Boundary Layer Later Afternoon and Sunset Turbulence (BLLAST) Field campaign (2011)
- o Scientific writing (2012)
- o PhD career assessment (2013)
- o Personal leadership (2014)
- o PhD course carousel: 'Visualising Science: how to present infographics (pictures, tables graphs) of your research', 'Finding and acquiring small grants: an overview of where to get small grants and how to obtain them', 'Be a vital PhD', 'Culture: The hidden rules of the game; how to function well in a diverse cultural setting' (2014)
- o Last stretch of your PhD (2014)

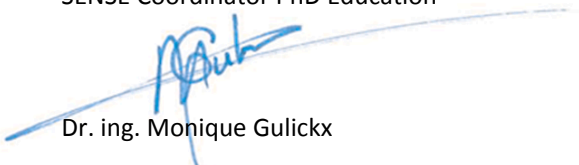
Management and Didactic Skills Training

- o 'Meer academici voor de klas' (more academics in secondary education) (2012)
- o Teaching tutorials 'Environmental data collection and analysis' (2012-2013)
- o Teaching practicals and tutorials 'Atmosphere-vegetation-soil interactions' (2012-2014)
- o Supervising BSc student: thesis entitled 'Early warnings for critical transitions in the stable boundary-layer' (2013)
- o Teaching field work course 'Land-atmosphere interactions' (2013-2014)

Oral Presentations

- o *Uncertainty analysis of analytical flux footprint models*. EGU Conference, 4-9 April 2011, Vienna, Austria
- o *Applying footprint models to investigate MO-dissimilarity over heterogeneous areas*. AFM conference, 28 May - 31 June 2012, Boston, United States
- o *Entrainment influences on surface layer measurements*. Boundary Layer Later Afternoon and Sunset Turbulence (BLLAST) Workshop, 5-7 Augustus 2013, Bergen, Norway
- o *Cn2 from single-level weather data*. Atmospheric Physics Symposium "Scintillometers and Applications", 7-9 October 2013, Tübingen, Germany.
- o Atmospheric turbulence over a heterogeneous surface. Boussinesq Center for Hydrology 1st Spring Meeting, 7 April 2014, Wageningen, The Netherlands

SENSE Coordinator PhD Education


Dr. ing. Monique Gulickx

This research was financially supported by the German Research Foundation (DFG), in the projects 'Links between local scale and catchment scale measurements and modeling of gas exchange processes over land surfaces' (SCHU2350/2-1 and GR2687/3-1) and 'A parametrization for structure-function parameters derived from weather-station data' (SI606/26-1).